Optical and Electrical Characterization of $ZnSnN_2$ Thin-Films

by

James P. Mathis

A dissertation submitted in partial fulfillment
of the requirements for the degree of
Doctor of Philosophy
(Applied Physics)
in The University of Michigan
2020

Doctoral Committee:

Professor Roy Clarke, Chair
Professor Steven Durbin, Western Michigan University
Professor Cagliyan Kurdak
Professor Lu Li
Professor Vanessa Sih

James P. Mathis

jpmathis@umich.edu

ORCID iD: 0000-0002-2770-2032

-To My Wife, Nikki - For all the years we've had to live apart and the literal *thousands* of miles we've traveled just to see each other. You've always been there for me as my rock. I love you.

-To my Friends & Family - For all the times I wanted to come visit and couldn't because of experiments, conferences, writing, etc.

-To my Lord and Savior, Jesus Christ - For keeping me sane amidst all the craziness of life up to this point, and for allowing me to understand just a sliver of some of the intricacies of His creation.

ACKNOWLEDGEMENTS

I'd like to express my deepest gratitude to Dr. Roy Clarke. You have been an incredibly understanding and motivational advisor. Thank you for everything you've done to keep me going by teaching me and encouraging me to finish. You are an inspiration and I cherish your wisdom and friendship.

A very special thank you, to the Applied Physics program, especially Cyndi D'Agostino, Chuck Sutton, and Cagliyan Kurdak for giving me a chance to take on this endeavor and to pursue one of my life goals.

A very special thank you, to Dr. Steve Durbin, Dr. Bob Makin, and Krystal York. Without you all, I would not have had the opportunity to work on this amazing project. Thanks for showing me the ropes of (and time committment needed for) MBE. My development as a scientist is in large part because of you and the time you spent with me helping me understand such an intricate growth technique.

A very special thank you to Dr. Nancy Senabulya Muyanja, who conducted several experiments which were vital to the continuity and completion of this dissertation.

A very special thanks also goes to Greg DeMaggio, Chuck Taylor and Barry Wissman, from k-Space Associates, Inc who were always ready to help me with troubleshooting and development of my ideas throughout the time I spent there.

A special thank you, to Darryl Barlett and k-Space Associates, Inc in Dexter, MI for their support and hospitality shown to me by giving me the lab space that I needed to tackle my most important experiment, even *after* I accidentally locked myself in the facility after hours.

TABLE OF CONTENTS

LIST OF FIGURES

Figure

ABSTRACT

This dissertation focuses on a new thin-film semiconductor material for optoelectronic applications such as solar energy harvesting and solid state lighting. The work represents a detailed exploration of the optical and electrical properties of epitaxial thin films of $ZnSnN_2$ (ZSN), a member of the II-IV nitride family of compounds in which cation ordering was predicted as a novel route to tuning the relevant optoelectronic characteristics. It also represents the first attempt at quantum confinement in a ZSN isocompositional heterostructure using cation order/disorder as a control parameter.

The increasing demand for alternatives to fossil fuels and the scarcity of certain metals commonly used in LED lighting, together highlight the need for earth-abundant optoelectronic materials. This has led to the development of the II-IV-V family of semiconductors–a wide variety of materials that enable access to the VIS/IR portions of the electromagnetic spectrum. As a member of this family, ZSN is composed entirely of earth-abundant elements and early theoretical investigations of it predict compatibility with solar cell applications, with band gaps ranging between 1.0 eV and 2.5 eV, depending on the degree of cation ordering.

The methodology for synthesizing ZSN with specific properties was developed in collaboration with a group at Western Michigan University, resulting in the first fully ordered, orthorhombic ZSN films. We present original results on the optical and electrical characterization of ZSN thin-films grown on (111) yttria-stabilized zirconia (YSZ) via plasma-assisted molecular beam epitaxy (MBE). A key finding is that the band-gap of the material is correlated with cation ordering across a large portion of

the infrared and visible spectrum. The degree of ordering was quantified by an order parameter, defined as $S = r_\alpha + r_\beta - 1$, where r_α and r_β represent the fractions of Zn and Sn cation sites occupied by Zn and Sn atoms, respectively. Values of S from 0.05 to as high as 0.92 were achieved in this work, as measured using *in-situ* Reflection High-Energy Electron Diffraction (RHEED) and *ex-situ* X-Ray Diffraction (XRD). Optical characterization included Photoluminescence (PL), Cathodoluminescence (CL) and Diffuse Reflectance Spectroscopy (DRS). The CL results are the first evidence of light emission from single-crystal ZSN thin-films. Another innovative aspect of our work was to modify conventional DRS to enhance optical absorption contrast from our thin-film samples, namely "waveguided diffuse reflectance spectroscopy" (WDRS), providing vital data on how the band-gap depends on the degree of cation ordering.

Electrical measurements were carried out to explore fundamental properties relevant to device fabrication–specifically mobility and carrier concentration. Hall measurements reveal high carrier concentrations ranging from $3.37\text{x}10^{20}$ cm^{-3} to $2.08\text{x}10^{21}$ cm^{-3}, while measured mobilities ranged from 1.27 cm^2/Vs to 32.5 cm^2/Vs. These results suggest that the density of carrier-generating defects, and perhaps a degenerate population, may be responsible for the comparatively low mobilities, resulting from an increased scattering cross-section and short mean-free-paths (10-100 nm)[1]. Further refinement of the growth parameters should help to reduce uncompensated charge carrier concentrations, found to be mainly n-type in our samples.

The results, the first of their kind in many cases, highlight the importance of continuing the development of ZSN as a promising earth-abundant alternative to existing III-V and II-VI compounds. In particular the correlation between heterovalent cation ordering and materials characteristics of importance for potential optoelectronic applications is shown to be especially fruitful for future studies.

CHAPTER I

Introduction

1.1 Motivation

1.1.1 The Importance of Semiconductors

Semiconductors are one of the foundational building blocks of the modern world. Each day, billions of people use them in such a wide menagerie of applications, that it's safe to say the research and discovery of semiconductors has ushered in what we know as the "Digital Age" and the "Internet of Things." Consequently, the versatility of semiconductors extends beyond that of a single application for a single industry. Indoor lighting, communications devices, computers, radios, TVs, medical equipment, solar panels, and almost every type of sensor are just a few of the various applications in which semiconductors are utilized to equip the world with the technology upon which we rely, daily. Such versatility arises from the exploitation of their physical, electronic and optical properties, which allow them to be tailor-engineered to the needs of a particular industry as broad as lighting and microelectronics, and as specific as earth-abundant, thin-film photovoltaics.

Lately, the solar energy conversion industry has been steadily growing in popularity because it seeks to directly address a number of global issues that will have lasting impacts on the planet. Increasingly limited fossil fuels and climate change have

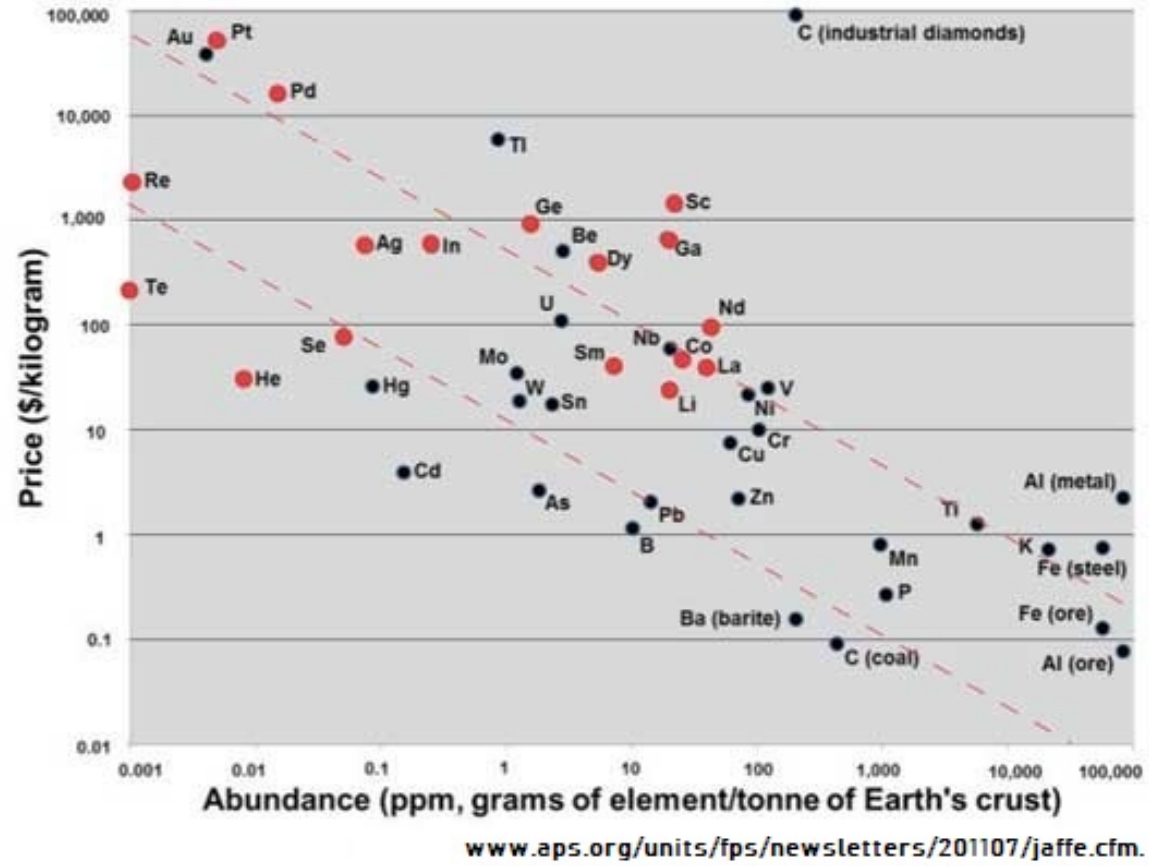

Figure 1.1: Here numerous elements have been charted based on their dollar amount per kilogram vs their crustal abundance[3].

sparked a societal paradigm shift in how we think about energy consumption, which in turn has paved the way for the last 50 years of photovoltaic-based research. To compound this issue, the diminishing supply of certain rare elements in conjunction with their ubiquitous use across significant and booming technological industries has created cause for concern about these elements' long-term availability[2]. As a result, the need for Earth-abundant alternatives has become acutely noticeable, particularly in industries like optoelectronics where mass-production is the objective. The challenge is that the most common material being used in solar cells today, silicon, is limited in energy conversion efficiency to roughly 29% and can only be used for efficient solar energy harvesting in its bulk form[4]. To address this need, scientists have been implementing new methods to increase solar cell efficiency in two main ways: the

creation/discovery of new materials and the redesign of solar cell geometries. The latter has seen somewhat limited progress, in terms of the ability to mass produce more efficient cells, for two main reasons. The first is that the elements which constitute these materials, like arsenic and cadmium, are toxic and require specially designed infrastructures for handling and disposal. Secondly, many of the elements used in the higher efficiency cells, especially elements like indium, are rare and expensive, as depicted in Figure 1.1, factoring heavily into the cost of production.

1.1.2 The Impact of Silicon

Silicon's renown is undoubtedly rooted in the fact that it is the second-most abundant element in the Earth's crust–making up roughly 28% of it–and thus it's also the second-most widely accessible material known to man[3]. In 1824 Jons Jacob Berzelius, a Swedish chemist, discovered silicon by heating up chips of potassium in a silica container, and then washing away the residual by-products[5]. Since then, silicon has been researched, studied and tested rigorously so that better, more efficient technologies can be created, many of which have already enhanced our lives. Increasingly more electronic devices have been utilizing silicon for components like transistors and microchips, and even outside of the electronics industry, silicon has been used for products like lubricants, different types of glass, medical implants and more. Perhaps one of today's most important technologies still being developed and iterated upon is the solar cell–over 90% of which are currently based on silicon[4].

1.1.3 The Solar Cell

The solar cell has quite a long history, starting in 1839 when French physicist Edmond Becquerel built the world's first photovoltaic device[6]. Since then, many other contributing milestones have been achieved; for example, in 1883 Charles Fritts produced the first solid state photovoltaic cell using selenium-gold junctions[7], which

achieved 1% efficiency; in 1905 the Nobel Prize for Physics was won by Albert Einstein for his paper in which he proposed a new quantum theory of light and a new understanding of the photoelectric effect; and in 1954 Chapin, Fuller and Pearson reported the first silicon-based solar cell, which converted sunlight with 6% efficiency[4]. Though early production costs stymied broad commercialization of these silicon cells, the prospect of remote power delivery spurred on research and development. Predictably, many of the advances in the microelectronics industry have benefitted the silicon-based solar cell and have helped drive it to its current prowess. In tandem with silicon, other important discoveries have led to the broadening in range of materials used to produce solar cells. Some of the more well-known of these include: various transparent conducting oxides (TCOs)[8], gallium arsenide (GaAs), and later, copper indium gallium selenide (CIGS)[9]. But silicon is not perfect. There are three main factors that contribute to a material or element being compatible for use in solar energy conversion: earth abundance, band structure, and conversion efficiency.

1.1.4 Why Silicon Isn't the Anwser

1.1.4.1 The Shockley-Queisser Limit

In 1961, William Shockley and Hans J. Queisser[10] proposed that the maximum, theoretically-achievable efficiency by a single p-n junction solar cell is 30%, based on the second law of thermodynamics. This proposition countered previous predictions, which were based on empirically-determined thermodynamic losses for (then) current Si-based cells (see Figure 1.2). Instead, they believed the basis for the "detailed balance limit" calculation rested on mathematically representing the fundamental physical processes that occur on the atomic scale which lead to losses and gains in the overall efficiency. One of the most notable details that their work outlined was the significance of losses in efficiency due to radiative recombination, one that the semiempirical limit does not consider. Further assumptions include: the

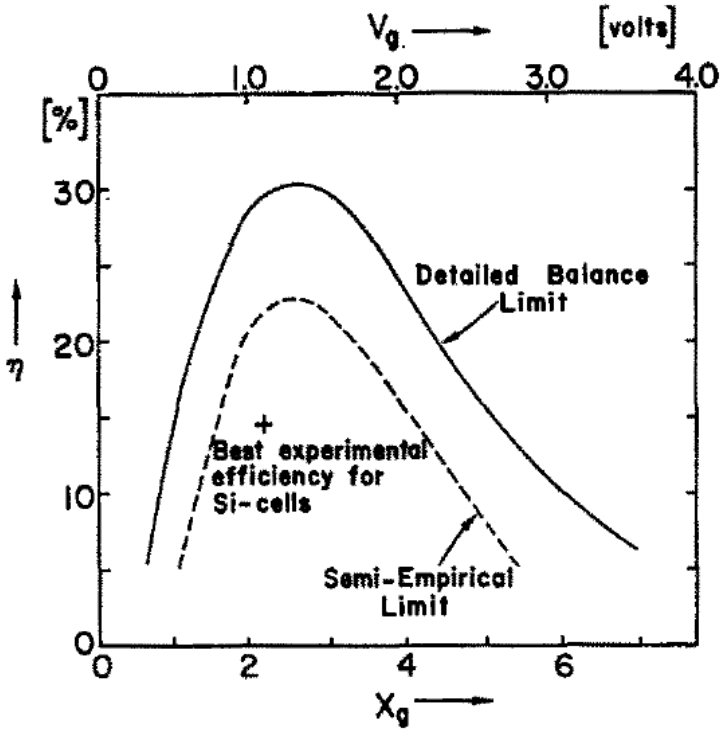

Shockley, et al., *Journal of Applied Physics*, 32(3), 1961.

Figure 1.2: Shockley and Queisser proposed the detailed balance limit as the maximum achievable efficiency by any single p-n junction solar cell. For band gaps of interest to photovoltaics, this maximum efficiency is around 30%[10]. Here X_g is defined by the ratio: $\mathrm{E}_{gap}/k_B\mathrm{T}_{sun}$, where k_B is Boltzmann's constant.

absorption of all photons with energy $E_{photon} > E_g$, oblique incidence on one side of a planar cell, 1:1 photon/e-h pair generation for photons with $E_{photon} > E_g$, a 6000^oC blackbody source and perfect collection of photogenerated electrons. These considerations can be summarized by the fact that photons which exceed the minimum energy for valence-conduction band transitions will lose their excess energy by thermal excitation. Shockley and Queisser also predicted the positive effect that defect minimization would have on the silicon crystal and inferenced this assumption to be generally applicable to other materials. In its entirety, their work scrutinized the effects of the all the processes involved in the photogeneration of excitons from a thermodynamic standpoint, and is considered by many to be the most significant theoretical contribution to this field to date.

1.1.4.2 PV Efficiency-Limiting Factors

One of the most important findings from the detailed balance limit is the significance of addressing each of the atomic processes involved, including: efficient electron-hole pair generation and separation, current extraction, and minimization of radiative and non-radiative recombination (which maximizes the open-circuit voltage, and allows for higher power outputs). All these, in addition to the proper selection of the material, must be taken into consideration to make most efficient use of its bandgap. Schockley and Queisser also suggested that dislocations in the material, caused by impurities, decrease the carrier lifetimes and diffusion lengths (two important quantities for current generation and extraction). This turned out to be a major factor in increasing cell efficiencies, and has since been one of the top priorities particularly for growth scientists who fabricate crystalline materials.

1.1.4.3 Single-Crystal Silicon

Crystalline silicon cells currently make up >90% of the market, which alone speaks to its versatility and relative ease of production. The well-known Czochralski method of slowly drawing a crystalline seed out of a melt to create high purity silicon has provided a low-cost method of mass-production and revolutionized the industry. Additionally, intrinsic carrier concentrations as low as 10^{10}cm^{-3} and mobilities as high as 1400 cm^2/Vs make it one of the best semiconductors we have available to us. The issue with monocrystalline Si lies in the fact that it appears almost completely opaque to a significant fraction of the Sun's radiation (i.e., beyond the IR region). While this implies a relatively large absorption coefficient, much of the absorbed radiation gets converted to heat due to its low band gap of 1.1 eV. This means long-wavelength absorption must be prioritized to achieve the desired efficiencies, which requires a thicker absorbing layer and, thus, more material for production.

1.1.4.4 Amorphous Silicon (a:Si)

Amorphous silicon (a-Si) once emerged as a promising alternative to bulk silicon for a few key reasons. It can be produced at low temperatures; it's used in thin-film form, reducing material costs, and it offers higher optical absorption properties than its bulk counterpart. However, these benefits come at a heavy price when considering the disadvantages. Amorphous silicon is relatively difficult to dope, possessing no long-range atomic order. Apart from this, it has dangling bonds which act as recombination centers for carriers. These contribute negatively to its already subpar transport properties, with mobilities less than 0.01 cm^2/Vs (140,000 times worse compared to monocrystalline Si!), and the dangling bond density increases over time causing it to degrade more quickly due to heat. All these factors subtract from the overall conversion efficiency, which nets to less than 10% as a result, and end up inhibiting a-Si more than bulk, since these limiting properties don't allow for opti-

mal integration with other technological advances like doping and the use of optical concentrators.

1.2 Theory on Solids

1.2.1 The Periodic Table

All matter is made up of atoms, "the building blocks of the universe." But these building blocks are themselves made up of a three basic particles called protons, neutrons and electrons.The number of protons in an atom determines its position in the periodic table; so, if you take a proton out of a given element, say Carbon, then you'll end up with a different element, namely Boron. However, if you change the number of electrons, its net charge changes, which affects how that element reacts to its environment, or the material(s) with which it comes into contact. The periodic table (see Figure 1.3) neatly presents all of these elements separated into rows and columns. All elements in a given row (or period) have similar electronic configurations in their outer (valence) shells, while all the elements in a given column have similar chemical and physical properties. Beyond this, the elements can be separated into classifications based on their physical properties and their location on the periodic table. For instance, the noble gases are all in Group VIII and are inert in their natural forms. Group I elements are known as the alkali metals, and are highly reactive with most substances. Then there are elements that are not all in the same Group, but share other similar properties: like the reactive non-metals, the metalloids, and the transition metals. It is the combinations of elements in these last three categories to which we often refer generally as *semiconductors*. As the name suggests these materials may act as either a conductor or an insulator, depending on their physical structure and the conditions to which they are exposed. They have higher electrical conductivities than an insulating material like glass, but lower conductivities than

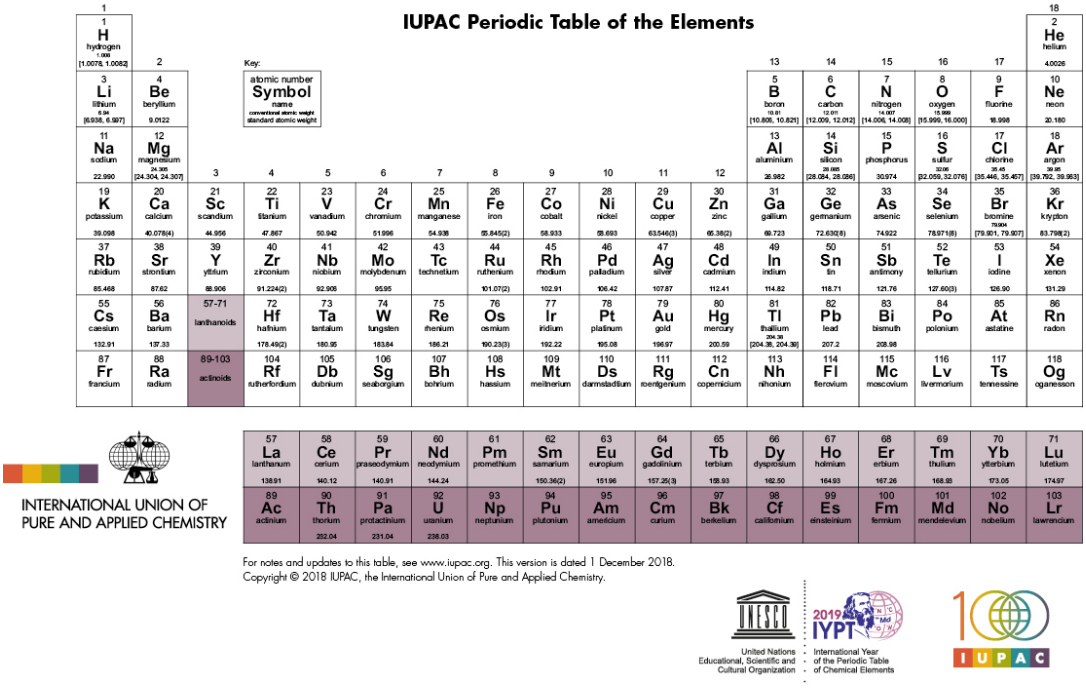

Figure 1.3: The Periodic Table. Rows are known as "periods," and columns are identified as "groups"[11].

a metallic conductor like copper. While protons and neutrons make up the large part of an atom's mass, the electrons and protons are what contribute to the atom's charge and, as in all materials, it is these charged particles that give a semiconductor its inherent electrical properties. Protons, which reside at the center of the atom alongside the neutrons, are positively charged, while electrons which form a sort of "cloud" around the atoms in orbitals are negatively charged. These layers, often referred to as "shells," are characterized by the the number of electrons that are allowed to reside within it and amount of energy it takes to remove an electron from it. In the most basic case, the Hydrogen atom houses one proton at its nucleus and one electron in its shell. This electron shell is held very tightly to the center of the atom due to the attractive force between the two (assumed) point charges, given by Equation (1.1):

$$\mathbf{F}_E = \frac{q^2}{4\pi\epsilon_0 r^2}\hat{\mathbf{r}}, \tag{1.1}$$

where r is the distance between them. As the atomic number is increased, the total number of electrons within the cloud, and the amount that may reside within each subsequent layer, increases rather slowly. This is governed by a combination of the Aufbau principle, which ensures that lower energy orbitals get filled first, and the Pauli exclusion principle, which limits the number of electrons of the same spin-type that can exist within a given orbital. This means that unless the number of electrons within the atom coincides with the amount that may completely fill the outermost shell, or valence band, like in noble gases, vacancies will exist in the valence band allowing for bonding with other atoms, so as to fill this band.

1.2.2 Bonding

Chemical bonding is the glue that holds various materials together to constitute a particular substance. They are the result of either the sharing or transfer of valence-shell electrons between atoms. There are two types of chemical bonds that may occur: covalent and ionic. As the name suggests, covalent bonds occur when two atoms share the same electron(s). A common example for this is the water molecule (H_2O), in which two hydrogen atoms share their valence electrons with a single oxygen atom. However, when one atom gives up its valence electron(s) and transfers it to another atom then the two atoms form an ionic bond, of which the most commonly known example is sodium chloride (NaCl)–or table salt. In this example, the sodium atom gives up its single valence electron to the nearly-full, chlorine atom's valence shell. This satisfies what is known as the Pauli Exclusion Principle, which states that no two electrons within a particular atom may simultaneously share the same quantum number or state.

1.2.3 Crystallinity, The Bravais Lattice, and Reciprocal Space

Most solids can be classified into one of three general categories: amorphous, polycrystalline, and crystalline. Within an amorphous solid, say silicon for example, the atoms are arranged as an interconnected network such that the material has short range order (largely preserving the tetrahedral silicon covalent bonding) but lacks long range order that the crystalline form displays. This results in a large variation in bond lengths between atoms, as seen in Figure 1.4, as is the case with amorphous silicon (a-Si). Figure 1.5 shows a schematic of a polycrystalline solid, which contains atoms that are arranged in a very specific order, but only in small, localized areas dispersed randomly throughout the material. To clarify, the arrangement of atoms in one area of the material may not look or be the same as the arrangement in another; so, we say that the atoms have no "long-range order." This type of crystallinity is particularly

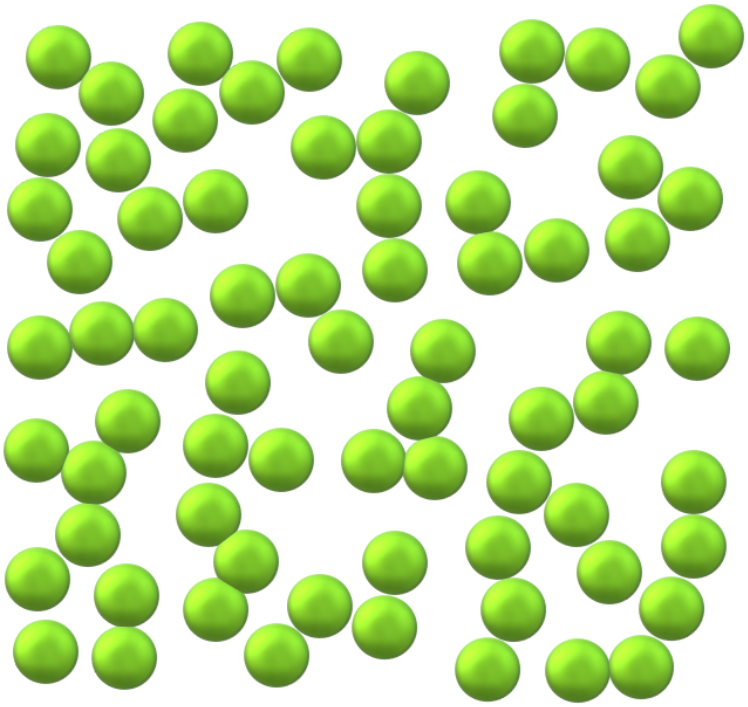

Figure 1.4: A schematic of the atomic structure in an amorphous solid.

common in lattice-mismatched materials or in materials with high in-plane strain. For a material to be crystalline, like in Figure 1.6, this "long-range order" must exist, so that the arrangement of atoms in one area of the material is *identical* to any other area of that material. More specifically, there are two governing principles which a material must follow to be classified as crystalline: 1) the real-space locations of its atoms (or groups of atoms) must repeat periodically such that they form a Bravais lattice (of which there are 14 types); and 2) the resultant reciprocal lattice vectors of said Bravais lattice must satisfy the plane wave equation such that:

$$e^{i\mathbf{K}\cdot\mathbf{R}} = 1. \tag{1.2}$$

Here, $\mathbf{R}$ describes the real Bravais lattice and $\mathbf{K}$ is the set of all wave vectors that create plane waves with Bravais lattice periodicity–the reciprocal lattice. Simply put, this means that only certain waves with specific properties will be able to propagate

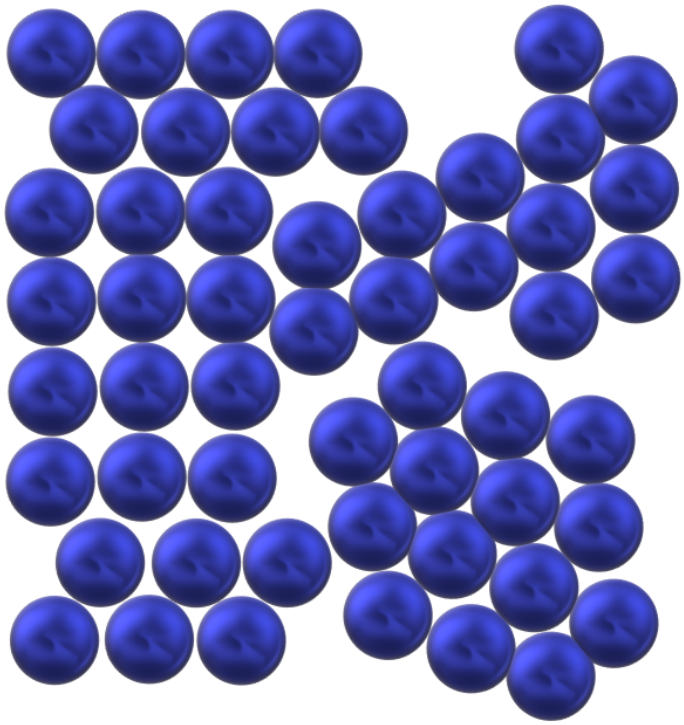

Figure 1.5: A schematic of the atomic structure in a polycrystalline solid.

through the material. Sometimes these Bravais lattices are made up of *sub*lattices of a certain combination and/or spatial configuration of elements, which in turn constitute that particular lattice's *unit cell*. The unit cell is the most basic form of the crystal structure; the one piece that gets repeated all throughout the material. In the case of zinc tin nitride (ZSN), the subject of this thesis, there are two sublattices: one for the cations and one for the anions. The cation sublattice is comprised of a two-atom heterovalent basis made up of one group II element and one group IV element, while the anion sublattice contains one group V element. These compounds can be more easily realized by replacing the cation pairs from the analogous III-V semiconductor coumpounds with the mixed cation pair previously mentioned. Another notable difference is that the ternary heterovalent cation compounds, such as ZSN, can take up different structures depending on whether the cations are ordered on their respective sites, as opposed to the alloy-like random mixing of cations across their sublattice.

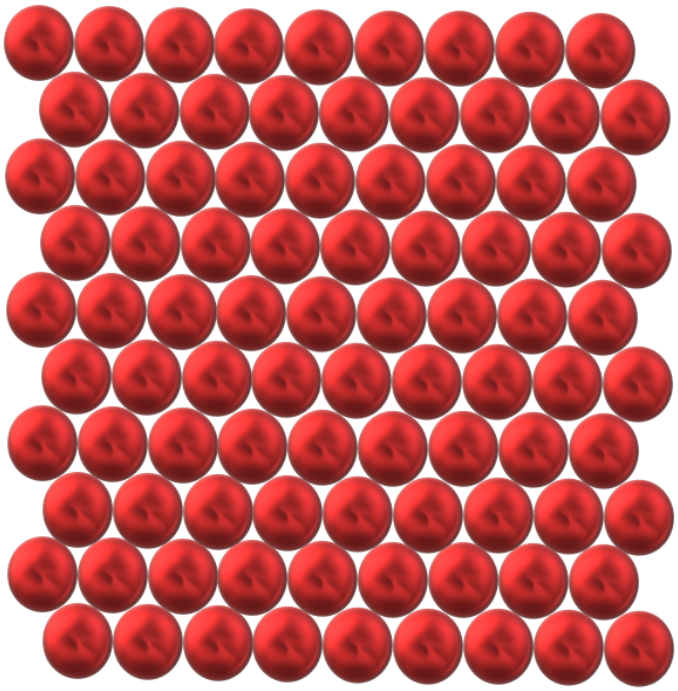

Figure 1.6: A schematic of the atomic structure in a crystalline solid.

When the two types of cation (Zn and Sn) are randomly mixed the overall structure resembles the hexagonal "wurtzite" structure of binary compounds like GaN.

The focus of this dissertation is to better understand the optoelectronic consequences of this cation ordering in the II-IV nitride family of semiconductors. The work presented here, resulting from a collaboration with faculty and students at Western Michigan University (the Durbin group) has led to substantial progress over the last few years, most of which has been published in a series of joint publications[12–15]. This same cation ordering leads to the arsenide and phosphide II-IV-V_2 semiconductors having the chalcopyrite structure[16, 17], which can be thought of as structurally equivalent to zincblende, but with ordered group II and IV cations. The II-IV-N_2 compounds, being more ionic than their (zincblende) arsenide and phosphide counterparts are analogous to the wurtzite III-Vs, and adopt a related orthorhombic crystal structure, (Figure 1.7a), if the group II and group IV cations are ordered; and

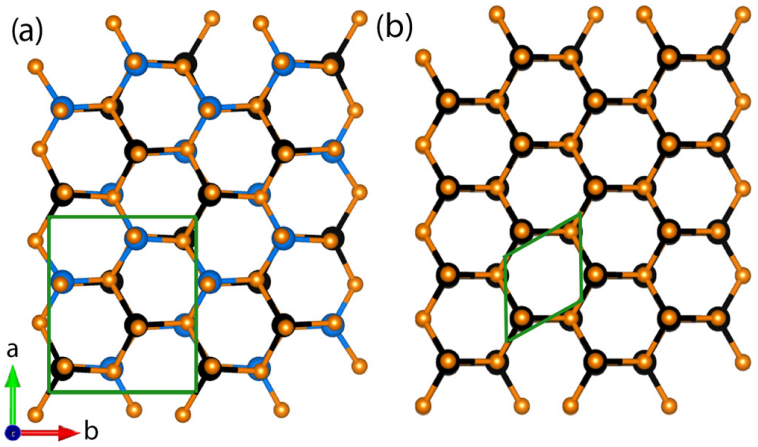

Figure 1.7: A top-down, c-axis view of the (a) orthorhombic and (b) wurtzite structures with the respective unit cells outlined in green. Note the doubling of the unit cell along the a-axis[18].

the structure reverts to wurtzite, (Figure 1.7b), if the cations are disordered[19]. Cation ordering is predicted to be favored (under equilibrium conditions) through the replacement of group III atoms in the companion III-N by group II and group IV atoms imposing stringent conditions on local charge neutrality. The theoretically predicted range of zero-temperature band gaps for the family is 0.6 to 5.7 eV[20], which, like the (Al,Ga,In)N family, spans the entire visible solar spectrum (as well as near infrared and near ultraviolet wavelengths). In addition, and perhaps just as importantly, the constituent elements are better classed as "earth-abundant" with the crustal abundance of Sn almost two orders of magnitude larger than that of In, and the occurrence of Zn more than three orders of magnitude larger than that of In (see Figure 1.1). Thus, the importance of the II-IV-V family is that it provides an earth abundant alternative to the well-known In/GaN series of alloys, one which is capable of band gap tuning across the IR/Visible/UV spectral range, with direct band gaps in many cases. The aspiration of this work as a whole is to achieve desirable electronic and optical properties that could be of value for new types of earth-abundant semiconductors which exhibit favorable properties for optoelectronic applications.

1.2.4 Band Gaps

The existence of a material's band gap can be attributed to two fundamental concepts: (1) every solid has a unique energy-band structure created by its conduction and valence band states–we derive the energy-dispersion relation, E(**k**), from this–and (2) energy is quantized for electrons, meaning they may only occupy specific energy states. The valence electrons can be approximated by the particle-in-a-box model from quantum mechanics (delineated here in 1-dimension), where the solutions to the Schroedinger equation are sine waves, given by:

$$\psi_n(x) = Asin(\frac{2\pi}{\lambda_n}x), \tag{1.3}$$

with eigen energies,

$$E_n = \frac{\hbar^2 k_n^2}{2m} \tag{1.4}$$

using the boundary conditions imposed by the infinite square well of width L: $\psi(0) = 0$ and $\psi(L) = 0$. From here, one finds that energy is quantized and that only for specific values of n (0 and all positive integers) will the Schroedinger Equation be satisfied. This directly correlates to the band structure of the material, as it is a graphical representation of these allowed states. In metals, we start with the free-electron gas model, in which ions are pinned and valence electrons are free to move about, while still obeying the Pauli exclusion principle[21]. Here the valence and conduction bands overlap each other or have an extremely low separation, allowing all electrons in the half-filled conduction band to participate in conduction. In insulators and semiconductors however, there exists a notable separation between the highest, occupied valence band states and the lowest, nominally unoccupied conduction band states. Within this region, there are no available states for electrons to fill and thus

it is known as the energy *band gap*, expressed in terms of its width(energetically). For insulators this separation is too large for electrons to cross, typically > 5 eV, but most semiconductors fall within the range of 0.67 (Ge) - 3.5 (GaN) eV. This allows semiconductor electrons to be easily excited into the conduction band by means of thermal excitation, without causing physical degradation to the material, as compared to an insulator.

At this point, it's important to note that in a crystal any given energy band, whether a valence band or conduction band, is associated with a momentum-like vector, $\boldsymbol{k}$. This is a direct consequence of Bloch's theorem which states that a quantum particle moving through a periodic potential has a wavefunction of the form

$$\psi_n(x) = e^{i\mathbf{k}\cdot\mathbf{x}} u_{n\mathbf{k}}(x). \tag{1.5}$$

From this we get the E($\mathbf{k}$) dispersion relation for a given material, which is the identifying "fingerprint" of its crystal geometry. Of course the quantum particles themselves are what actually inherit this momentum. The states within each band always fill upward, starting with the lowest energy states in that band. At some specific crystal momentum, or $\mathbf{k}$-value, the energy band reaches either its maximum (VBM), for the valence band, or its minimum (CBM), for the conduction band. In materials like GaAs, where these two bands' k-values coincide at their respective maxima/minima, a *direct* band gap exists. Here *only* a photon of energy $E \geq E_{gap}$ is required for excitation. Alternatively, the VBM may *not* coincide with the CBM at the same $\mathbf{k}$-value, leading to what is called an *indirect* band gap. In such a case a phonon, a quanta of kinetic motion, is required to provide the momentum needed for an electron to be excited into the conduction band.

For solar energy harvesting, the consequences of this relationship are critical to the correct choice of the material. Indirect-gap semiconductors usually require more ma-

terial due to a longer absorption length (microns) because of the need for momentum-conserving phonons in the absorption process; direct gap materials on the other hand are compatible with thin film technology (with an active-layer thickness of microns or less). According to calculations presented in [18], the theoretical band-gap of $ZnSnN_2$ is direct and in the vicinity of 1-2 eV, depending on whether the cations are ordered (2 eV) or disordered (1.12 eV). The motivation for this dissertation is the prior lack of detailed experimental evidence of this as well as a desire to explore, for the first time, the optoelectronic response of this material system in both single layers and quantum-confined structures.

1.3 Theory on Light

1.3.1 The Photo-Electric Effect

One very well-known phenomenon, the photo-electric effect, which was first observed by Heinrich Hertz in 1887 and subsequently explained by Einstein in 1905, provides a good mental picture for, and is strongly correlated to, the way a solar cell works. Hertz' goal, in the experiment in which this phenomenon takes place, was to observe the nature of light and, in particular, whether or not an interaction existed between light particles (photons), and the electrons which reside freely upon the surface of metals. To measure this interaction, he placed a piece of metal foil very close to a closed electric circuit, through which no current was flowing, but also through which he was able to measure any subsequent flow of current. He then directed a light source of variable wavelength, and thus energy, at the piece of metal foil. Somewhat to his surprise, a measureable current began flowing through the adjacent electric circuit. In fact, and perhaps less surprisingly, the higher energy photons, ultraviolet (UV) light, produced higher currents within the electric circuit. It turns out that since the free electrons in metals aren't bound to positive charges, like they usually

are in other materials, you can eject them from the metal itself, provided you do supply enough energy for the electrons to overcome what's known as the work function of the material. The work function, ϕ, is the amount of energy needed to pull an electron out of a material. To make an analogy, one could imagine a fish tank partially filled with water. If you were to gently place a tennis ball on top of the water, so that it floats, you wouldn't cause any splashing. But if you were to throw that tennis ball as hard as you could against the surface of the water, you'd make a mess by splashing water out of the tank. By this analogy, if the water represents the electrons which reside on the surface of the metal, and if the tennis ball represents the incident photons, then the distance between the surface of the water and the top of the tank would represent the work function, and speed with which you throw the ball would represent the energy of the photons. The lower the water level within the tank, the more energy is needed to eject electrons from that material, or in this analogy to splash water out of the tank. Incidentally, the physics of the photo-electric effect is not to far removed, conceptually, from how solar cells can harness energy from our sun, the main difference being the means by which the electrons are extracted from the material.

In semiconductors, electrons that are used for energy transfer are loosely bound to the valence, or outer-most, "shell" of their respective atoms. It costs some finite amount of energy to remove these electrons from the atom and then excite them to a higher-energy state. Once they have entered this higher-energy state, they may be extracted from the material and utilized for energy transfer, for example, to generate electricity for powering homes and/or electronics. One of the challenging aspects of making this work, however, is that electrons prefer to occupy lowest-energy states available. As such, they will readily give up the energy that was given to them, by the incident photons, as heat in order to occupy that lower energy state. So in order to make the solar cell actually effective, often times a bias, whether "natural" or

external, is applied to the cell geometry to encourage the diffusion and/or drift of these electrons from one side of the material to the other, without recombining with an atom (where the lower energy states usually reside). This causes a flow of negative charge in one direction, which is called a current, and in this case more specifically a photocurrent. To extract this photocurrent, however, it is necessary to connect this cell to a external circuit.

1.3.2 P-N Junctions

In electronics, current is driven by an electromotive force cause by a difference between two electrostatic potentials; this is commonly referred to as a voltage. But once the circuit is completed current may flow in either direction, which is generally unfavorable to most electronic devices. This reverse current can decrease performance, inhibit or distort a desired signal, or it may even completely destroy the device. To mitigate this, engineers came up with the diode, which acts like a kind of "waterfall" to the electrons and allows current flow in only one direction. A p-n junction is a stack of semiconductors that have different charge flow properties based on the type of dopants in each material.

1.3.2.1 Intrinsic Semiconductors

To understand what a p-n junction truly is, it's best to start with explaining what the nature of an intrinsic semiconductor. For the sake of concreteness, let us consider Silicon (Si) as our material. In a Silicon atom there are four valence electrons, which participate in the tetrahedral bonding between the other Si atoms surrounding it. These electrons are confined to the valence band and have no motivation to cross the energy gap into the conduction band–hence intrinsic silicon is non-conductive, at low temperatures where thermal excitation is not possible.

1.3.2.2 P-type / N-type

When atoms of a different species, say Boron (B) from Group III, are introduced into the silicon, suddenly there are fewer electrons available to participate in bonding, causing a surge in electron *vacancies*, which we call "holes," to appear at the top of the valence band. These holes are able to "move" around freely within the valence band as if they were positive charges and are the majority carriers in a p-type material. Conversely, if an atom of another species, this time say Phosphorus (P) from Group V, is introduced there are suddenly *more* electrons available, creating a surplus of negative charge carriers. These extra electrons are no longer confined to the valence band, nor are they responsible for bonding, but instead are able to freely move about the material and participate in conduction. These electrons are the majority carriers in an n-type material. When these two types of materials are brought together to form a p-n junction, the free electrons and holes recombine leaving behind a region of positively and negatively charged ions near the interface between the two materials. This so-called "space charge" region creates a built-in electric field which rejects any further flow of charges. This is the basis upon which the p-n junction diode works.

It is the goal of solar cells to utilize this diode functionality by exploiting the band gap of the p-type material to generate electron-hole pairs via sunlight with intention that the adjacent n-type material will capture and conduct the electrons away from the interface and onto the external circuit components. Solar cells can either be made out of two different materials (heterojunction) or out of the same material (homojunction). One of them, the p-type, has more vacancies in the valence shells, and the other, n-type, has more occupancies. In the traditional cell, the n-type dopants, also called the "donors," give up the electrons from the valence band to be excited by photons and transfered to the p-type material, doped with "acceptors." By stacking these two materials, you can create a gradient in the energy bands, causing the carrieers to flow in specific directions depending on a few factors like the built-in

voltage, or V_B, for instance. This motion of charge from one material to the other introduces another nuance that is essential to understanding how a solar cell works– carrier density. Carrier density can be understood as the amount of charge per unit volume that is able to be transferred between materials. To clarify, carrier density is *not* the same as charge density. Where charge density is the total amount of charge within a given volume, carrier density is the amount of *transferable* charge per unit volume.

1.3.3 The Solar Spectrum

The spectrum of solar light incident on Earth's surface is known as the terrestrial solar spectrum and is unique to our planet. From basic physics, it is known that the ideal radiator is a black body, which emits all of its energy according to Bose-Einstein statistics, giving the well-known Planck blackbody radiation spectrum shown in black in Figure 1.8. Though this model is only an approximation and does not account for absorption by the atmosphere, our Sun's terrestrial spectrum providentially shares the same general shape as the blackbody's. In particular, the terrestrial solar spectrum happens to include all the wavelengths within the visible light spectrum in the portion that also has its highest intensities. This means that the majority of the total number of photons entering the atmosphere are within the visible spectrum, though infrared and some ultraviolet (UV) photons also permeate the atmosphere. The energy of a photon is given by:

$$E_{photon} = \frac{hc}{\lambda}, \tag{1.6}$$

where h is Planck's constant, λ is wavelength, and c is the speed of light. Between Equation 1.6 and Figure 1.8, we discern that semiconductors of a certain band gap could be useful for the absorption and/or emission of visible-range photons. More-

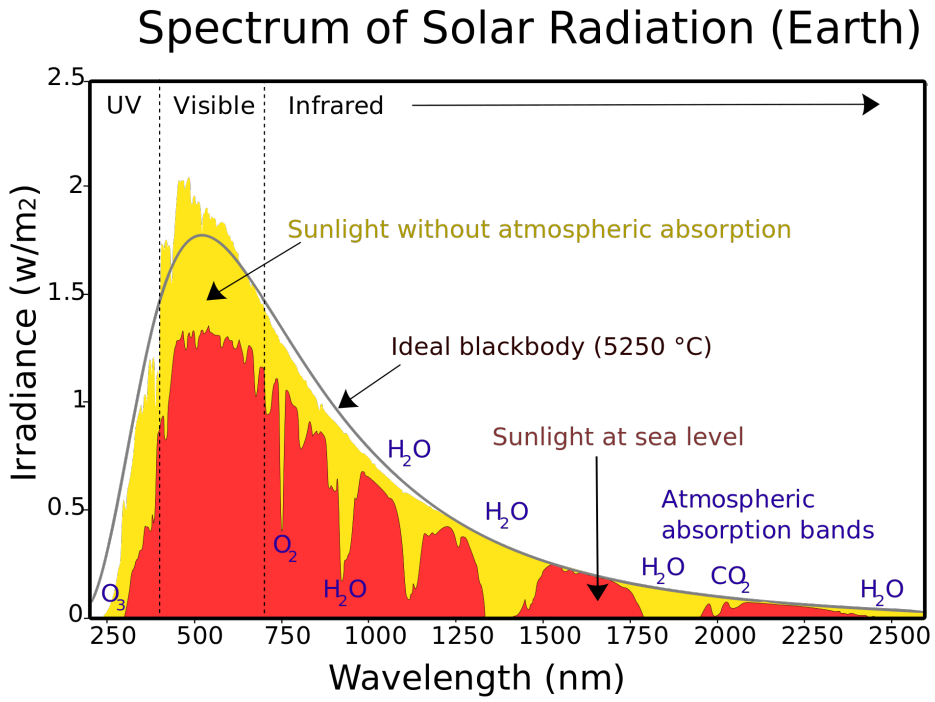

Figure 1.8: This figure shows the solar radiation spectrum for direct light at both the top of the Earth's atmosphere (represented by yellow area) and at sea level (red area). The sun produces light with a distribution similar to what would be expected from a 5778 K (5505 °C) blackbody, which is approximately the sun's surface temperature. These curves are based on the American Society for Testing and Materials (ASTM) Terrestrial Reference Spectra, which are standards adopted by the photovoltaics industry to ensure consistent test conditions and are similar to the light that could be expected in North America. Regions for ultraviolet, visible and infrared light are indicated[22].

over, the high-intensity wavelengths of terrestrial solar energy can be converted into electricity, by either direct-, or indirect-band gap semiconductors.

1.4 Recent Work & Development

Zinc-tin nitride is a relatively new material, having only been realized within the last ten years. Here some of the major milestones marked in the development of ZSN are noted and briefly discussed.

It was first proposed in 1984[16] as a potential solution to the looming energy crisis, along with the family of ternary nitride compounds. Some of the earliest work performed in the study of zinc tin nitride explored theoretical calculations in density functional theory (DFT) to estimate the band structure, electrostatic potential and lattice constants. Punya et al. [20] did this using the local density approximation (LDA). Since publication of that report, several important milestones have been achieved in the investigation of the physical nature of this material. In 2012, Feldberg et al. synthesized the first films, grown by plasma-assisted molecular beam epitaxy (MBE), and identified the two crystal structures to which ZSN conforms–the orthorhombic phase and the wurtzite phase. In situ RHEED measurements were made which catalyzed the experimental investigation of the crystal structure and optical properties of ZSN[18]. In 2013, several groups contributed to the investigation of the fundamental properties of ZSN. Various approaches were taken ranging from band gap calculations using different software packages, to the use of different types of synthesis techniques, to the probing of the optical band edge through various experiments. Punya et al. calculated the band offsets between $ZnGeN_2$ and $ZnSnN_2$ in relation to III-V compounds ZnO and GaN using DFT[23]. Though this had been investigated to some degree in their previous work[20], the 2013 study focused on acquiring a more accurate understanding of the band structure by using the (QS)GW approach, a different method for calculating the bulk portion of the material, and the

previously used LDA at the interfaces. This study further corroborated the notion that II-IV-N_2 materials were indeed viable for use in light-emitting diodes (LEDs) and in photovoltaics such as solar cells. Soon Lahourcade et al. [24] would synthesize ZSN on sapphire and GaN substrates via radio frequency (RF) magnetron sputtering. The crystal structure was determined to be orthorhombic by X-ray diffraction with calculated; the group also performed spectroscopic ellipsometry to obtain an estimated band gap of 2.0 eV (extrapolated from 1.8 eV absorption onset), which contradicted their calculated result of 1.42 eV (at zero Kelvin), using the hybrid HSE06 functional. This discrepancy was attributed to a phenomenon known as the Burstein-Moss Effect in which some conduction band states are partially filled, pushing the absorption edge higher, thus increasing (blue-shifting) the apparent band gap. Hall measurements found electron mobilities to be low, considering the band gap (approx. 10 cm^2/Vs or lower), which was attributed to extremely high carrier concentrations, ranging from 10^{19} cm^{-3} to 10^{21} cm^{-3}. Later, Quayle et al. [25] synthesized polycrystalline films of $ZnSnN_2$ by plasma-assisted VLS. SEM images depicted a somewhat rough, fragmented film of ZSN on top of a smooth Zn-Sn alloy. Further study and analysis included X-ray diffraction (XRD)and photoluminescence (PL) of said films and ultimately led to some of the first experimental values for the optical band gap of ZSN–around 1.7 eV +/- 0.1 eV. This seemed to somewhat agree with previous predictions made by Punya et al. [20] in 2011 and by Feldberg[18] in 2013, except that the crystal structure discerned by the XRD in this study exhibited a wurtzitic profile, as opposed to the orthorhombic profile associated with a band gap of that size. This sparked what has now become an ongoing debate over which band gap *should* be expected for the orthorhombic structure versus for the wurtzite structure, not dissimilar to the earlier controversies over the band gap of InGaAs. Still later in 2013, Feldberg[18] synthesized the first single crystal ZSN thin films. Though they were unable to detect a diffraction pattern at 22.1^o–a signature of the

orthorhombic structure–they still confirmed growth of the two different possible crystal systems for this compound. Significant 2014 studies included the theoretical work done by Chen[26] and the adjacent experimental work by Narang[27] on ZSN alloyed with germanium(Ge) via RF sputtering. Together, these studies explored both the phase stability of ZSN and the bandedge shift of the ZSN through Ge alloying, which discerned a minimum band gap of 2.0 eV for $ZnSn_xGe_{1-x}N_2$ (when x = 1).

Perhaps the most interesting distinctions between all of these experiments are the differences in growth methods and how that appears to have affected experimentally determined band gaps. As a result, many researchers have been scrambling to verify and understand the nature of ZSN–its band structure and electronic and absorption properties–for its two crystal structures. Unfortunately, the newness of the material and variability of growth methods and parameters have, thus far, contributed more questions than finality. Although many other groups have begun the exploration and characterization of ZSN, my colleagues and I have taken a unique approach to the growth of this material through MBE, with a focus on single crystal thin-films, and have performed optical and electrical experiments on these films. Based on this study, we maintain that the single-crystal, orthorhombic ZSN structure yields a band gap closer to 2.0 eV as predicted by Punya et al. [20], and that wurtzite structures yield a band gap closer to that predicted by Feldberg et al. [18] of 1.0 eV, and perhaps most interesting of all, that the band gap can vary in between these two extremes depending on the degree of cation ordering.

In more recent developments, Senabulya was able to isolate which growth conditions allowed for a stable, orthorhombic crystal structure in ZSN on YSZ substrates[12]. The structure was first probed with RHEED measurements[28], then verified via high-brilliance XRD measurements which were used to create 3D reciprocal space maps, called "pole figures," of the crystal structure within the samples. This paved the way for Makin et al. [13] to not only stabilize the growth conditions themselves, but also to

explore the growth space and decipher the correlation between the individual growth conditions and the resultant crystal structures. This has placed the PAMBE growth method in an advantageous position, as a ZSN film can now be relatively fine-tuned both in stoichiometric composition and in crystal structure. The two major components still missing for better understanding the nature of this epitaxially-grown material were detailed optical and electrical probing of its properties. With these, a more well-rounded characterization of this material can be gained as well as the phenomena at work which affect it. The next two chapters will detail the epitaxial growth of ZSN as well as the characterization techniques used to probe its optical and electronic properties.

1.5 Overview of the Proceeding Chapters

The remaining chapters will proceed as follows:

-Chapter II will first briefly discuss the significance of $ZnSnN_2$ as it pertains to the thin-film PV industry. Mention of the various methods that have been used to date will be made, and a detailed description of this dissertation's MBE growth experiments will be given, ending with a discussion of our findings.

-Chapter III will review the overarching concepts for each of the characterization methods used, as well as what can be learned from each technique. The order in which the characterization was completed will be implemented for the sake of continuity. They include: Reflection High-Energy Electron Diffraction (RHEED), X-Ray Diffraction (XRD), Diffuse Reflection Spectroscopy (DRS), Photoluminescence (PL), and Hall Effect measurements.

-Chapter IV will detail the setup of each of the experiments and results obtained from each experiment will be presented, as well as the conclusions that may be drawn from each. Here the novel contributions of this work to the field will be highlighted and discussed.

-Chapter V will summarize the major findings of this dissertation as well as any novel contributions that have been made to the field, mentioned in the preceeding chapters. Finally, a brief discussion about the significance of this work to the future of the project will be given, along with suggestions for how these experiments can be enhanced and iterated upon so that progress can be made in the field toward understanding the nature of $ZnSnN_2$ and where it stands in the context of the renewable energy market.

CHAPTER II

Growth Methods

This chapter details the material $ZnSnN_2$ as it pertains to various growth methods that have been used. Afterward, a description of this project's MBE growth experiments will be detailed, including the setup and discussion of our findings. Many of the details relating to growth have already been submitted and accepted for publication[12, 13, 15]. It should also be noted that the subject of collaborator R. Makin's doctoral thesis was the growth of and characterization of cation disorder in II-IV nitrides. Most of the samples studied in this dissertation project were grown in Prof. Durbin's MBE lab at Western Michigan University. The author of this dissertation worked in collaboration with R. Makin and K. York to fabricate many of the samples that are the focus of this dissertation.

2.1 A New Material for a Sustainable Future

A fundamental reason behind the creation of the thin-film photovoltaics industry was to provide a means to lessen the cost of solar cell production by reducing material costs generally associated with bulk materials like silicon and gallium arsenide (GaAs). While the development of thin-film photovoltaics has since largely been a success[29], there still exist some major roadblocks which must be overcome for them to truly begin to outpace the use of bulk materials in commercial devices. One of

those roadblocks, to which gallium arsenide also succumbs, is toxicity. Cadmium telluride (CdTe) is one of the two most prominent thin-film photovoltaics which has seen significant developments in the PV industry, the second being copper indium gallium diselenide (CIGS), which incorporates two low-abundance elements in its stoichiometry (indium and gallium). It is a direct bandgap material whose bandgap of ∼1.45 eV is well-suited for the conversion of the relevant portion of the solar spectrum into electricity. It has a high optical absorption (roughly $10^5 cm^{-1}$), p-type conductivity, and can be deposited by a myriad of different processes including, but not limited to, sputtering, thermal evaporation, and chemical vapor deposition[29]. Cadmium, however, is a carcinogenic byproduct of copper and lead mining which poses significant health risks from long-term exposure. Although much work has been done to refine the processes by which it is produced and recycled in order to mitigate human exposure to Cd, the impact on the rate of its development as a thin-film technology has undoubtedly had a slowing effect as a result.

The prospect of using ZSN thin-films as photovoltaic devices sees a significant advantage here, as it is entirely comprised of non-toxic, earth abundant elements, as discussed in Section 1.1.1. This nullifies any need for development of special infrastructures for the procurement and recycling of the consituent elements. As a result, zinc tin nitride has become of increasing interest to many photovoltaic scientists in recent years. Next we go into detail on the nature of its crystal structure.

Zinc-tin nitride forms crystals meaning that the overall crystal structure has long-range order with the cations distributed over their respective sublattice. This long-rang order can be quantified with an order parameter, S, which can vary from 0 (randomly distributed) to 1 (completely ordered)[15]. This feature is very important to enabling tunability of the bandgap while maintaining the overall integrity of the crystal structure. The two different structures arise based on the locations of the two metals–zinc and tin–on the sublattice, which are determined by the order parameter

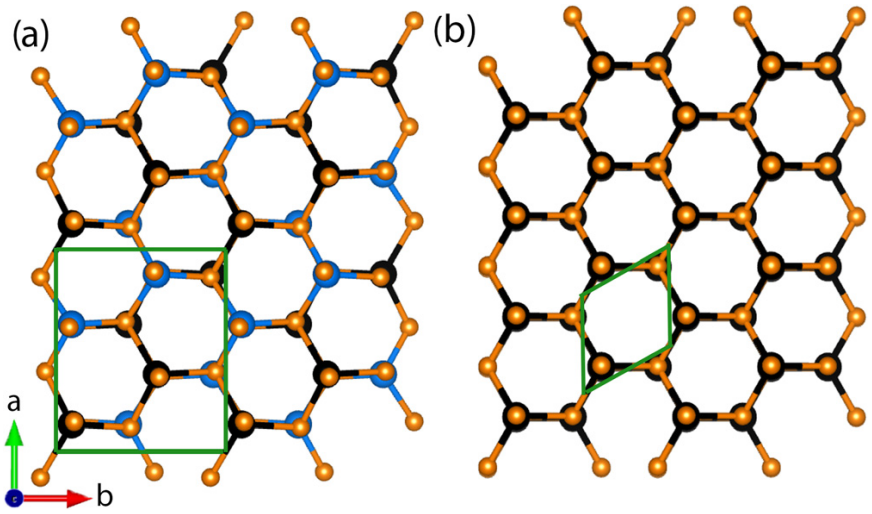

Figure 2.1: In (a) the orthorhombic structure is depicted. Black and blue atoms represent the Zn and Sn cations, respectively, configured in a perfectly ordered state, corresponding to S=1. Note the doubling of the unit cell along the orthorhombic a-axis. In (b) the cation species are not restricted to specific sites and are denoted by the black atoms. This represents the wurtzite structure, in which the random distribution of cations on the sublattice corresponds to S = 0[15, 18].

S, defined as $S = r_\alpha + r_\beta - 1$. For this study, r_α is the fractional occupation of Zn on Zn-sites and r_β is that for Sn on Sn sites. It is also important to note the requirement that $r_\alpha = r_\beta = r$, which results from the films being stoichiometric.

The more naturally occurring configuration of ZSN is known as the wurtzite structure which is characterized by its hexagonal symmetry. In this state, the distribution of the two cations is randomized and the crystal is said to be in the "disordered phase". As the sublattice becomes more ordered, eventually Zn atoms only occupy Zn sites and Sn atoms will only occupy Sn sites, forming the othorhombic structure; this is referred to as the "ordered phase." This is depicted in Figure 2.1.

As part of a previous study[12], it was found that the effects of this ordering result in a contraction of the basal plane in conjunction with an expansion in the out-of-plane direction, by 0.65% and 5.7%, respectively. Additionally in that work,

it was confirmed that orthorhombic substrates, like (001) $LiGaO_2$ (LGO), that are well-lattice matched to the zinc tin nitride cation sublattice are able to support this orthorhombic structure during single-crystal growth. These studies demonstrated that various substrates could be used to grow the films of the orthorhombic phase of ZSN, including LGO and YSZ, the latter case requiring the growth conditions to be tuned to achieve the desired structural phase transition.

2.2 Molecular Beam Epitaxy

Though other methods have clearly been used [24, 25, 27], the sole focus of this project was the application of molecular beam epitaxy (MBE) for the growth of $ZnSnN_2$ thin-films. One of the advantages of using an MBE system is that the stoichiometry of the material can be precisely optimized by applying the appropriate set of growth parameters. Here we will discuss each parameter and the role it plays in the growth of the films. A few of the disadvantages that come along with such precise control over the stoichiometry include: the need for ultra-high vacuum (on the order of 10^{-9} Torr), relatively high substrate temperatures (typically $>350°$ C), long growth times (depending on the material), and the tedious amount of upkeep and monitoring needed by the system, both during and outside of growth experiments.

Several $ZnSnN_2$ thin-films were grown via plasma-assisted molecular beam epitaxy (PAMBE) using a Perkin Elmer 430 molecular beam epitaxy system in conjunction with standard effusion cells, with thicknesses ranging between 10 and 100 nanometers and with variations in crystallinity between polycrystalline and single-crystal. All films were grown under the guidance of the Durbin Group using Dr. Steve Durbin's MBE system, located at Western Michigan University (WMU). An approximate schematic of the vacuum chamber and its components is shown in Figure 2.3 (exact geometry altered for clarity). The quality of the resulting films was determined by taking a line scan across RHEED images produced just after growth

and directly correlating pixel brightness to the intensity. This allowed for a sufficiently accurate analysis of the RHEED streak thickness, which is directly related to the level of defects and impurities (or lack thereof) within the crystal.

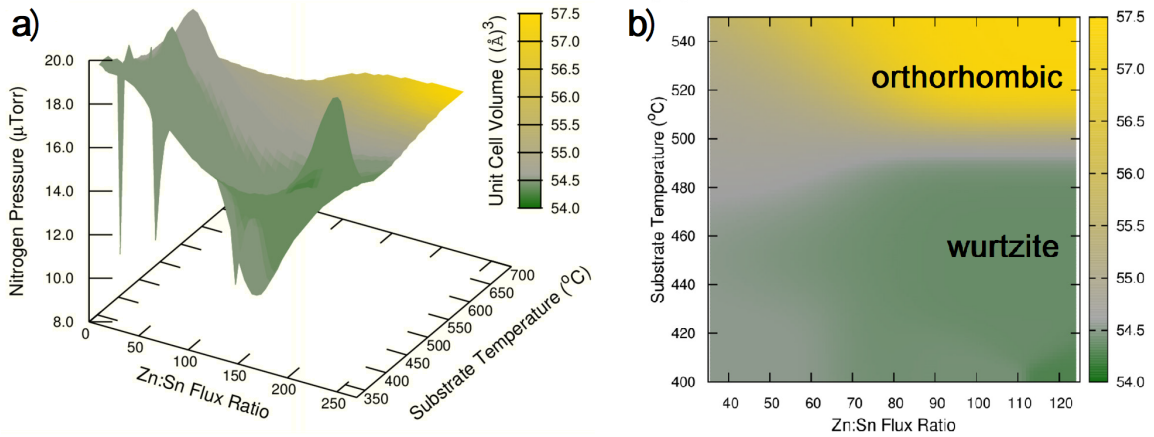

Figure 2.2: a) Here the growth space of $ZnSnN_2$ was been mapped as a function of the Zn:Sn flux ratio, substrate temperature, and the nitrogen pressure. The scale on the right represents the volume of the unit cell ($Å^3$), calculated from lattice constants which were obtained via XRD. b) shows the projection of the 3D map in a) onto the Zn:Sn flux and substrate temperature plane[13].

To achieve the desired degree of ordering, tunable parameters included: the radio frequency (RF) power, the N_2 flow rate, N_2 pressure, the Zn:Sn ratio (which is alterable by modifying the Zn and Sn fluxes), the substrate temperature, and the vacuum pressure of the system. A slight change in any of these may cause slightly or drastically varying results between growth runs. That being said and since it is generally understood that no two growth runs can be precisely the same, we considered it beneficial to focus on 2-3 parameters as variables and to make as few adjustments as possible outside of those parameters. This allowed for a more detailed study[13] of the effects of specifically chosen parameters on the growth space of the material. In that study, the growth space was mapped as a function of the nitrogen pressure, metal flux ratios, and substrate temperature (see Figure 2.2). Next, a detailed account of the process that precedes the growth of a thin-film is given, which will provide

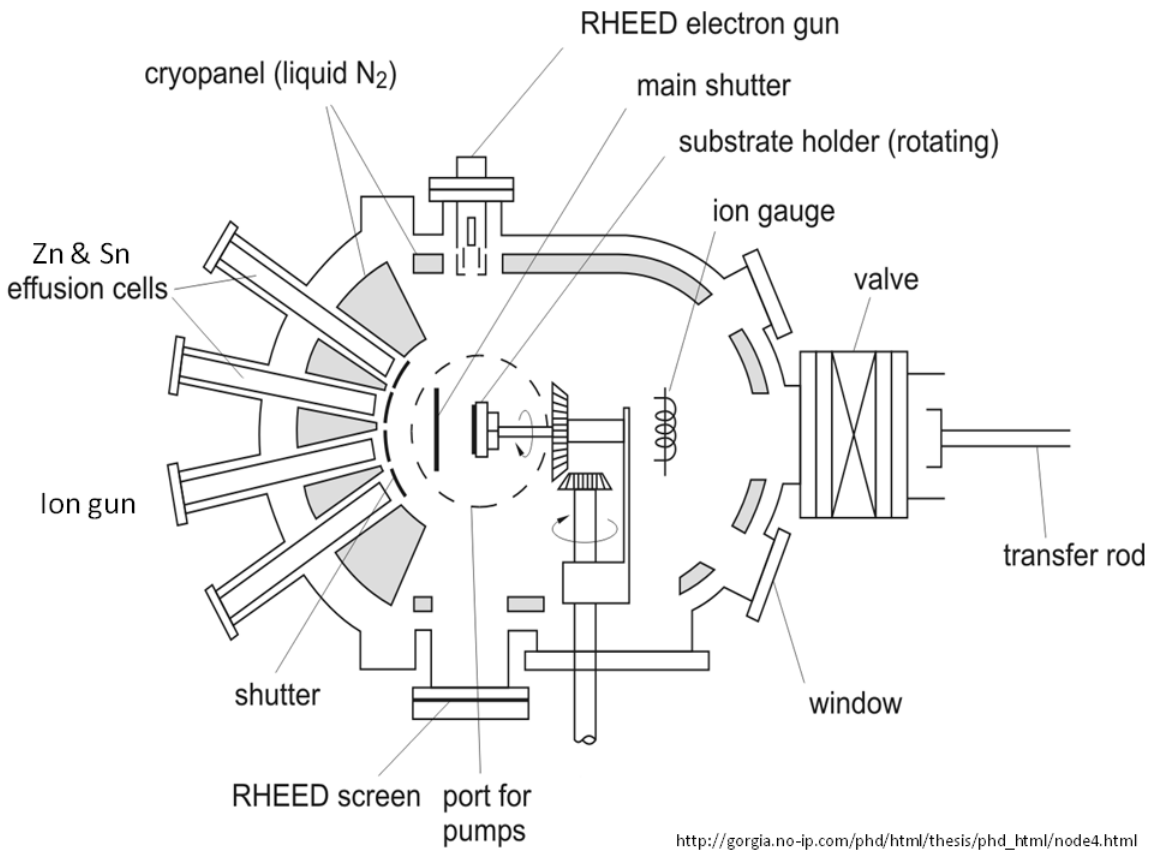

Figure 2.3: An approximate schematic of the MBE chamber used in the growth experiments[13].

valuable insight to the interpretation of some of the data which will be later explained.

2.2.1 Growth Details

Prior to initiating the growth, the Knudsen cells (or K-cells) must be heated, shown in Figure 2.4. K-cells are effusion evaporator sources which contain the individual metals being used for growth. Effusion is the process by which gas escapes from a container through a hole that is significantly smaller than the mean free path of the molecules in motion–which means the metals must first be vaporized into a uniform gas within the cell crucible chamber. For zinc and tin, this requires that each K-cell be heated to above 300°C and 1000°C respectively, so that a uniform stream

of metallic gas flows from each crucible chamber, through their respective aperture plates (each of which have a set number of apertures), into the growth chamber, and onto the substrate at a constant and measurable rate. This flow rate is determined by the molar mass of the gas, the pressure in the growth chamber on the other side of the aperture plate, and the number of apertures through which the gas may flow, and it is given by:

$$Q_{effusion} = \frac{\Delta P A N_A,}{\sqrt{2\pi M R T}}, \tag{2.1}$$

where ΔP is the pressure difference between the growth chamber and the crucible chamber, A is the area through which the metal vapor diffuses, N_A is Avogadro's number, M is the molar mass, R is the ideal gas constant, and T is the absolute temperature. Because zinc has a low sticking coefficient, the ratio between the rate of adsorption and the rate of desorption, a Zn overpressure must be applied to the growth environment in order to maintain the desired growth rate (roughly 130 nm/hr) at which stoichiometric films can be grown[13]. This means that the temperature of the Zn source must be adjusted to provide a sufficient flux, causing more zinc to be used up as compared to the tin. As a side note, it is very common for MBE systems to have more K-cells attached to the system than are used for a single growth (see Figure 2.3), (generally 3-4 depending on the size of the system), since many growth scientists work on multiple types of material growths. Before growth, each of these K-cells is closed off from the growth chamber by shutters, labeled in Figure 2.3, which prevent the metals from prematurely adsorbing onto the substrate. To gain an accurate estimate of the thickness of the thin-films, the metal flux must be measured for both metals. To do this the substrate is first averted from the K-cells, then the quartz crystal microbalance is lowered into the chamber, and finally the shutters are opened individually for flux measurements (see Figure 2.6).

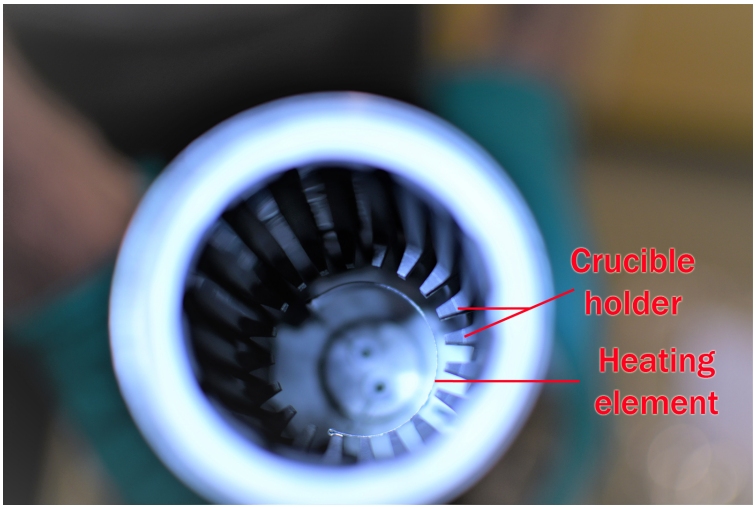

Figure 2.4: This picture shows the interior of a K-cell. In particular, the heating element and circular grill upon which the crucible sits, are shown.

The quartz crystal microbalance consists of a quartz-crystal oscillator set to oscillate at a specific frequency; when the shutter to the metal gas is opened, mass is added to the crystal which changes this oscillation frequency by a small amount. The rate of change quickly stabilizes over the course of about 10 to 20 seconds, and the individual frequencies are read out by a computer, where the average change in frequency is then calculated and recorded. After the metal flux measurements have been taken and the anticipated growth rate has been calculated, the crystal microbalance is retracted from the growth chamber.

The next step is to create an active-nitrogen rich atmosphere within the growth chamber by producing a nitrogen plasma with a source that creates energetic N_2 gas species. To begin this process, the nitrogen flow rate must first be determined which is based on the desired stoichiometry. To do this, an inductively-coupled Oxford Applied Research HD25 RF plasma source was fitted with a 256-hole aperture plate and equipped with electrostatic ion removal and an inline flow controller. To operate, the radio frequency (RF) power is slowly raised to 100W while its impedance is

Figure 2.5: This picture shows a plasma source outside its housing.

simultaneously matched, so that the power being produced by the system is not reflected back into the power supply. The RF power display is shown in Figure 2.7. After 100W was reached on the power source, the N_2 *flow valve* (which allows gas flow from the container) was opened and the *leak valve* (which lets the gas into the growth chamber) was loosened. It is important to note that this step takes place after the RF power is brought up to a minimal operating power so that the nitrogen in the environment is *only* active nitrogen (albeit a small amount in comparison). During the opening of the leak valve, the vacuum pressure must be monitored so that a sufficiently low-pressure environment is maintained with the flow of nitrogen into the growth chamber–roughly $5x10^{-9}$ Torr. After this has been done, the RF power must be brought up to create the plasma, while maintaining a minimal reflected power through impedance matching. Once the power is sufficiently high, a nitrogen plasma strikes, shown in Figure 2.8, which causes a spike in the amount of active-

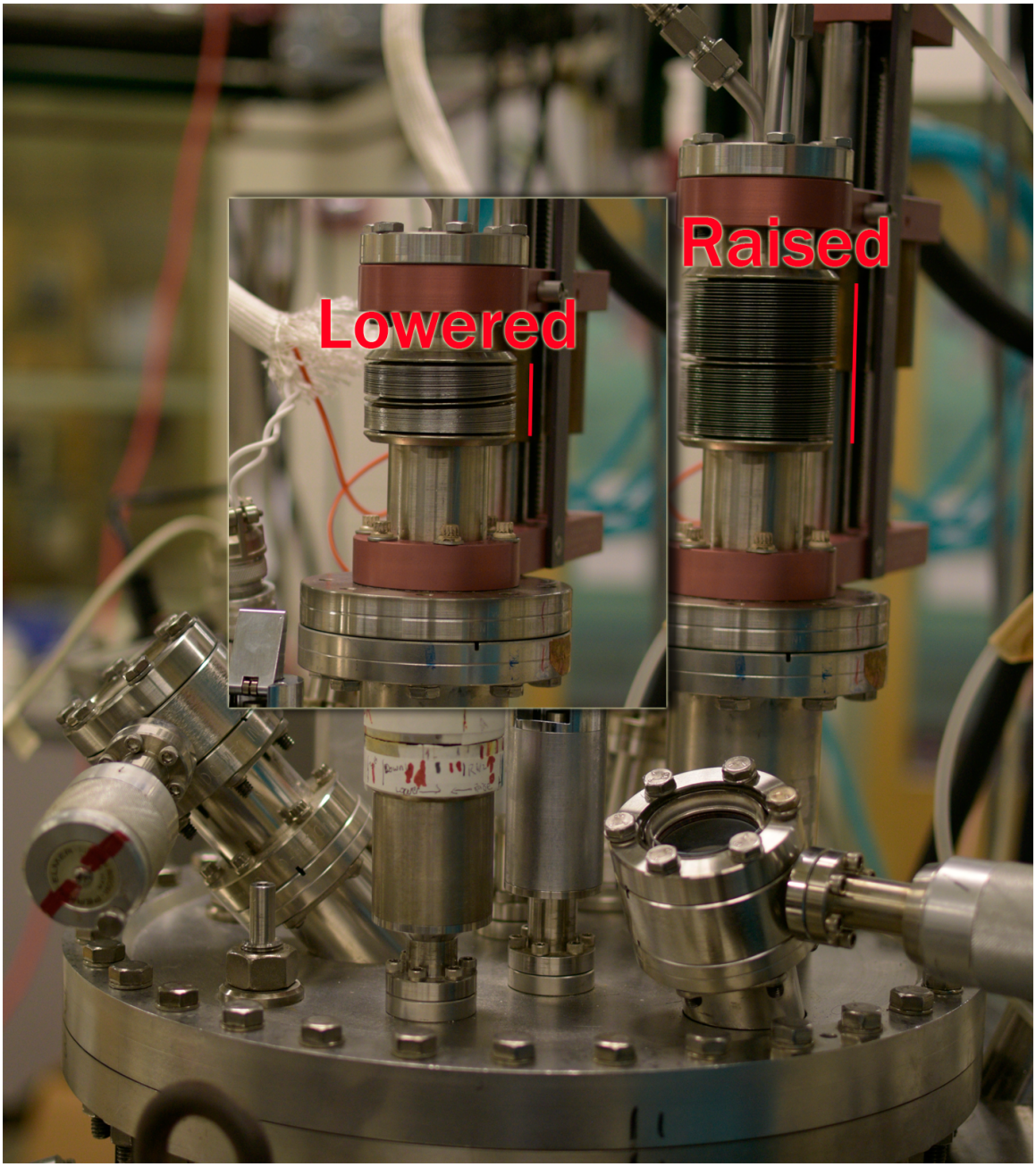

Figure 2.6: The two positions of the quartz crystal monitor are depicted here, highlighted by the red bar to denote relative heights with respect to each other. The inset shows the QCM in the lowered position, used for flux measurements, while the outset depicts the raised position, when the QCM is not in use.

Figure 2.7: This picture shows the forward and reflected power displays.

nitrogen present in the environment, and inducing a pink-colored, high-brightness mode plasma emission. The charge-coupling of this active-nitrogen to the RF power causes a large amount of the power to be reflected back into the system, so the power must be immediately reduced and impedance-matched using a set of knobs, so that the nitrogen plasma is maintained while minimizing the reflected power–generally down to 150W, assuming "high-brightness mode" plasma was struck at a higher RF power. With the growth environment fully prepared, the N_2 shutter is briefly closed while the sample holder is turned back around, exposing the substrate to the K-cells and the plasma source. Finally, the substrate growth orientation is set and verified via RHEED, and all three shutters–Zn, Sn and N_2–are primed for simultaneous opening to start growth.

2.2.2 Notes on Film Growth

Under normal circumstances corresponding to the growth of traditional III-V semiconductors, there exists only a single cation on the cation sublattice. Consequently, one can simply vary the metal flux to optimize the growth rate. Because there are two metals present on the cation sublattice in this $ZnSnN_2$ system, varying the fluxes of

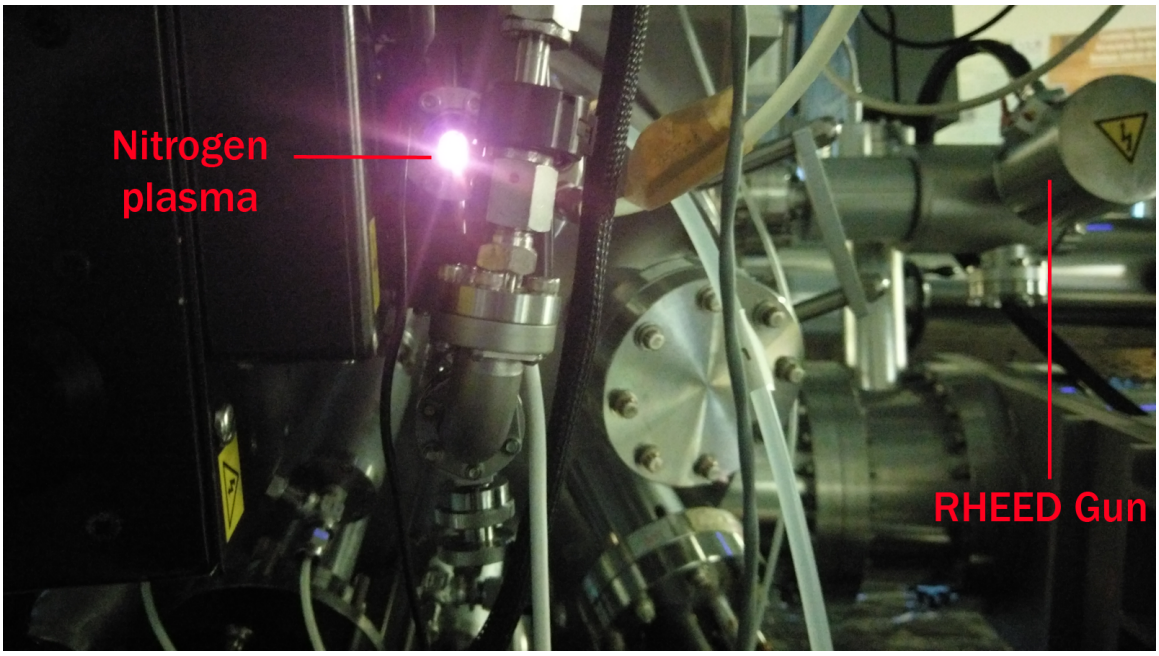

Figure 2.8: This picture shows the nitrogen plasma which has been struck. Generally, the "high-brightness mode" mentioned is much brighter than this and imposes unfavorable conditions on the system which must be addressed immediately; thus no HBM is shown.

both zinc and tin creates a much more complex situation. To minimize this complexity, the metal fluxes were held constant at conditions where previous runs had resulted in monocrystalline films. The substrate temperature was also held constant and was chosen with the same motivation, namely to achieve high quality, monocrystalline films. Films were grown at varying nitrogen flow rates to determine the optimal parameters for which the growth of the orthorhombic phase of $ZnSnN_2$ would be most ordered. Reflection high-energy electron diffraction (RHEED) was employed in-situ to monitor film quality, crystal structure, and film thickness approximation during growth. Note that for some runs, circular streaks may appear during RHEED analysis, due to the isotropic nature of inelasticallly scattered electrons off the surface of the substrate lattice. These streaks, referred to as "Kikuchi lines", are generally a desirable condition and are indicative of coherent diffraction conditions.

2.2.3 Application Potential of ZSN Quantum Well Structures

A quantum well is a 2-dimensional structure that consists of a low-band-gap material confined between two high-band-gap materials. Of particular interest to this dissertation, the benefit to growing a quantum well lies in its ability to confine the electron wave function, which allows for a more controlled optoelectronic response from the material. It is important also to point out that the versatility of the II-IV-V compounds provides a very interesting and useful way to fabricate QW structures. Additionally, this type of structure is well-suited to the growth of ZSN using MBE, due to the ability to select the band gap using the same chemical constituents, while altering the cation ordering within the layers of the film that is being grown. For instance, the low gap can be used for the well region while the high gap is used for the confining layers on either side of the well. Best of all, the MBE growth parameters can easily be changed to fabricate the well layer *and* the confining layers, all in a single growth run. This iso-compositional quantum well is highly unusual and is made possible by the allotropic nature of the ZSN system. Another example of this is the case of BN which can exist in either a hexagonal phase or a cubic phase[30].

CHAPTER III

Characterization Methods

This chapter will review some of the overarching concepts for each of the characterization methods used, as well as what can be learned from each technique. Topics will be discussed in the general order that the experiments were conducted. They include: Reflection High-Energy Electron Diffraction (RHEED), X-Ray Diffraction (XRD), Diffuse Reflection Spectroscopy (DRS), Photoluminescence (PL), Hall Effect, and Cathodoluminescence (CL) measurements.

3.1 What is Diffraction?

One of the most striking features of waves is how they tend to interact with objects within their path. Particles like electrons and photons, which have wave-like attributes, abide by these same principles and may be exploited to characterize a sample of interest. RHEED and XRD, which utilize electrons and photons (respectively), both take advantage of this wave-like behavior and are commonly used in materials characterization. Diffraction is the bending of a wave around an object within that wave's path. A simple yet pertinent example of this is depicted in Figure 3.1, where a plane wave of some wavelength λ encounters a single slit of width d while moving from left to right. The wavefront penetrates the slit, resulting in a difference in path lengths as the wave continues through the slit to impinge on a screen. This differ-

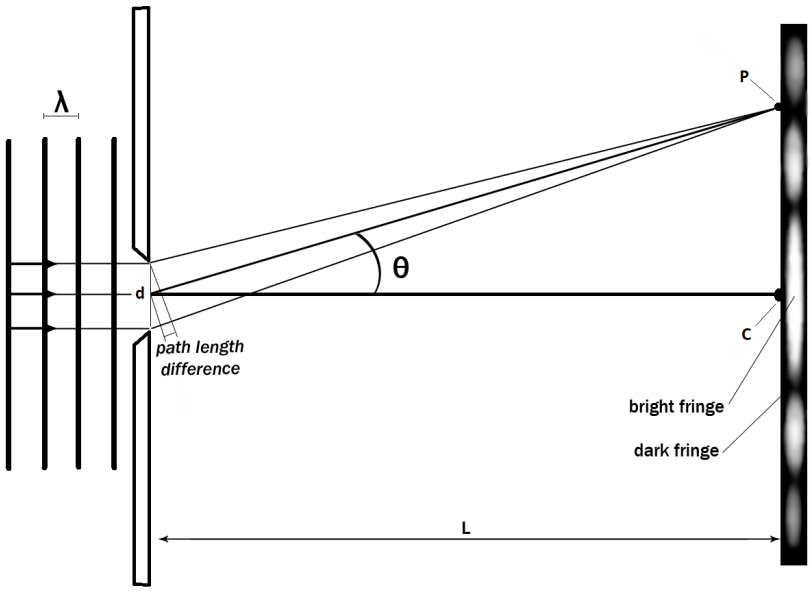

Figure 3.1: A schematic of single-slit diffraction.

ence in path lengths from the slit to the point P causes constructive and destructive interference to occur; thus, when observing the screen behind the slit the observer will see a pattern of bright and dark fringes, which delineates the constructive and destructive interferences, respectively. The spacing of these fringes depends on the distance L between the slit and observation screen, and on the width d of the slit. Mathematically, we can locate the centers of the dark spots by measuring the angle θ between two lines: one originating at the slit's center and extending to center of the observation screen, C, and the other extending to the point of interest, P. With a few extra steps, we can come to the conclusion that a smaller slit increases the spacing between the fringes, while a larger slit decreases the fringe spacing.

On the atomic scale, there are a few key differences compared to the simple optical example illustrated in Figure 3.1. Most importantly, high-energy electrons and photons share the trait that their wavelengths are sufficiently small for them for interact with the spacing of the atoms in a solid.

3.1.1 RHEED

Reflection High-Energy Electron Diffraction, or RHEED, is often used to characterize crystalline materials *in-situ* during and/or immediately after growth, prior to removal from the growth environment; this is referred to as *in situ* characterization. By exploiting the wave nature of electrons, accurate analysis of a material can begin prior to any other characterization methods. Perhaps one of the best advantages of using a RHEED system is the opportunity for analysis of the film *during* growth which, if taken advantage of early enough, allows for on-the-fly adjustments to the growth conditions without having to fully restart the growth or change out the substrate. When paired with software packages like KSA 400, developed by k-Space Associates, Inc., it becomes an even more powerful tool for providing key insights on the effects of various growth conditions, as well as contributing vital information to predictions on growth rates. RHEED patterns usually include both the specularly reflected beam (by total external reflection) and diffracted beams. The first may not be visible to the detector depending on the physical location and orientation of the sample on the substrate holder, but when oriented correctly, the specular beam appears as a small bright dot; the diffracted beam carries the information about the sample's surface structure, with only the uppermost two or three atomic layers typiclaly contributing to the RHEED pattern, depending on the angle of incidence.

RHEED images, like the one in Figure 3.2, are the "raw data" of any RHEED experiment. But to obtain them, a relatively high current, 1-2 A, must first be passed through a tungsten filament which has a low work function. The electrons are then drawn from the tungsten filament into a beam (focused down via a combination of electrostatic and magnetic lenses) by means of an anode positively-biased at a high voltage, generally between 10 and 30 kilovolts (kV). The electron beam is then diffracted by the atoms at the surface of the sample (which is mounted on a heated wafer holder), and reflected off at a low ($< 1°$) angle of incidence, resulting in both a

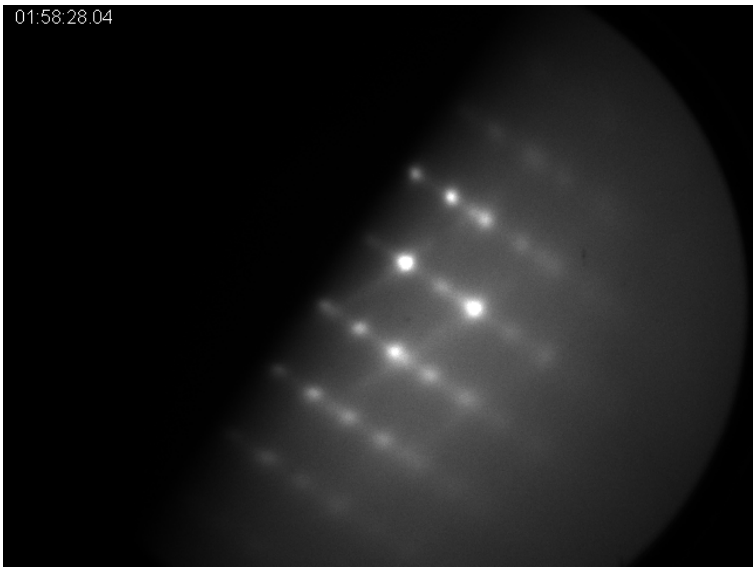

Figure 3.2: This RHEED pattern was captured with a CCD camera during an early attempt at the growth of $ZnSnN_2$ before the correct growth conditions for a smooth, epitaxial film were established. The spotty appearance of the RHEED pattern indicates the presence of 3D crystallites on the surface. The phosphor screen actually luminesces as the emission of green light from the electron interaction.(See Figure 3.3)

specular and a diffracted beam. To preserve the clearest possible resolution, the focal point of the beam is chosen to be at the detector–a phosphor screen (see Figure 3.3) which luminesces upon electron interaction. Finally, a charge-coupled device (CCD) camera detects the light emitted from the phosphor screen, is digitized and fed into a computer which reproduces the data as an image using the KSA 400 RHEED data acquisition software.

As a result of the high accelerating voltages used, these electrons have very high energy and are only able to interact with the top few layers of atoms before they are reflected off of the surface of the growing film. Consequently, RHEED is extremely surface-sensitive and it is imperative that the substrate surface is clean before growth, otherwise the RHEED data acquired (if any) may not be reliable. Predictably, one of the foremost characteristics visible in RHEED data is the roughness (or smoothness) of the sample. Typical values for the surface roughness in MBE growth of these

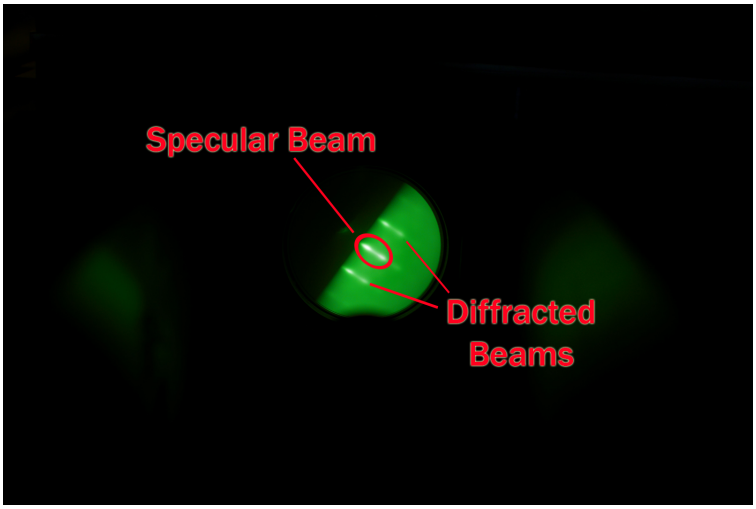

Figure 3.3: An image of a RHEED pattern using a phosphor screen as a detector. Electron interaction causes the screen to luminesce. In this image, one can see both specular and diffracted beams.

films are $\sim$ 0.5 nm, as determined from Atomic Force Microscopy (AFM) images. At the beginning of the growth, the deposition of atomic layers can be witnessed as an oscillation of streak intensities in the RHEED pattern. The completion of each monolayer leads to a minimum (or maximum) of the diffracted intensity, depending on whether the intensity is measured at a Bragg or anti-Bragg position. Typical growth rates are 0.2 monolayers per second. In Section 1.2.3, the periodic nature of crystal structures was discussed. It is this periodicity, or lack thereof, which causes the diffracted beam to appear as a series of either streaks or dots, depending on the actual surface structure. With this information the smoothness of the film can be deduced along with whether the film is single-crystal or polycrystalline. Each resulting diffraction pattern is unique to the *surface* structure of that material. When a surface is terraced but otherwise very smooth, the diffracted beams will appear as streaks, denoting a lack of pronounced 3D structures (e.g., crystallites) protruding from the surface in the growth direction. This type of qualitative analysis is typically used to "prescreen" a substrate prior to initiating growth. After growth has been initiated, additional information about the film growth and its structure can be obtained from

the RHEED pattern, including the spacing between rows of atoms on the surface, the coherence length of the surface atomic structure (determined from the transverse width of the RHEED peaks) and, most importantly, a quantitative measure of the order parameter.

3.1.2 Determination of the Degree of Ordering in ZnSnN_2

As shown by Makin et al. [15] a quantitative measure of the degree of cation ordering in ZSN can be expressed as an order parameter, S, defined as

$$S = r_\alpha + r_\beta - 1, \tag{3.1}$$

where r_α is the fraction of Zn sites occupied by a Zn atom and r_β is the fraction of Sn sites occupied by a Sn atom. Thus S = 0 corresponds to randomly occupied cation sites and S = 1 corresponds to a fully ordered cation arrangement. S is commonly measured by a scattering experiment, either with x-rays or electrons (RHEED)[31], such that $|F_{hkl}| = AS + B$, where $|F_{hkl}|$ is a structure factor that is sensitive to the cation ordering. A is a constant representing the atomic scattering factors of both Zn and Sn atoms, and B is a constant representing the atomic scattering factor of nitrogen atoms. $|F_{hkl}|$ is chosen to be that of a superlattice reflection, $|F_{210}|$ in this case.

For x-rays $|F_{210}|$ includes geometric corrections for the polarization of the x-ray beam, incident on the (210) planes at an angle of θ:

$$|F_{210}|^2 = \frac{E_{210}F_{002}^2[\frac{1+\cos^2 2\theta_{002}}{2\sin 2\theta_{002}}]e^{-2M_{002}}}{E_{002}[\frac{1+\cos^2 2\theta_{210}}{2\sin 2\theta_{210}}]e^{-2M_{210}}}, \tag{3.2}$$

where $|E_{210}|$ is the integrated intensity of the (210) superlattice reflection, and M_{hkl} is a Debye-Waller factor to correct for the effects of atomic vibration. The superlattice structure factor is normalized to a reflection (002) that is insensitive to cation

ordering.

For electrons (RHEED), the order parameter is similarly determined from the integrated intensity ratio of the (210) and (002) reflections. We obtained excellent agreement between the values of S determined by both x-ray diffraction and by RHEED[15]. RHEED was particularly useful for this study because the RHEED pattern is readily available during growth of the thin films and it was immediately apparent to what extent each sample was ordered by visual inspection of the RHEED pattern along the (210) zone axis.

3.1.3 X-Ray Diffraction

3.1.3.1 An Historical Synopsis

In 1895, German physicist Wilhelm Roentgen discovered an invisible type of radiation with exceptionally short wavelengths, in comparison to visible light. These mysterious "X-rays", as they were dubbed, were electromagnetic by nature and could easily penetrate most objects. Though they were not well understood at the time, their utility was immediately capitalized upon as a means to see through or inside of normally opaque materials, including broken bones within the body or cracks within a metal casting. The capacity to see minute details inside of a material without physical deformation it was a major breakthrough not only for scientific discovery, but also for more accurate diagnoses and analytical studies in medicine. But the extent of the resolution achievable by X-rays far exceeds the millimeter-scale (10^{-3}) generally seen in medicine. In 1912 the true nature of X-rays was confirmed which led to the discovery of *diffraction* by crystals. This opened up an entirely new basis and methodology for material analysis. Today, using X-ray diffraction, scientists can study structural phenomena on the atomic scale of angstroms (10^{-10}m).

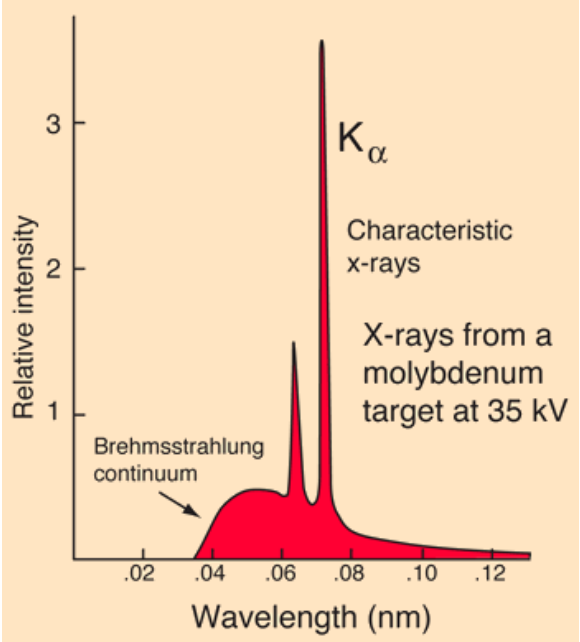

Figure 3.4: This is a generalized depiction of the difference between bremmstrahlung and K-α X-ray emission spectra. The unmarked peak to the left of the K-α peak is an example of a K-β peak and is also characteristic of the target metal[32].

3.1.3.2 X-ray Production

X-rays are produced in one of two ways: 1) when highly energetic electrons decelerate as they collide with a metal surface, known as "bremsstrahlung radiation," or 2) when electrons radiatively relax from high-energy atomic orbitals to a low-energy orbitals, also known as "K-α radiation." In the former method, electrons are deflected by the strong electric fields produced within atoms by high-Z nuclei in metals, like copper or molybdenum. The maximum energy is released when an electron is fully decelerated by a single collision. Some of the electrons experience multiple collisions before releasing all of their energy; thus emitting gradually less and less per collision. This results in a continuous spectrum, similar to white light in the visible regime, whose total energy "depends on the atomic number of the metal target, Z, and the tube current"[33]. However, in the latter method which was used for this study, the collision causes inner-orbital electrons within the metal atoms to be ejected, open-

Figure 3.5: A Bird's eye view of the Advanced Photon Source facility at Argonne National Laboratory[36].

ing up vacancies that can be filled by outer-orbital electrons. This movement from a higher to lower energy state releases energy in the form of electromagnetic radiation of precisely the energy difference between the two orbitals. In contrast, this results in very sharp peaks in energy spectrum at much higher intensities than in bremmstrahlung radiation[32]. See Figure 3.4.

3.1.3.3 The Advanced Photon Source (APS)

The Advanced Photon Source (APS) at Argonne National Lab (ANL) is this hemisphere's leading producer of high-brilliance, high-energy X-rays. Year-round, thousands of experiments are conducted at the facility for a wide variety of research projects, ranging from improvements to fuel-injector efficiencies[34] to studying how certain plant viruses replicate[35], originating from multiple institutions that span across various disciplines and industries. Researchers prize this brilliance so much because of the level of precision that is achieveable with such high-energy photons.

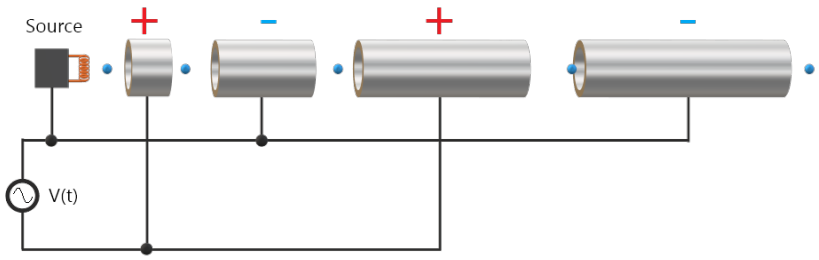

Figure 3.6: A basic schematic of a linear accelerator showing the electrons (blue) accelerating through a series of RF cavities which produce electric fields of alternating polarization.

3.1.3.4 The Linear Accelerator (LINAC)

At the heart of the APS lies the linear accelerator (LINAC), depicted in Figure 3.6, which first emits the electrons via thermionic emission, by heating a tungsten cathode up to 1100°C. Next these electrons are accelerated to relativistic speeds (99.999% of the speed of light) by a series of alternating electric fields to an energy of 450 MeV before being further accelerated by the booster synchrotron to 7 GeV (99.999999% of the speed of light) in less than one second. The electrons are then injected into a 1104-meter circular storage ring, which consists of over 1000 electromagnets that focus the beam and minimize divergence, all housed within a concrete enclosure inside the experimental hall–the circumference of which would surround the White Sox's stadium, in Chicago! Insertion devices provide researchers with access to this storage ring via 35 different beamline sectors tangentially situated around the circumference(see Figure 3.7).

3.1.3.5 What We Can Learn From XRD

Due to the wave-nature of photons, X-rays retain their characteristic information while bending around objects in their path [see Section 3.1]; in the case of XRD, these

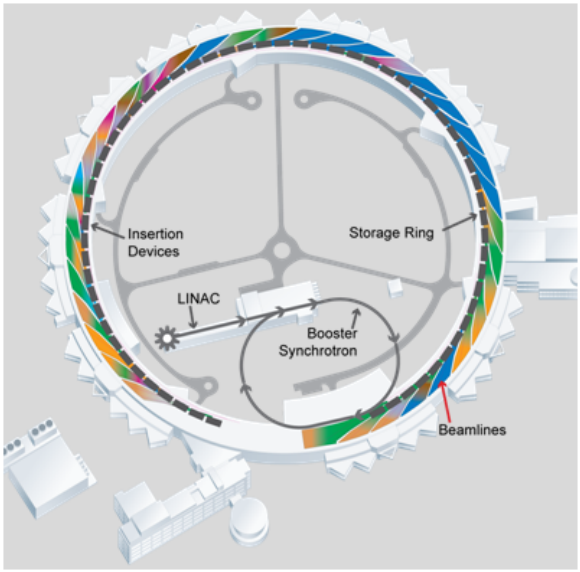

Figure 3.7: Beamlines are located tangentially to the storage ring and are divided into 35 different sectors accessible to scientists for research at each insertion device[37].

objects are atoms within a crystal lattice. With these high-energy photons, one may conduct diffraction peak experiments, which result in $\theta - 2\theta$ plots of photon intensity, which provides information about the lattice constants and structure factor of a crystalline or polycrystalline material. By spreading the beam out in one direction, a series of areal scans may be taken to map the reciprocal space along a particular (hkl)-direction. When stacked and rendered properly, these 2D scans can generate 3D reciprocal space maps (3D RSMs), which can then be used to accurately determine the type of crystal structure present, based on the symmetries and associated Bragg peaks, given the constructive and destructive interference rule sets for a particular space group.

For this project, X-ray diffraction was used to verify the structures and lattice constants of ZSN thin-film's[12] and to quantitatively measure the associated order parameter, S, for each film[13], as described in Section 3.1.2. These experiments assisted in providing and corroborating the expected values for the band gaps of wurtzite and orthorhombic films, which will be discussed later as a comparison to the

values experimentally determined in this dissertation.

3.2 Spectroscopy

Spectroscopy is the study of how a material responds to a given type of radiation. The data acquired from spectroscopic experiments are often presented in the form of a spectrum that shows how the measured quantity changes as a function of the probing wavelength. The source of the radiation may vary depending on the type of experiment being conducted and the quantity of interest being measured. For this project, where determination of the optical band-edge is the main interest, the spectroscopy techniques employed utilized light sources from a broadband lamp, for diffuse reflectance, and stimulated emission (a laser) for photoluminescence. Energetic electrons were also used to excite optical emission from several samples in a technique referred to as "cathodoluminescence" (CL). These types of techniques are often referred to as pump-probe experiments, which entail “pumping” a sample with light or electrons and using a detector to “probe” the light that emanates from the sample as a result of that pumping.

Optical spectrometers, like the ones used in this experiment, detect the intensity of light as a function of wavelength after it has been reflected off, or transmitted through, a material of interest. In short, diffuse reflectance spectroscopy (DRS) is able to determine how a semiconducting material responds at each wavelength to a light source of many wavelengths and thus to measure the optical band-gap[38, 39]. The wavelength (or energy) corresponding to the band-gap is denoted by a sharp drop in the reflectance at shorter wavelengths where strong absorption of the incident light occurs (see Figure 3.8). To perform DRS, optical spectrometers take advantage of the wave nature of light by splitting the detected light into many wavelengths using a diffraction grating to create a spectrum that is indicative of the material’s response. When one compares this reflectance spectrum to that of the incident light,

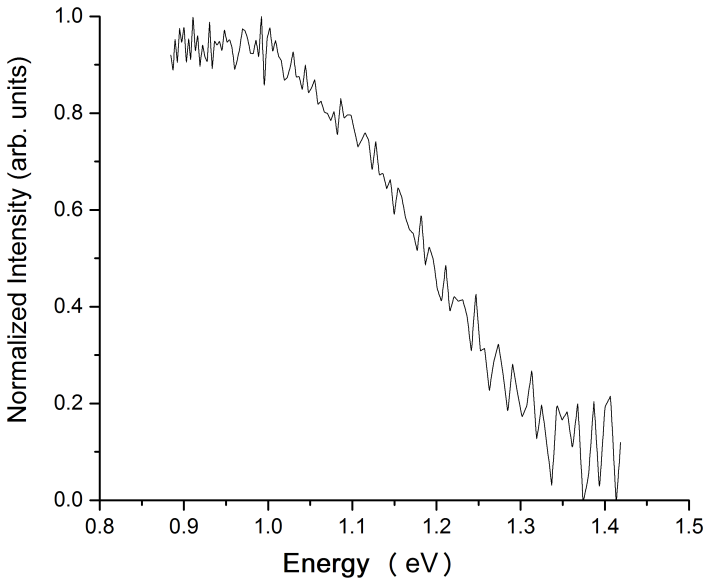

Figure 3.8: Here a reflectance spectrum for wurtzite sample WPI91A is depicted. This illustrates the absorption of photons whose energies exceed the optical band gap of the ZSN thin film ($\sim$ 1.3 eV in this case).

it is possible to discern fairly precisely (within about 0.1 eV) the location of the optical band gap energy.

3.2.1 Diffuse Reflectance Spectroscopy

Diffuse Reflectance Spectroscopy, or DRS, provides a way to probe the optical response of a thin film by diffusely reflecting broadband light from the back surface of the film. The light enters the front surface of the film and the diffusely scattered light is transmitted through the film from the back surface. For a wave or particle to be diffusely reflected, it should be reflected at an angle different from which it was incident upon the surface, that is, non-specularly. By characterizing the reflected light, one can gather information about the surface's absorptive and reflective properties. If a material reflects perfectly diffusely, it is said to be Lambertian, meaning that the reflected light is reflected in equal proportion in all directions on the same side of the

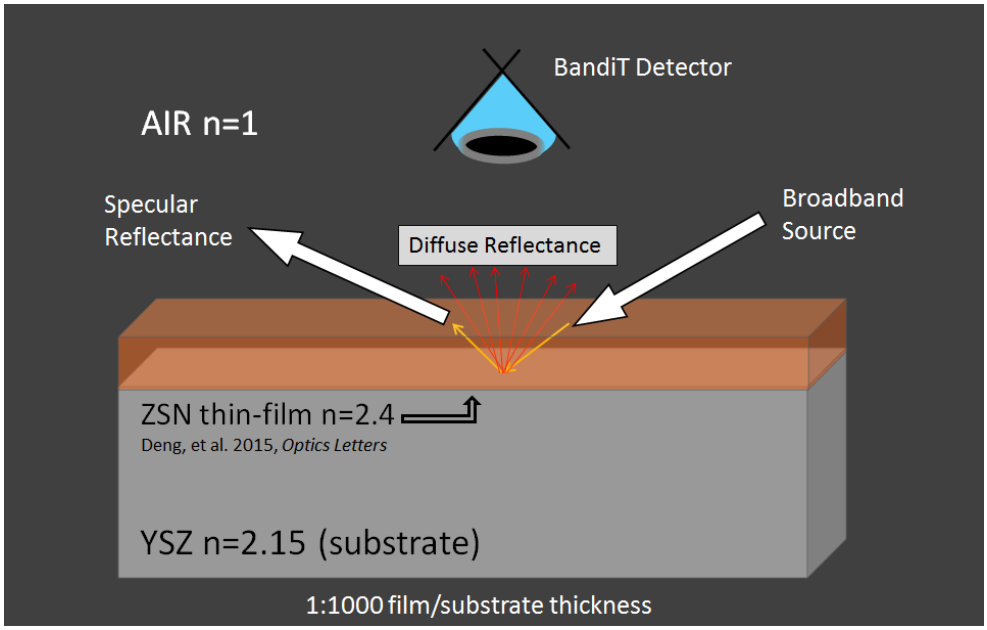

Figure 3.9: A traditional diffuse reflectance schematic.

surface as the incident light. While much of a surface's reflectivity has to do with surface roughness, it should also be noted that just because a surface is well-polished doesn't mean it will reflect just like a mirror. Mirrors reflect close to 100% of incident light, thus there is little or no diffuse reflection from them. However, consider a polished gray slab of marble which provides a reflection. In this case, the marble still appears gray to you because some of the light is being diffusely reflected. As shown in Figure 3.9, diffuse scattering occurs due to scattering that happens BELOW the surface of the material. Incident light penetrates the surface and scatters off of other interfaces that lie beneath the polished (or unpolished) surface. The deeper the light penetrates, the more diffusely it will be scattered, because there are more scattering centers it will encounter upon its return to and out of the surface as a reflected ray.

There are two important interfaces to take note of: the air-sample interface as well as the sample-substrate interface. At both of these interfaces, some of the incident photons get reflected back toward the surface of the sample. Throughout the travel time of the photons which make it all the way through the material to the back

surface, there exists a chance that some of these photons will still be absorbed by the material during their return path toward the sample surface. This is also depicted in Figure 3.9.

3.2.2 A New Method: Waveguided Diffuse Reflectance Spectroscopy

Most samples of our very thin films (100 nm or less) showed only weak absorption edges when measured via the traditional method, while others didn't show any. As the experiment evolved, certain known issues began to surface as likely factors for the low or complete lack of signal from the films. One of these early issues was that the area of the beam spot was too large resulting in low incident light intensity. While the original setup contained an optic fiber coupled to a fixed collimating lens, this was soon modified to instead include a microscope lens, which reduced the spot size to roughly 1 mm in diameter. However this complicated the experiment since the sample would now have to be situated at the proper focal length to avoid loss of incident intensity due to beam divergence. This created the need for fine control of the sample placement, upon which the setup was further modified to include a 3-axis sample-mounting plate with thumbknob micro-adjusters. Due to the new small spot size, it would be more difficult to obtain good spatial coverage of the sample.

To achieve this coverage we devised a novel approach, which we refer to as Waveguided Diffuse Reflectance Spectroscopy (or WDRS), that was specifically designed for DRS measurements on extremely thin films (< 100 nm). By focusing a beam of broadband light into the sample at below the perceived critical angle, we could minimize specular reflections, while still acquiring multiple internal reflections off of the sample surfaces for spectroscopic study with various spectrometers spanning the visible and IR regions. Other minor adjustments were made to this new setup including: the blackening of the mounting surface (for the sample) to reduce external scattering, and the vertical placement of the detection fiber to minimize detection of stray light

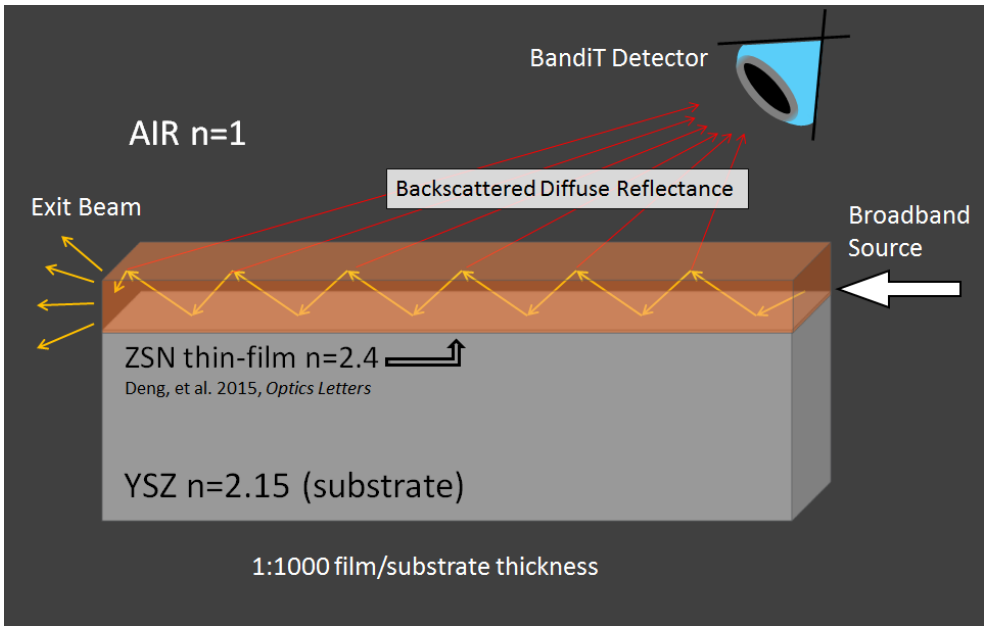

Figure 3.10: A waveguide diffuse reflectance schematic.

(see Figure 3.10).

The end result was that WDRS spectroscopy was demonstrated, but it is still difficult to setup in a controlled environment, due to various issues including very small sample thickness (<100 nm), Fabry-Perot effects, etc. However, the benefits to this technique are as follows: it makes band edge measurements possible at low spectral reflectivity, it provides greater probabilty of photon absorption than at higher incident angles, it creates much longer path lengths for photons within the plane of the film, and overall it improves contrast above and below the optical band gap. To summarize, Waveguided DRS is based on the premise of utilizing the two surfaces of the film as a waveguide so that multple points of glancing angle internal reflection are created so that the path length for absorption is maximized compared to the normal single-pass geometry of DRS.

3.2.3 Photoluminescence

Photoluminescence spectroscopy is the study of a material's emissive properties upon exposure to light. When some types of material, for example semiconductors, absorb light, the incident photons can cause electron transitions from lower-energy states to higher-energy states within the material if the photons have sufficient energy. It is not, however, energetically favorable for the electron to stay in this new state, and so it quickly (within femtoseconds) transitions down to some lower-energy state. When electron-hole recombination occurs a photon may be emitted, and we say that the material luminesces. This phenomenon is commonly used in spectroscopy to probe either the band edge of or defect states within the gap of semiconducting materials. In a basic photoluminescence spectroscopy experiment there are three major components: the light source, the sample of interest, and the detector. Photoluminescence is a photonic pump-probe experiment, which means that the photons are used as the energy source to cause some type of perturbation, or change, within the sample. Quantum mechanically, photoluminescence (or PL), is a 3-step process that requires the *absorption* of photons by a material's valence band electrons, the consequent *excitation* of those valence band electrons into the conduction band, and the subsequent *spontaneous emission* of new photons as a result of the conduction band electrons relaxing back down to the valence band or some other lower-energy state. Fermi's Golden Rule which governs the transition rates states that

$$\frac{2\pi}{\hbar}| < f^* | \hat{H}' | i > |^2 \delta(E_f - E_i - E), \tag{3.3}$$

where $\hat{H}'$ is given by the Hamiltonian of the electric field of the incident photons, i and f are the initial and final states, respectively, and E is the amount of energy absorbed from the incident photon by the valence band electron. The occupation probablilities for the initial and final states f_f(E) and f_i(E) are given by the Fermi-

Dirac distribution function which represents the probability that an electron exists in a given energy state. This perturbation causes the light to be reflected with a "new signature" as compared to its spectrum prior to sample interaction. In a linear process, the incident photon energy must be greater than the transition energy that one is probing. The PL light is incident on a photodetector, digitized, and then usually read out by a computer for spectral analysis. While this is a more generalized explanation of a photoluminescence setup, the details on the specific setup employed for this project will be spelled out later, in Section 4.2.3.

Thermalisation is the process by which one object interacts with another, bringing it to thermal equilibrium with its environment upon said interaction. In this case photon energy is converted into thermal vibrations (phonon energy) and may cause unintended recombination of electrons and holes. This counteracts radiative recombination by increasing the density of states between the valence and conduction bands, called "intermediate states," allowing for faster inter-band transitions. These types of transitions usually do not emit photons and are known as non-radiative recombination. By performing measurements at extremely low temperatures, thermalisation can be circumvented, prolonging the lifetime of electrons in the conduction band and increasing the probablility that they will radiatively recombine with holes.

3.2.4 Quantum Confinement

In addition to the study of single-layer ZSN thin films, ZSN quantum wells (QW), the first of their kind, were examined using photoluminescence. The nature of quantum confinement can be best understood by the well-known particle-in-a-box model. In it we consider a free particle oscillating back and forth while trapped in between two impenetrable walls of infinite height. These walls represent the potential energy barrier faced by particle, with the well portion having zero potential energy, $V(x) = 0$, and being of total width $x = L$. The wavefunction of this particle confined within

the well can be found by solving (for simplicity) the time-independent Schroedinger equation for the system given by:

$$\frac{-\hbar^2}{2m}\frac{d^2\psi}{dx^2} = E\psi, \tag{3.4}$$

where $\hbar$ is Planck's constant, m is the particle effective mass, and E is the energy (or eigenenergy) associated with a given wavefunction (or eigenstate), ψ. The solutions to this equation, a mixture of sines and cosines,

$$\psi(x) = Asinkx + Bcoskx, \tag{3.5}$$

where A and B are constants, impose a strict set of boundary conditions on the eigenenergies. Specifically, since $\psi = 0$ at the edges of the infinite well, the value k must take on integer multiples of π/L,

$$k_n = \frac{n\pi}{L}, n = 1, 2, 3, ... \tag{3.6}$$

so that the allowed eigenenergies become

$$E_n = \frac{n^2\pi^2\hbar^2}{2mL^2}. \tag{3.7}$$

In the real world, quantum wells do not have infinite potential barriers, but the results of this modification do not change the simplicity of the numerical analysis. These energies still correspond to the allowed transitions between the ground state (n = 0) and the excited states (n > 0). As such, we have used this simple model in Section 4.2.4 to predict the expected transistion energies for ZSN QWs of various widths grown via MBE.

3.3 Electrical Measurements: Hall Effect

Characterizing the degree to which a conducting material is able to transport charge is essential to gaining a better understanding of the the type and magnitude of the band-gap, the charge carriers, and their mobility. Thus the beauty of the Hall effect, which was discovered by Edwin Hall in 1879, is the simplicity with which charge transport may be observed in the lab when compared to the diverse information that the method provides. The Hall effect occurs when a moving charge is deflected transversely toward one edge of a conducting (or semiconducting) material by a uniform magnetic field applied at normal incidence to the surface of the material. A depiction is given in Figure 3.11. The relation between this field and the resultant force experienced by the charge is given by the equation:

$$\hat{F_m} = q(\hat{v_d} \times \hat{B}) \tag{3.8}$$

This is known as the Lorentz force, where q is the charge in motion, $\hat{v_d}$ is the drift velocity of the moving charge, and $\hat{B}$ is the applied magnetic field. As the number of deflected charges accumulates on that edge, a transverse electric field, $\hat{E}$, is created due to the imbalance of charge on the opposing edge of the conductor. This new electric field applies a second force, $\hat{F_e}$, on the moving charges which opposes the force induced by the uniform magnetic field, until an equilibrium between the two is reached. The transverse voltage observed upon reaching equilibrium is known as the Hall voltage, V_H, and is given by:

$$V_H = E_{trans}(w), \tag{3.9}$$

where w is the width of the film or the separation of the transverse electrodes used to collect the magnetically deflected charges. This voltage was obtained empirically and

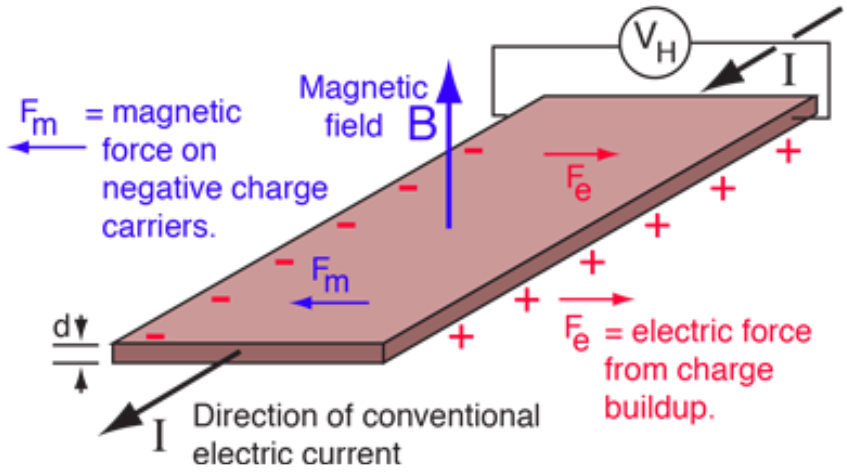

Figure 3.11: A depiction of the Hall Effect[32].

its sign reveals whether the moving charges are electrons or holes. In semiconductors, there are two possible types of charge carriers: electrons and holes, which are negatively and positively charged, respectively. Holes are the vacancies left behind, for example, when an electron transitions from the valence band to the conduction band. Taking this analysis a step further, the concentration of these carriers, n, can be extracted using the relation:

$$n = \frac{IB}{V_H de}. \tag{3.10}$$

Here I is the magnitude of the current, B is the magnitude of the magnetic field, d is the film thickness, and e is the carrier charge. If the carrier density in a material is above a certain threshold, the energy difference between those individual carrier states becomes such that one state is energetically indistiguishable from the next, thus degenerate. This happens when the carrier density is greater than roughly 10^{20} cm^{-3}. Given the carrier concentration, one can also calculate the mobility using:

$$\mu = \frac{1}{ne\rho}, \tag{3.11}$$

where ρ is the resistivity of the material. For photovoltaics, the mobility is one of the most important attributes of a semiconductor, since it is a measure of how quickly free charges are able to drift through the material and be collected by the contacts. As such, one can also express the mobility in terms of the velocity v_d by which those carriers are transported by the electric field E between the contact and the material (Equation 3.12).

$$\mu = \frac{v_d}{E}, \tag{3.12}$$

This so-called "drift velocity" has an important bearing on the *mean free path* of the carriers, which is a measure of the average distance a free charge may travel before being scattered. Around and above room temperatures, high-frequency phonon modes ($\sim 10^{-13}$ s^{-1}) can be populated, which have large scattering cross-sections; thus, the scattering events that occur are mostly dominated by electron-phonon interactions, which reduce mobility[1]. This reduction is further amplified by other contributions like high carrier concentrations and defect densities, which can lead to even shorter mean free paths. Practically speaking, this means that aspirant materials need to have some combination of low defect densities, low carrier concentrations, or long mean free paths (in comparison to material thickness) to excel in photovoltaic applications. In crystalline silicon, μ is around 1400 cm^2/Vs, while in amorphous silicon mobilities are observed as low as 0.01 cm^2/Vs. For bulk materials, like crystalline silicon, a short mean free path would be detrimental to efficient charge collection, but in thin films the impact may be tempered by the relatively short distance the charge needs to travel; thus, for a thin-film material like ZSN, the mobility of the material in thin film form is less critical than for bulk material.

The knowledge of these key electrical properties enables scientists to correlate the real-world transistions that take place within the band structure to the synthesis

parameters, providing unique insights to the material's viability as a component in commercial devices. The results from our measurement of ZSN thin-films (discussed in Section 4.3.1) fall between these values.

3.4 Cathodoluminescence

Cathodoluminescence (CL) is the excitation of optical luminescence by irradiation with energetic electrons in the range (0.5 - 5 keV). In some respects CL can be considered to be complementary to the more commonly used photoluminescence technique also used in our studies of ZSN thin-films (see Section 3.2.3). There are several key differences, however; first, the electrons used for optical excitation are much more energetic than the photon sources typically used for PL, which are commonly laser beams with photon energies in the UV-Vis range of a few eV; this enables data to be obtained over a wider range of photon energies than is typical in PL. Second, the high intensity of the electron gun sources used for CL is typically a few microamps (μA) focused in a beam that is only a few nanometers in diameter. This makes it possible to probe samples with much higher spatial resolution than is possible with PL on account of the ability to focus energetic electrons to spot sizes that are much smaller than a diffraction limited optical focus (wavelength $\sim 1\mu$m). While this provides a brief overview of the concept of CL, the details of this experiment have been reserved for Sections 4.4.1 and 4.4.2.

CHAPTER IV

Results & Discussion

Here we detail the setup and results for each experiment conducted, as well as a brief discussion of key results from each. Most of the results in this Chapter were submitted for publication and have now appeared in various journals. Specifically, band-gap tuning and demonstration that ordering is correlated with size of band-gap[15], growth of ZSN films and identification of growth parameters[13], demonstration of orthorhombic epitaxial films and structural confirmation[12], and the correlation between band gap and heterovalent cation ordering[14].

4.1 Diffraction Experiments

4.1.1 RHEED Setup

The growth of all ZSN films were measured *in situ* with a 20 kV Staib Instruments RHEED system at filament current around 1.3 A (shown in Figure 4.1) in tandem with a KSA 400 image acquisition and analysis package[13]. The kSA 400 (shown in Figure 4.2) couples directly onto to the viewport of the growth chamber via a set of screws. At the side of the kSA 400 is housed a CCD camera, which captures images of the phosphor screen seen in the top half of the image. Although the screen fluoresces green to the naked eye, the use of a monochrome CCD camera produces the black

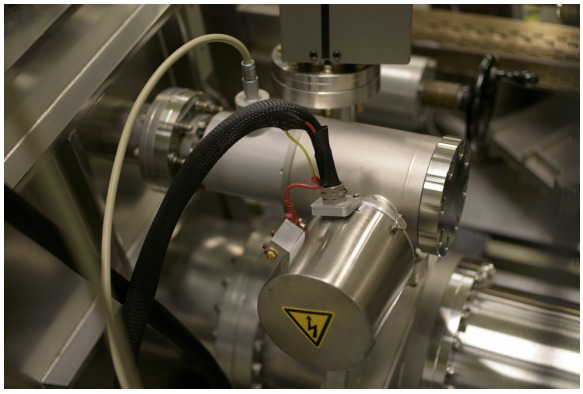

Figure 4.1: The 20 kV Staib Instruments RHEED gun is coupled to the growth chamber directly across from the kSA 400.

and white images commonly seen in RHEED images. A black cloth is draped over the entirety of the box to ensure the exclusion of stray light from the images.

Although the bulk of the RHEED images were taken in 1-30 second intervals during the early stages of film growth to capture the creation of the film-substrate interface, larger time intervals (10-30 minutes) were also used during the bulk of the growth time to monitor the quality of the film as it developed in thickness. This early-stage capture allowed for minor "on-the-fly" tweaks to be made to the growth parameters, and in a worst case scenario, it informed the need to abort the growth to conserve materials, in the event of a "bad," polycrystalline film. Although polycrystalline ZSN films have been purposefully synthesized and studied before[25], the focus of the project was to produce and study films that were free of these crystal domains; thus, growths that resulted in such "poly" films were not studied for the purpose of this project.

4.1.2 RHEED Results & Discussion

The diffraction of high-energy electrons off of a uniform crystal produces a specific set of reflections corresponding to the allowed scattering vectors in the reciprocal lattice[21]. These streaks are known as "Bragg rods" and can be seen in on the sample

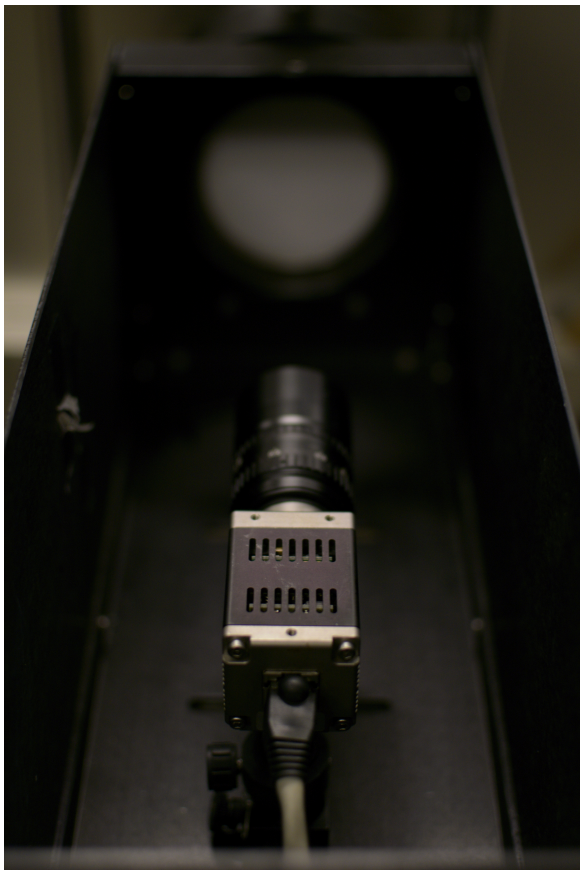

Figure 4.2: The kSA 400 houses a monochrome CCD camera which captures images of the phosphor screen seen in the top half of the image.

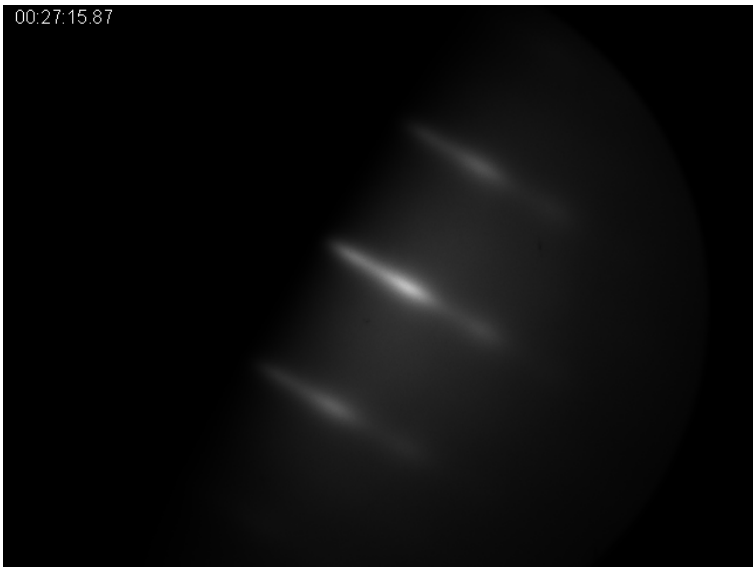

Figure 4.3: RHEED image of a film (WPI86) with a mostly smooth surface. RMS roughness ~ 0.5 nm.

shown in Figure 4.3 as a result of constructive interference. This rod-like pattern is a result of the uniformity of the crystal in the direction of growth (c-plane), i.e. a smooth surface.

If there is non-uniformity in the growth direction, these rods instead become broad spots as seen in Figure 4.4, indicating roughness on the surface caused due to the nucleation of 3D crystallites on the substrate surface. This may occur if the substrate temperatures are too low, resulting in limited surface migration of adatoms. Fortunately, if this is caught early enough, this can be easily corrected by pausing the growth and increasing the substrate temperature. This allows for more time for the completion of an atomic surface layer rather than the formation of surface crystallites.

The intent of the project was to synthesize single-crystal thin-films, but occasionally some polycrystalline films were unintentionally grown. This was particularly the case closer to the start of the project before the proper growth parameters were established. During that time, the growth rate was slower; thus, the majority of the RHEED data was acquired toward the conclusion of the growth rather than its

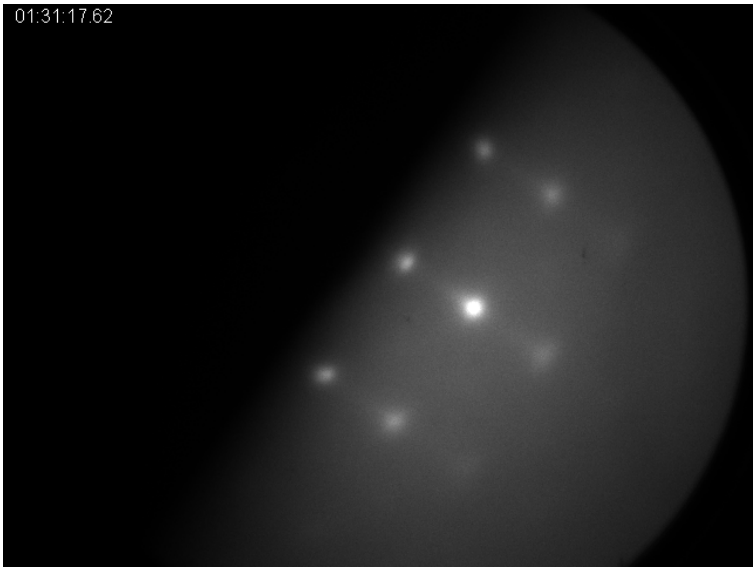

Figure 4.4: RHEED image of a film (WPI85) with a non-uniform surface.

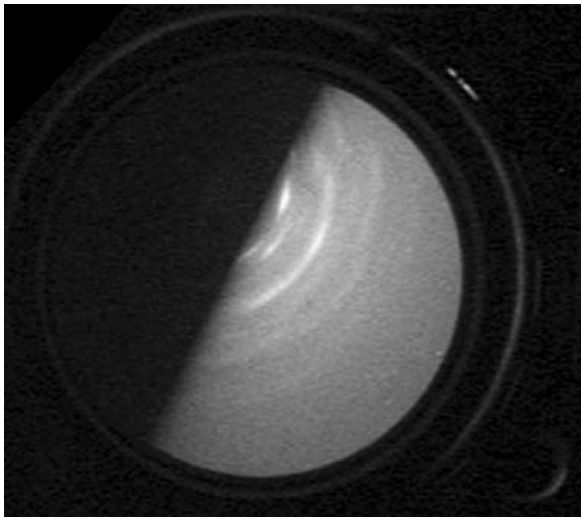

Figure 4.5: An example of a polycrystalline RHEED pattern created by GaN.[40]

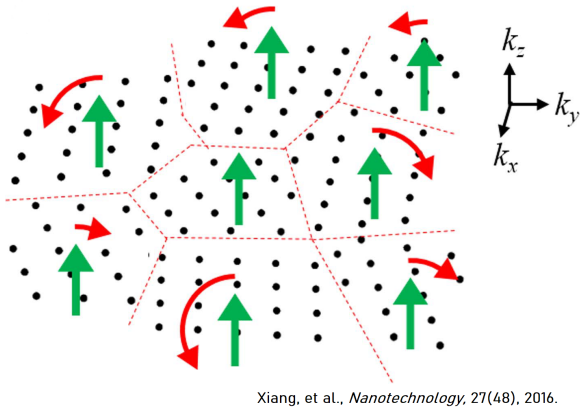

Figure 4.6: Here a polycrystalline structure is shown with randomly oriented crystal domains(red dotted lines). The green arrows denote the growth direction while the curved red arrows delineate the random crystal orientation per domain. Created by Xiang et al. [41].

beginning. This sometimes resulted in so-called "undesirable" films which displayed circular interference patterns on the RHEED images similar to that displayed by polycrystalline GaN in Figure 4.5.[40] This curvature denotes a directional invariance (or isotropy) of the film orientation on the diffraction pattern–a telltale sign of a polycrystalline film, in which a crystal is broken up by various domains of random orientations as is well-depicted by Xiang et al. [41] in Figure 4.6. After some refinement of the methodology and the growth rate, more detailed attention was given to the beginning of the growth so that it could be optimized to produce single-crystal thin-films of either the wurtzite or orthorhombic structure.

The most notable difference between these two structures is the size of the unit cell. As explained in Section 2.1, in a ZSN wurtzite crystal (see Figure 2.1) any given site on the cation sublattice may be occupied by either a Zn or Sn atom with equal probability (see Figure 4.7) [13]. A typical RHEED pattern acquired from such a film displays Bragg rods evenly spaced by an amount that corresponds to the reciprocal of the lattice spacing taken up by the unit cell. This can be clearly seen in Figure 4.9a.

In the orthorhombic state, however, cations are assigned to specific sites on the

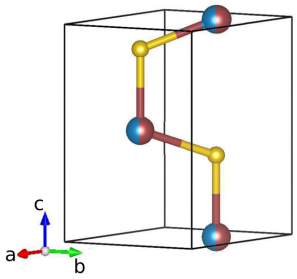

Figure 4.7: The wurtzite unit cell is depicted. Cation sublattice sites are populated randomly by either a Zn or Sn atom (shown in red and blue)[13]. *Image provided courtesy of Robert Makin, PhD.*

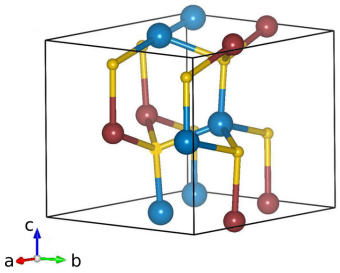

Figure 4.8: The orthorhombic unit cell is depicted, showing Zn and Sn atom site delegations[13]. *Image provided courtesy of Robert Makin, PhD.*

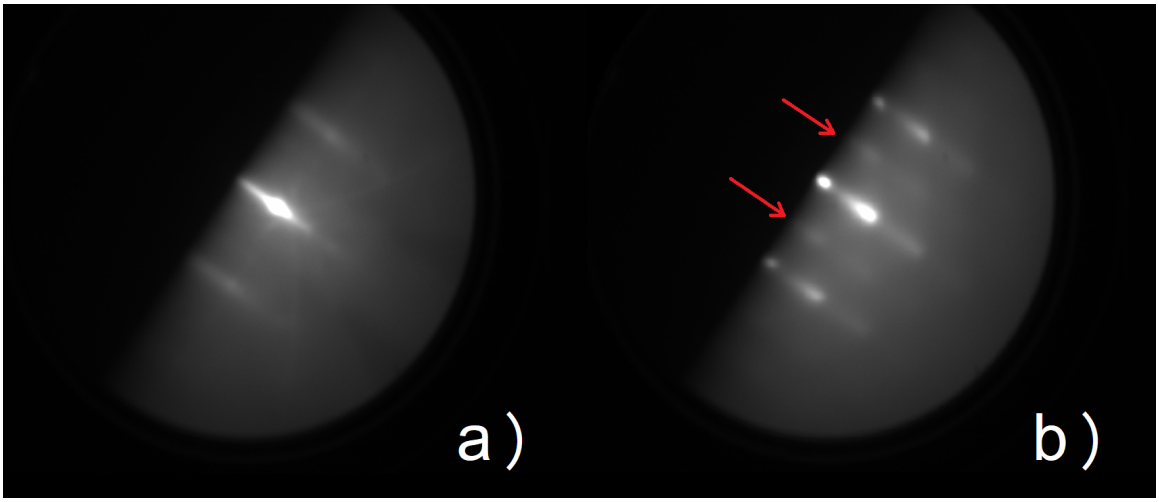

Figure 4.9: Shown are two RHEED images of ZSN films. a) This RHEED pattern clearly shows the three pertinent Bragg rods which indicate the wurtzite structure. To the right, b) an orthorhombic pattern is shown, noted by the secondary streaks visible between the three primaries. These are pointed out by the red arrows and are indicative a doubling of the unit cell. (See Figure 2.1 earlier in the thesis which shows the doubling.)

cation sublattice in an ordered fashion, which doubles the lattice spacing along the orthorhombic a-axis (see Figure 4.8). In Figure 4.9b the red arrows mark the locations of the half-order streaks that are expected to appear in orthorhombic samples. These secondary diffraction peaks manifest due to a doubling of the unit cell spacing along the a-axis in real-space; since the RHEED depicts the reciprocal space of the structure, the distance between streaks is, as a result, halved.

Using a combination of the ImageJ software and the kSA 400 analysis package, a linescan can be taken across the RHEED image and the pixel brightness across said line could be plotted with the binned pixel location to produce a graphical representation of the RHEED intensity (see Figure 4.10). This was useful for determining the crystallinity of the films, as half-order peaks will manifest for orthorhombic films (see Figure 4.11), and also for estimating growth rates, in terms of the number of layers present. The latter could be achieved by plotting the pixel brightness from a series of RHEED images with time over the course of roughly 30 seconds of growth.

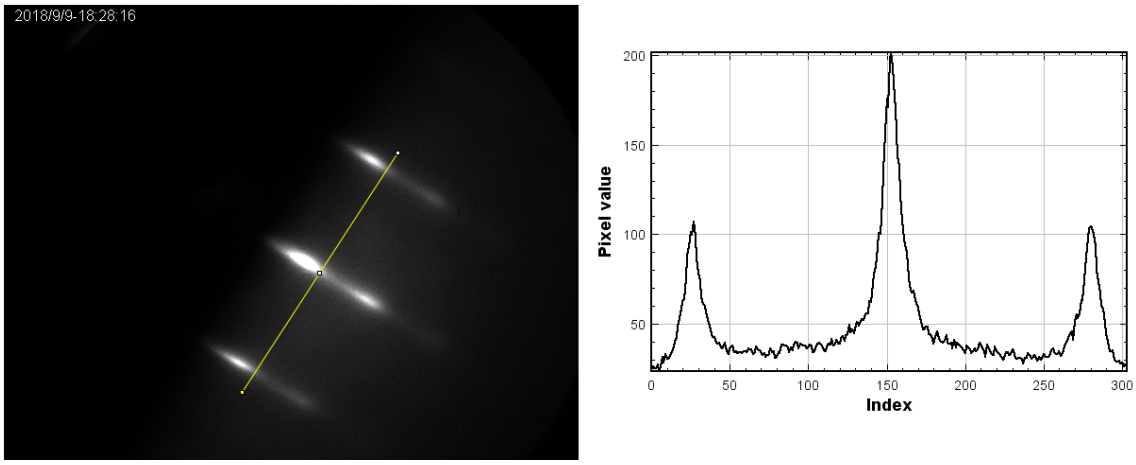

Figure 4.10: A linescan across the RHEED image (left) of sample WPI146 and the corresponding plot of pixel brightness intensity (right).

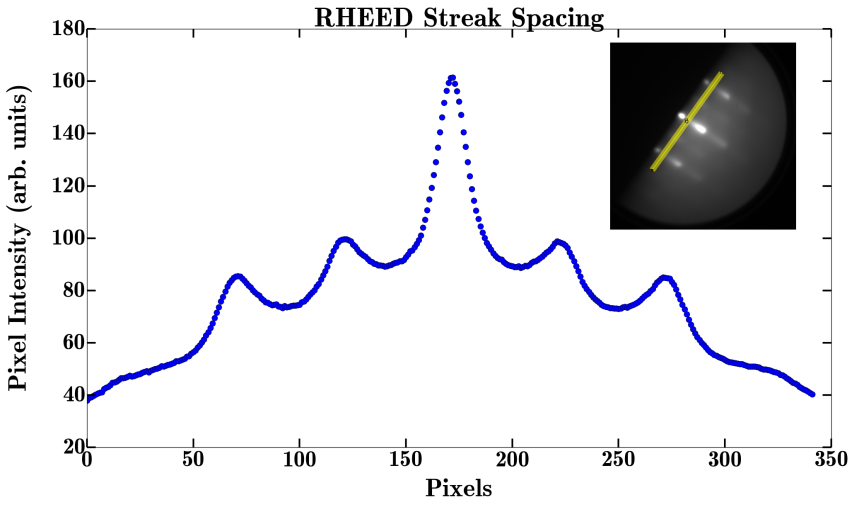

Figure 4.11: A linescan across the RHEED image (inset) of an orthorhombic film and the corresponding plot of pixel intensity (main)[13]. The half-order streaks can be clearly seen at 125 and 225 pixel positions (horizontal axis).

As the atomic layers complete, the brightness of the diffraction pattern maximizes before again approaching some minimum intensity. These oscillations occur for every layer but are most clearly seen near the start of growth, hence the bulk of the images are captured within the first 10-15 minutes of growth.

Since all samples were monitored *in situ* with RHEED, later experiments like XRD could be used to confirm RHEED findings and to provide a more complete analysis and understanding of the nature of ZSN thin films.

4.1.3 XRD Setup

Beam lines 13-BM-C, 33-ID-D and 33-BM-C were used to conduct XRD experiments at the APS. XRD experiments were performed with synchrotron radiation at the Advanced Photon Source on several films, and respective unit-cell refinement measurements were made "by fitting over twenty film reflections using Bragg peak positions obtained from Kappa diffractometer angle calculations"[12]. For each experiment, a 15 keV beam of monochromatic X-rays was used, which was optimized to be 270 μm x 30 μm in the horizontal and vertical directions, respectively, to probe the structure of the films and to confirm the structural findings from RHEED, particularly the doubling of the unit cell associated with the orthorhombic phase.

4.1.4 XRD Results & Discussion

Since ZSN has 3-fold symmetry, the high-order Bragg peaks from the film were used as waypoints to map the 3-dimensional reciprocal space (3D RSM's) of the crystal. This was achieved by using a PILATUS 100K area detector to measure the intensity distribution around said peaks by scanning along the L-direction to create a series of 2-D reciprocal space slices. These slices were then stacked vertically to render the 3D RSM's of which Figures 4.12 and 4.13 are 2D projections.

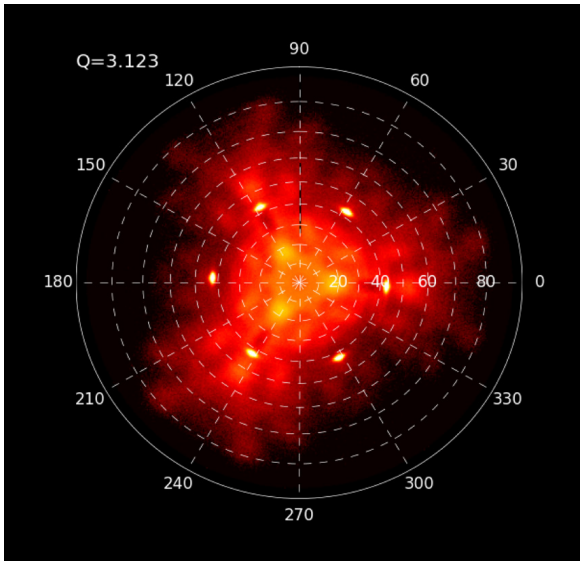

Figure 4.12: Pole figure of the (102), (112), (012) peaks of a wurtzite film[12].

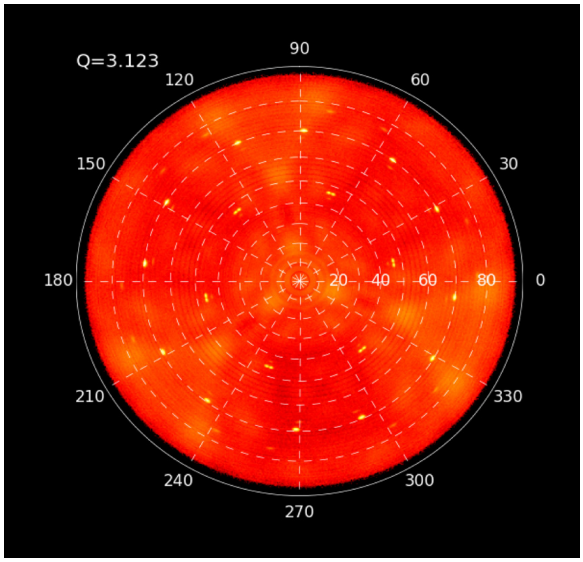

Figure 4.13: Pole figure of the (102), (112), (012) peaks of an orthorhombic film[12].

4.2 Spectroscopy Experiments

4.2.1 DRS Setup

Diffuse reflectance spectroscopy allows the indirect probing of a material's absorptive properties by measuring its reflectivity. For part of this experiment, broadband light was sourced from a Quartz Tungsten Halogen QTH lamp through fiber optics and focused down to a collimated beam (1 millimeter in spot size via a microscope lens in WDRS mode only) and fed through low-OH optic fibers into a beam collimator. Diffuse reflection (off-specular angle) of the sample was then detected using a capture lens coupled to an IR-range BandiT spectrometer equipped with an InGaAs sensor via another optic fiber, as depicted in Figure 4.14. With this detection setup, measurements could be made within the wavelength range 875-1400 nm, however due to the small size of the samples and beam divergence, this setup was very difficult to align.

Initial objectives for this step were two-fold: 1) quickly determine whether or not a higher wavelength range was needed, and 2) detect with some level of certainty any features that that exist toward the longer wavelength range of the visible spectrum. This allowed the need for multiple spectrometers to be minimized, using only one set of optics (low-OH optic fibers, a gold-coated interior of the light source and the InGaAs spectrometer sensor). To go higher in energy (lower in wavelength), it is necessary to swap these components out for others that were more conducive to transmitting visible light (low-OH fibers, some other coating for the source bulb, and a silicon sensor in the spectrometer). Measurements performed in the visible range were made using a similar band-edge spectrometer, but which employs a silicon sensor and a cooler fitted with a thermo-couple temperature sensor instead of the InGaAs sensor. This particular spectrometer's lamp source controller runs hotter due to the higher energies used, thus it needs a cooler to stabilize its temperature and

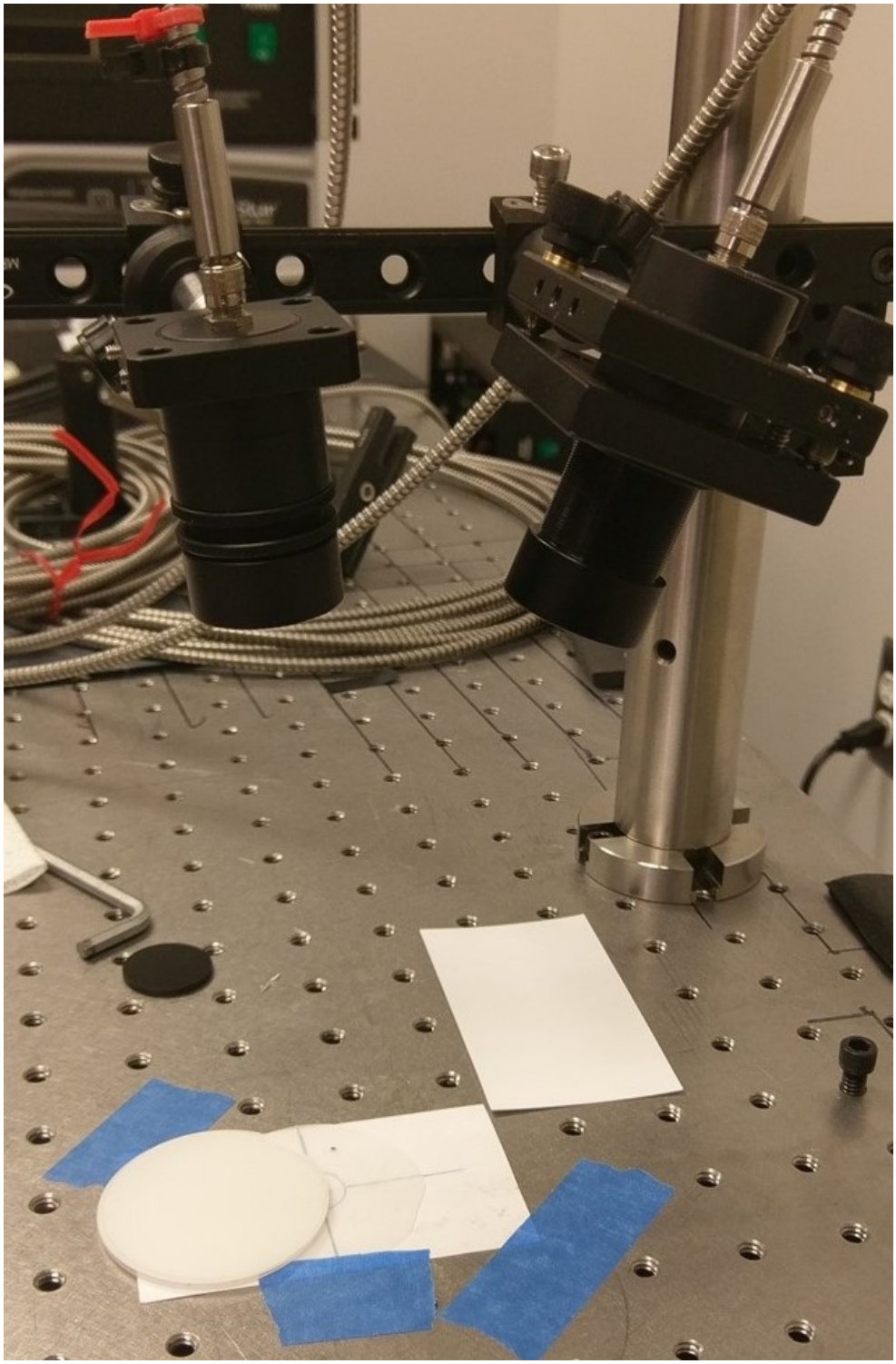

Figure 4.14: A traditional diffuse reflectance setup. All DRS/WDRS measurements were made with equipment provided by k-Space Associates.

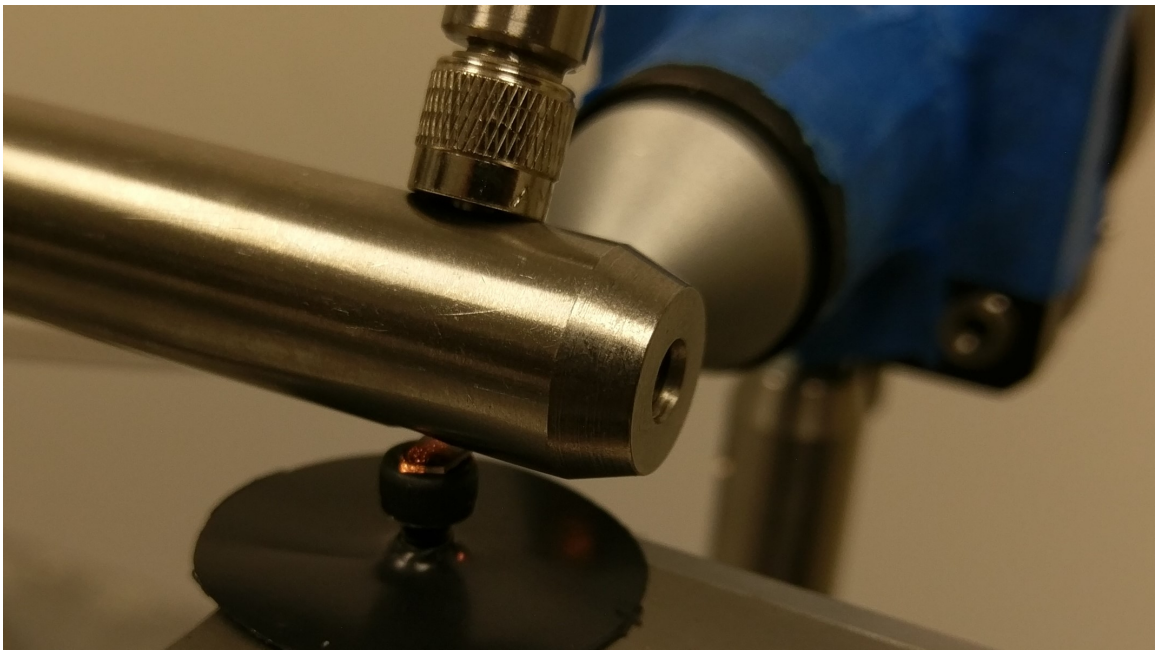

Figure 4.15: A modified version of the diffuse reflectance setup, instead utilizing the fiilm as a waveguide. The beam from the source is visible crossing the surface of the sample. All DRS/WDRS measurements were made with equipment provided by k-Space Associates.

the temperature of the nearby sensor. A lack of proper cooling for this sensor would result in significantly higher noise levels due to thermal excitations within the device.

4.2.2 DRS Results & Discussion

In the interest of achieving measurements with low noise, there are a few important steps to take when using the grazing incidence method described above. Firstly, it is important that the measurements are taken in as dark an environment as possible. This will reduce noise levels due to other sources of radiation entering the fiber, which is directly coupled to the spectrometer such as, but not limited to: ceiling lights, the monitor light from the computer used to take the measurement, and also sunlight. If not properly suppressed, these sources may add unwanted curvatures and noise to the spectrum. This is particularly important because of the integration time needed to acquire the signal. The integration time is cognate to the shutter speed of a DSLR

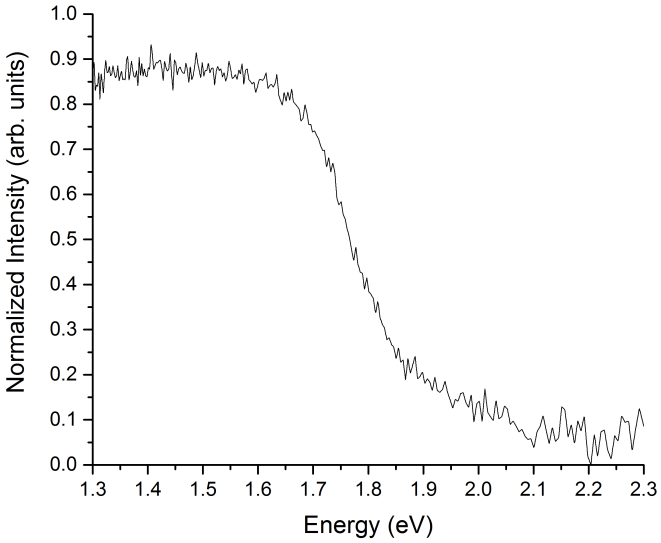

Figure 4.16: Reflectance intensity shown for the annealed wurtzite film P69D.

camera. For a camera, the longer the shutter is open, the more light is allowed to reach the sensor and create the image. In spectroscopy, the longer the integration time, the more light is allowed to reach the sensor and be used to create the spectrum for that given time frame. For example, with an integration time of 500 milliseconds, 500 milliseconds worth of light data will be aggregated by the sensor and used to create the corresponding spectrum. There are benefits and caveats to utilizing a long integration time, however. With longer integration times, less measurements are able to be performed within a given time period, but the benefit is that the signal to noise ratio can usually be increased by at least a factor of two.

Although most preliminary reflectance measurements using the traditional setup proved to be largely uninsightful, due to low signal and high noise issues. The only exception to this was a single sample pulled from previous work. As a part of an investigation into whether or not the orthorhombic structure could be achieved post-growth on a wurtzite structure, the film had been annealed.This sample had been grown on an $LiGa_2O_3$ (LGO) substrate, as opposed to the YSZ used mostly for this

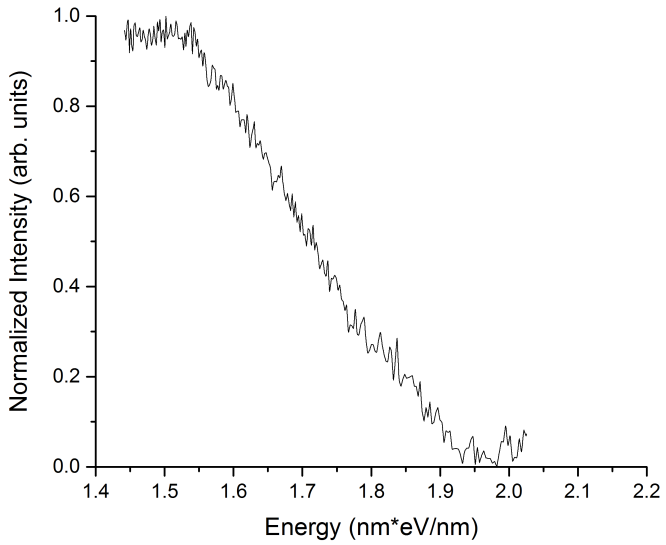

Figure 4.17: Reflectance intensity shown for an orthorhombic film WPI88C. Measurements performed using our new waveguided diffuse reflectance technique. Note the very clean absorption edge detemination.

project, but like the rest of the samples, it was grown via plasma-assisted MBE using the same system. *In-situ* RHEED measurements and *ex-situ* XRD measurements confirmed the wurtzite structure in the film. After it was annealed, however, further investigation found that the sample's crystal structure had been altered from wurtzite to orthorhombic. Optical probing of this sample using traditional DRS methodology indeed showed an absorption edge similar to that which would be expected from an orthorhombic film. A linear extrapolation to the x-axis from the point of inflection, shown in Figure 4.16 suggests a band gap of approximately 1.85 eV +/- 0.01 eV, which is consistent with theoretical values previously suggested[18, 23]. This was the first ever measurement on an orthorhombic sample that had been produced by annealing a sample originally grown in the wurtzite phase.

Waveguided diffuse reflectance measurements of orthorhombic samples, see Figure 4.17, suggest and band gap of roughly 1.95 eV, while wurtzite sample measurements suggest a band gap closer to 1.2 eV, as shown in Figure 4.18. These values

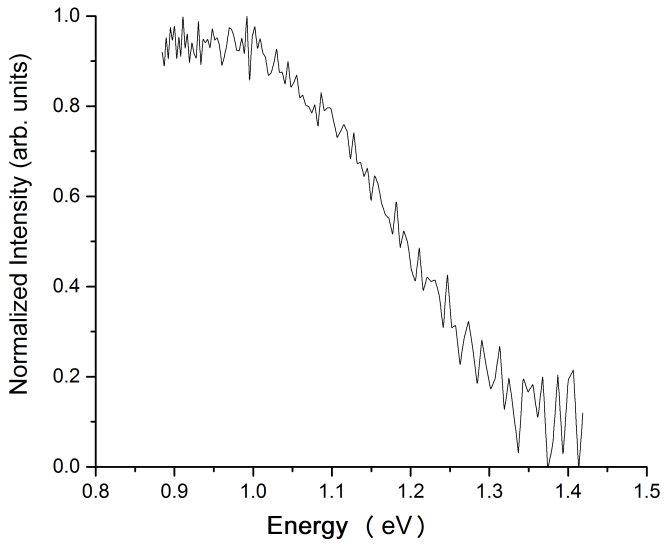

Figure 4.18: Reflectance intensity shown for a wurtzite film WPI91A.

are consistent with theoretical data band gap predictions put forth by Feldberg[18] and Punya[23] in 2013, and with experimental evidence found by Quayle et al. [42] in 2015, although the samples measured in that study were polycrystalline. The band gaps were estimated by taking a linear extrapolation from the point of inflection[24]. A side-by-side comparison of the two samples reveals a blueshift of the orthorhombic band edge by roughly 0.5 eV as compared to the wurtzite band edge, as seen in Figure 4.19.

Accurate quantification of the increase in signal-to-noise ratio achievable by using WDRS over a traditional DRS setup has proven difficult to obtain. This proceeds from a number inconsistencies that are currently inherent to the measurement procedure on the part of the sample as well as on the part of the setup. Here are outlined a few aspects of the experiment that have proven *extremely* difficult to replicate. These variables appear to contribute significantly to the overall S/N ratio. Fine control of at least a few of these variables *must* be prioritized in the future to explore the true capabilities of this novel "Waveguide DRS" method. With regards to the

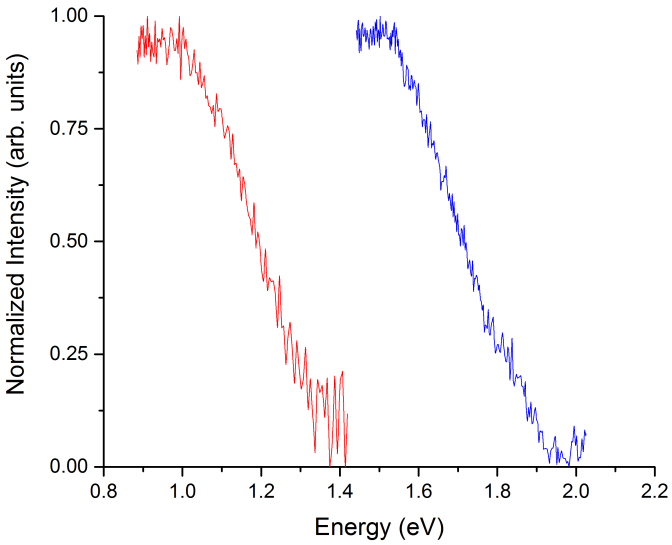

Figure 4.19: Waveguided diffuse reflectance intensity shown for wurtzite (red curve) and orthorhombic (blue curve) films WPI91A and WPI88C, respectively.

sample, the exact positioning varies according to size and shape. Samples were on average 5x5mm^2, which was sufficiently small for the most recently realized setup to maintain consistency; however, this size generally makes the handling and adjustment of the sample positioning more difficult. With regards to the setup, a lack of needed components severely restricted variability of the angle of incidence. To complicate matters, the angle of the cleavage along the sample edge dramatically affects the amount of light able to enter the substrate and exit through the surface. Additionally, the optimal angle of diffuse reflectance capture largely varies from film to film.This is a direct result of the changing angle of incidence needed, based on the substrate cleavage and film thickness.

The overall conclusion is that despite the inconsistencies of the measurement, improvements to the S/N ratio can be seen by using this WDRS method over the traditional DRS method. This experiment serves as a proof-of-principle investigation of this method.

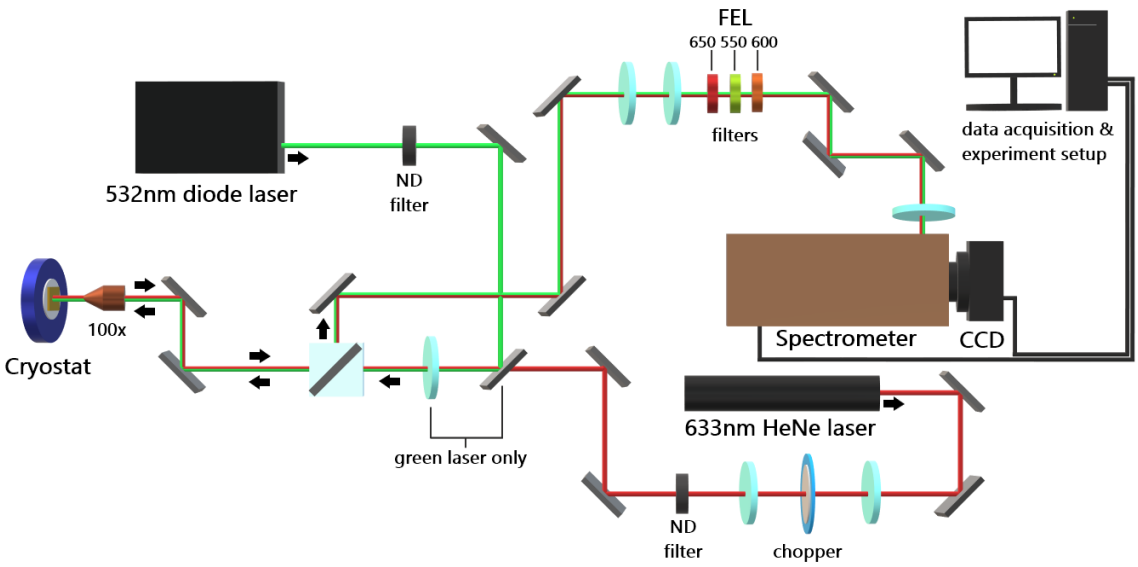

Figure 4.20: Setup used for all PL experiments, schematically depicting all optical components. This facility is located in Professor Vanessa Sih's Lab.

4.2.3 PL Setup

For the focus of this project two light sources were used, a 633 nm (red) continuous wave (CW) HeNe laser and a 532 nm (green) diode laser, which were situated at normal-incidence to ensure consistent photon flux exposure between samples. The samples studied in this experiment were ZSN thin films of typical thicknesses (∼100 nm) grown on a square centimeter (111) YSZ substrate (which was subsequently divided into 4 smaller samples). The detector was a liquid nitrogen-cooled charged-coupled device (CCD) array spectrometer (Supplier: CVI). During experiments using the 532 nm laser, a 550 nm and a 600 nm longpass filter were used to attenuate the signal from the laser. Experiments conducted with the 633 nm laser, however, utilized a 650 nm longpass filter so as to minimize signal input directly from the laser. The initial experiment was conducted between 10 K and 30 K, but most subsequent experiments were conducted below 10 K to minimize the likelihood of thermal noise.

To employ this technique, samples were mounted onto a coldfinger inside of an evacuated cryostat fitted with a glass window (roughly 2.5-3 inches in diameter).

Pressures as low as 10^{-7} Torr were used to seal the cryostat while preventing the sample environment from building up condensation at extremely low temperatures. Appropriate optics and filters were implemented along the beam path which ends at a variable-grating spectrometer, with an 80nm blazing, that is coupled to a liquid-nitrogen cooled CCD camera (Figure 4.20). An external computer can be used for both data acquisition and to change some of the properties of the experiment such as the grating number and exposure time. All experiments were conducted in a dark room and external light was suppressed as much as possible to prevent unwanted signals. Once the optics and software-driven settings of the experiment have been set up, PL measurements are generally simple to make–the difficulty lies in accurately interpreting the data.

4.2.4 Photoluminescence Studies

This section presents the first attempts to obtain PL data on MBE-grown samples of ZSN. We met several challenges, not all of which are fully resolved, but we were able to obtain some interesting results which are useful to compare with other optical techniques presented in this Chapter. The measurements were performed in the laboratory of Prof. Vanessa Sih. Facilities were available for variable temperature cryogenic measurements down to T = 10K. This was important to overcome the effects of thermal excitation, which as we shall see can significantly degrade the photoluminescence spectrum. Several different types of light source were available for PL, including a He-Ne laser (633 nm; 1.96 eV), a green diode laser (532 nm; 2.33 eV), and a blue diode laser giving 350 nm, or 3.54 eV. It is important to choose a light source with sufficient photon energy to enable valence to conduction band transitions in order to detect the radiative recombination of electrons and holes which will provide information about the optical band gap.

The range of band gaps of interest for ZSN spans roughly 1-2 eV, depending on the

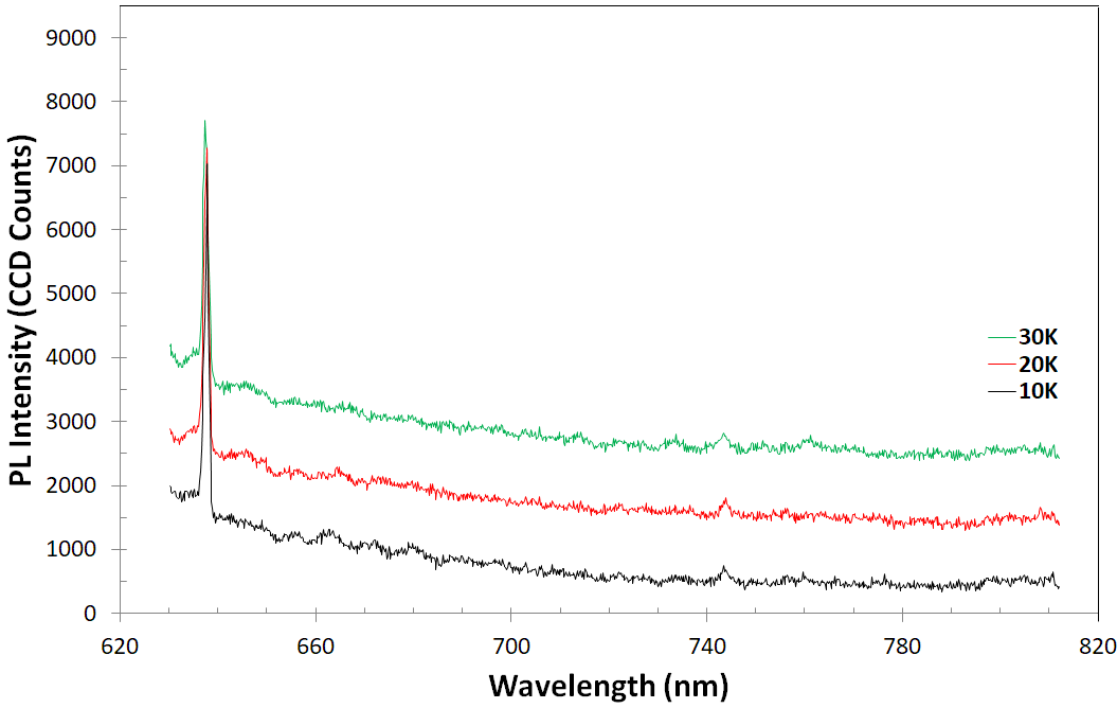

Figure 4.21: PL spectrum of orthorhombic thin film of ZSN (sample P61) measured at three different temperatures between 10K and 30K. The sample was grown by MBE on an LGO substrate. The sharp peak at 633 nm is a remnant of the He-Ne laser source. No significant optical emission from the sample was observed at this excitation wavelength.

degree of cation ordering, therefore He-Ne is marginal for the samples at the upper end of this range. This is illustrated in Figure 4.21 which shows the PL spectrum of sample P61F, a ∼100 nm thick ZSN film grown in the orthorhombic phase. As the excitation source, the He-Ne laser was very close to the expected band gap energy of orthorhombic ZSN, so we switched to a shorter wavelength, 350 nm (3.54 eV). Figure 4.22 shows the PL spectrum for the same orthorhombic sample (P61) measured at T= 10K with the more energetic photons of the 350 nm excitation source. We observe a broad peak at approximately 660 nm (1.87 eV), towards the limit of the spectral range of this spectrometer. This is consistent with the expected optical band gap of the orthorhombic (cation ordered) samples of ZSN, as determined by band-edge absorption measurements presented in Section 4.2.2, and later confirmed by cathodo-

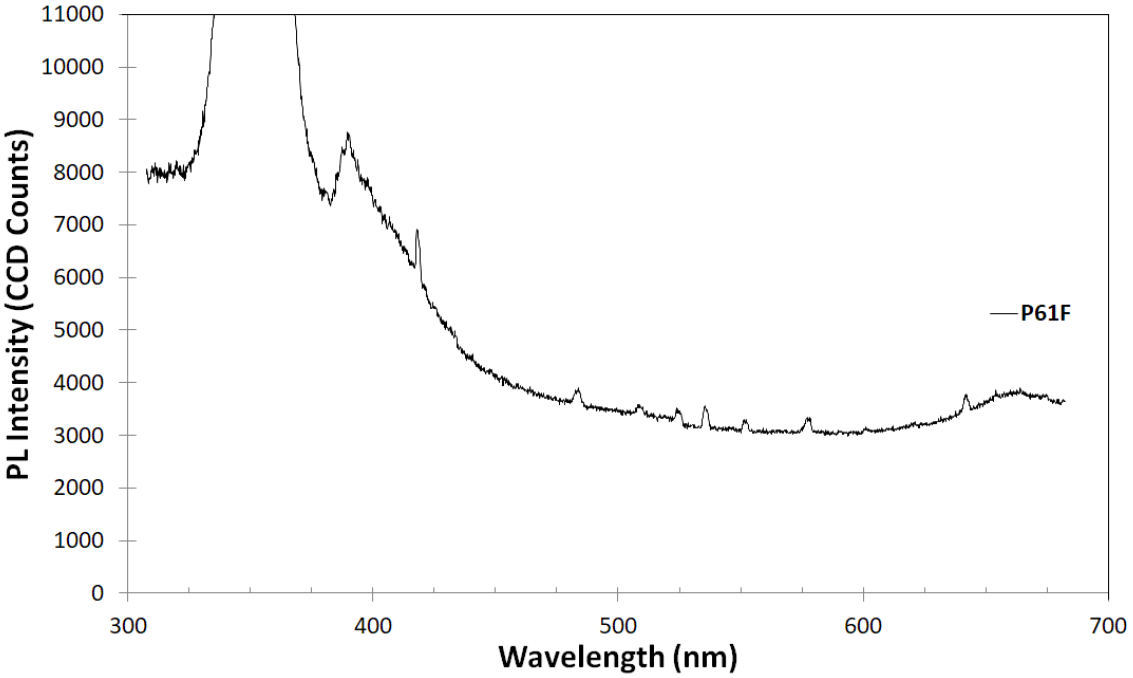

Figure 4.22: PL spectrum measured at T= 10K, for sample P61, the same sample as for the data shown in Figure 4.21, except using a 350 nm excitation source. In addition to the PL peak of interest at ∼660 nm, there are a number of sharp, but low intensity, lines associated with the excitation source.

luminescence (CL) techniques reported later in this Chapter (see Section 4.4.2).

4.2.4.1 PL Studies of quantum well structures

We turn now to the interesting possibility of observing optical emission from a quantum well structure constructed entirely of $ZnSnN_2$, with barrier layers formed from the orthorhombic phase ($E_g \sim 2$ eV) and the well layer composed of the wurtzite phase ($E_g \sim 1$ eV). We were encouraged to try to fabricate such a sample by the high quality of the film-substrate interfaces made possible by MBE growth. An example demonstrating the atomic abruptness of the epitaxy of ZSN on YSZ substrates is shown in the high-resolution TEM micrograph Figure 4.23 kindly obtained by Dr. Kai Sun in the Michigan Center for Materials Characterization (MC^2).

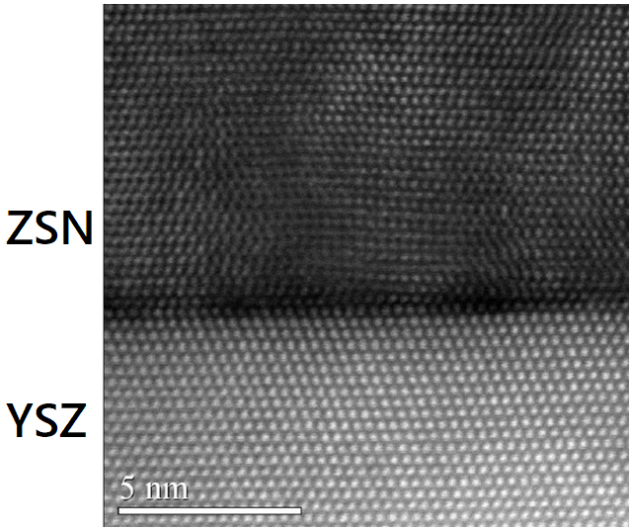

Figure 4.23: High-resolution Transmission Electron Micrograph of atomically sharp interface between the YSZ substrate and ZSN film. Image obtained by Dr. Kai Sun, University of Michigan (MC^2).

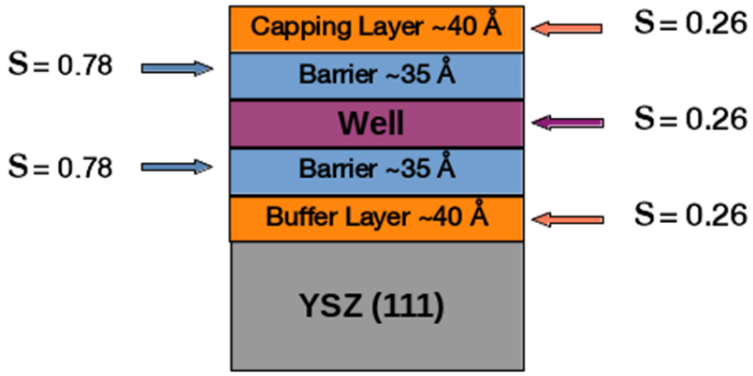

Figure 4.24: Schematic of an order-disorder quantum well, with barrier and well layers composed entirely of $ZnSnN_2$. The QW samples are grown by MBE on a YSZ (111) substrate, with 40 Å ZSN buffer and capping layers predominantly in the wurzite phase and 35 Å-thick orthorhombic ZSN barrier layers. The degree of cation ordering for each layer is indicated by an order parameter, S, determined by RHEED.

The possibility to fabricate a quantum well in this way is an interesting development and while a slightly different approach has been explored for $GaInP_2$ by Mukherjee et al. [43], who instead focused on non-isocompositional heterostructures,

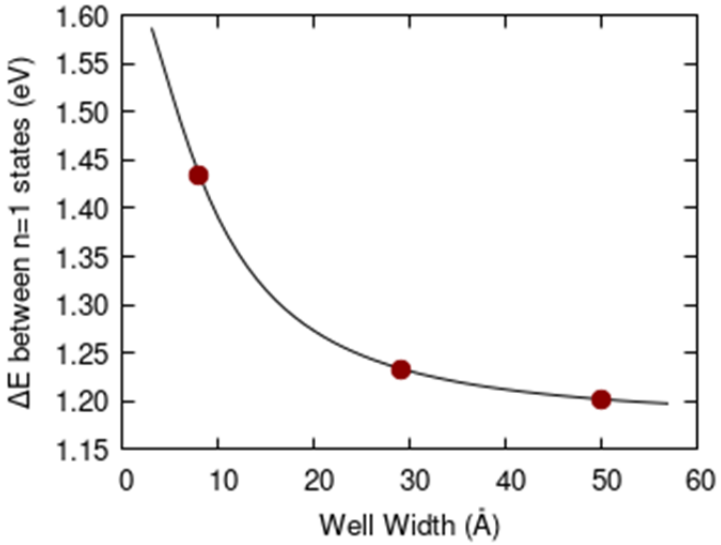

Figure 4.25: n=1 to ground state transition energies for confined QW states predicted by a particle-in-a-box model for the different well-widths of our samples. The target widths for our samples are shown as red dots.

we explored the fabrication of quantum wells formed by a modulation of the ordering of the cations in all layers of otherwise identical chemical composition. A schematic of the structure is shown in Figure 4.24. We mounted three different QW samples on the cold finger of an optical cryostat and performed PL spectroscopy on them using a green (532 nm) laser diode source for optical excitation. The three samples had different well widths as follows: sample WPI 144, 30Å; WPI 145, 8Å; and WPI 146, 50Å. Using a particle-in-a-box model, as described in Section 3.2.4, we expect to see PL at the energies shown in Figure 4.25, as a function of well width.

The optical emission spectrum obtained from all three QW samples is shown in Figure 4.26 (plotted as a function of wavelength) and in Figure 4.27 (the same data plotted as a function of energy). A green (532 nm) diode laser excitation source was employed for these measurements. We note from these data that the positions of the emission lines fall in a range (1.3 -1.4 eV), close to what is predicted for the particle-in-a-box simulation shown in Figure 4.25. However, the spectrum is more complex than what one would expect for a QW with a single well. We believe this could be because

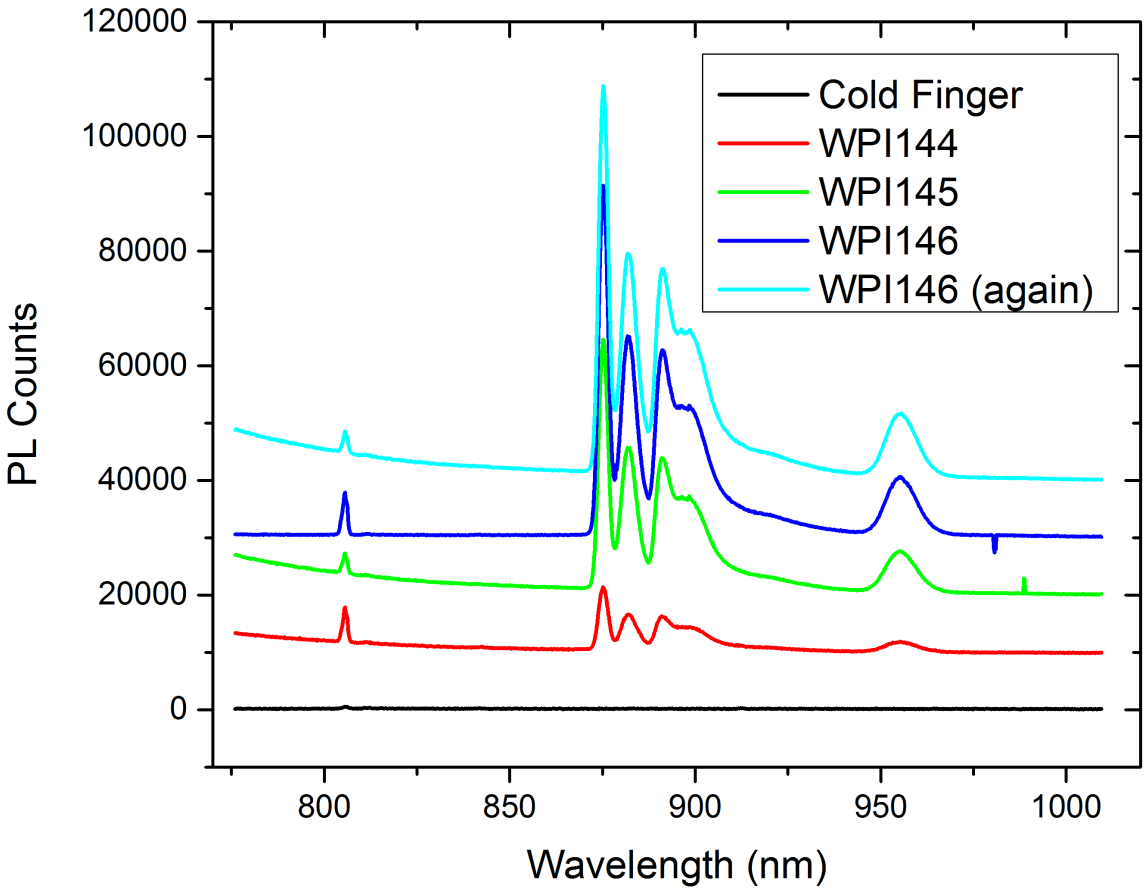

Figure 4.26: PL spectra of the three ZSN quantum well samples in the IR range, 775 nm to 1000 nm, measured at 10K. All three have identical barrier layers 40 Å thick of orthorhombic ZSN (band-gap $\sim$ 2 eV) and a quantum well layer made of wurtzite ZSN (band gap $\sim$ 1 eV). WPI 144 has a well width of 30Å, WPI 145 8Å and WPI 146 50Å. The group of peaks between 875 nm and 975 nm are supposedly from transitions between quantum well states. The sharp peak at 805 nm is from unknown origin, having been confirmed to exist in data taken by others in the Sih Group.

the additional buffer and capping layers also act as confining wells for the electron eigenstates; they have similar widths ($\sim$40 Å) and therefore may dominate the PL spectrum. This might be the reason why the emission wavelengths are so similar for the different samples, even though the nominal well widths are different. Also, the precision to which layer thicknesses can be controlled is uncertain at the present time.

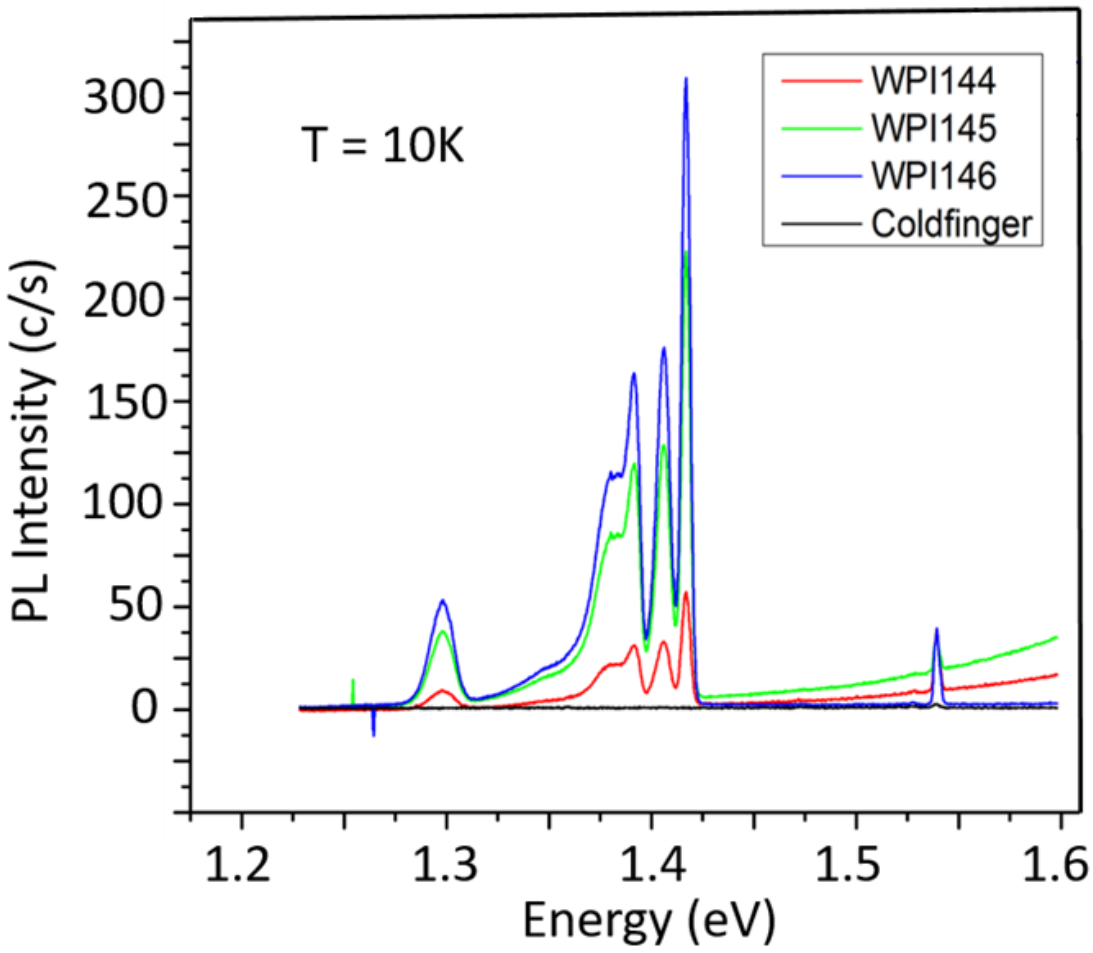

Figure 4.27: PL spectra as in Figure 4.26, plotted as a function of energy, for the three QW samples. The laser excitation wavelength was 532 nm (2.33 eV). The peak at $\sim$ 1.55 eV is an artifact of unknown origin, having been confirmed to exist in separate data taken by others in the Sih Group.

We should also caution that these are the first measurements of their kind on the first three samples we have grown. While the PL measurements on these prototype QW structures are very promising, it will be necessary to grow additional samples, perhaps with a simpler layer structure, and perform more systematic measurements on them to verify that indeed the observed emission is originating from confined QW states.

We also explored whether the PL spectrum had the expected reduction in intensity and peak broadening that is expected as a function of temperature. Figure 4.28

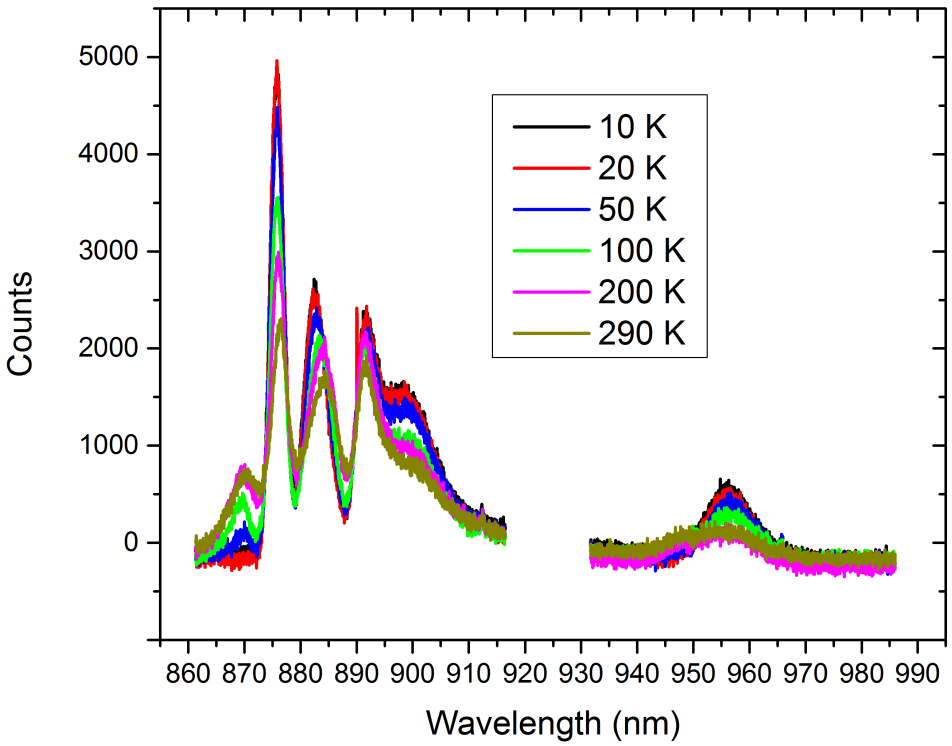

Figure 4.28: PL spectra of one sample (WPI 146). Temperature was varied between T = 10K and 290K (approximately room temp.). The 600 G/nm setting was used to view a more narrow range with higher resolution.

illustrates that the spectrum does indeed improve significantly in quality between T = 290K and 10K.

4.3 Electrical Experiments

4.3.1 Hall Effect Setup

To prepare the samples for electrical measurements, four indium-tin (50-50 by % wt.) contacts, separated by ∼5 mm, were soldered onto the sample in the van der Pauw configuration, as shown in Figure 4.29, using a fine-tipped soldering iron to minimize the size of the contact[45]. Samples were then mounted onto a blank,

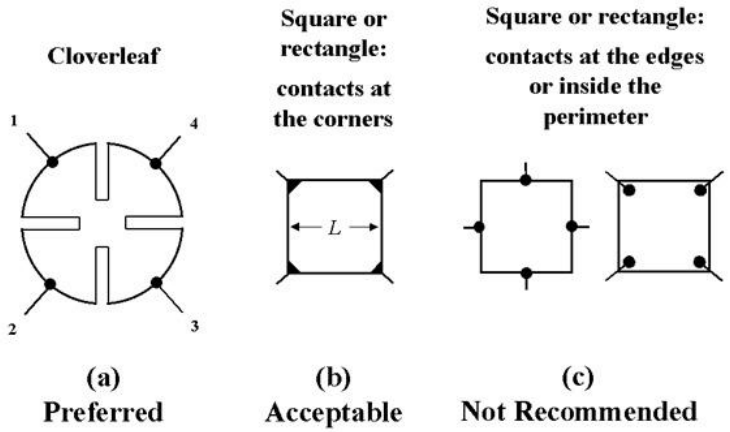

Figure 4.29: The placement of the contacts shown in b)was primarily in this experiment and is a generally accepted configuration for producing reliable Hall measurements on shapes which are less suitable for measurements using a traditional Hall bridge or the preferred "cloverleaf"configuration depicted in a). In a few cases, contact placement closer to that depicted in c) was used for reasons explained[44].

16-pin circuit board connector with vacuum grease to ensure that it would not fall or move during the experiment. Contacts were alloyed in forming gas at 350^{o}C for 60 seconds, and afterward, thin copper leads were applied to the sample by first soldering the leads to the contacts, then extending those leads out to the four corner connector pins (e.g. 1,8,9, & 16). A picture of a typical sample mount can be seen in Figure 4.30.

The Hall measurement setup (shown in Figure 4.31) was prepared by the Goldman Group in their lab on North Campus and consisted of two permanent magnets, a vertically-oriented sample holder, a Keithley current source, and a Hewlett-Packard voltmeter. The magnetic field itself, which was measured to be 1200 Gauss (0.12 T) using a Lakeshore 410 Gaussmeter and Transverse Probe, provided a uniform magnetic field at the center point between the two plates and penetrated normally to the surface of the film. The orientation of the magnetic field was reversible providing 180^o rotations so that either a negative or a positive field could be applied to the

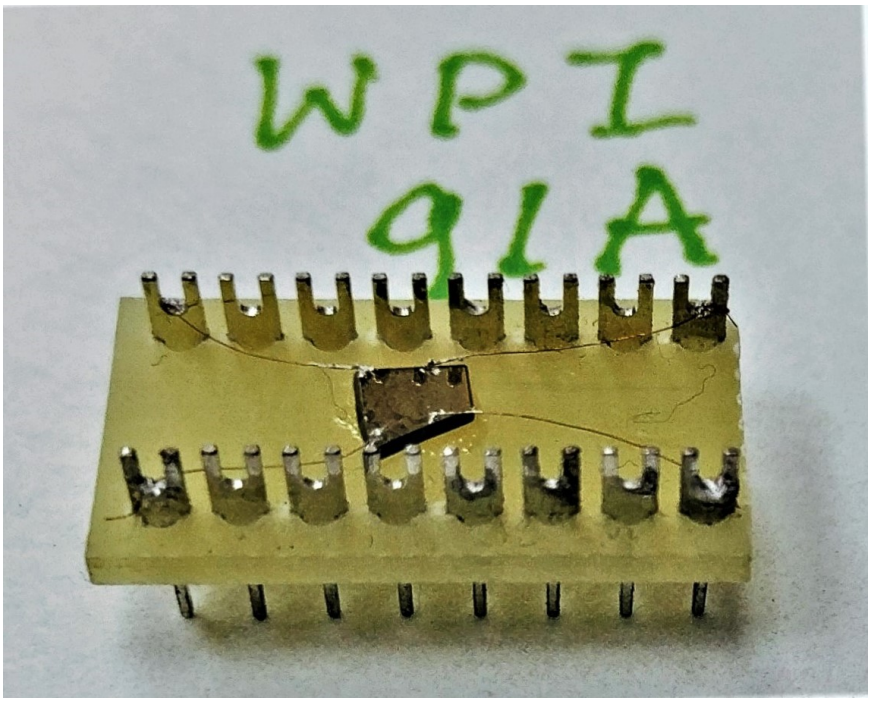

Figure 4.30: A picture of one of the samples mounted onto a 16-pin connector. Copper leads can be seen extending to the four corner pins.

sample. Resistivity measurements were made first in the absence of a magnetic field by sliding the magnets along the rails away from the sample holder (see Figure 4.31) .

An electric field was produced between two contacts by the Keithley current source, while the voltage was measured across the other two contact points using a Hewlett-Packard voltmeter. The electric field polarity and direction were alterable by utilizing a combination of the source and the "control box" (shown above the voltmeter in Figure 4.32) which was equipped with banana connectors that were wired to each of the four corner pins on the sample holder. All measurements were conducted at room temperature.

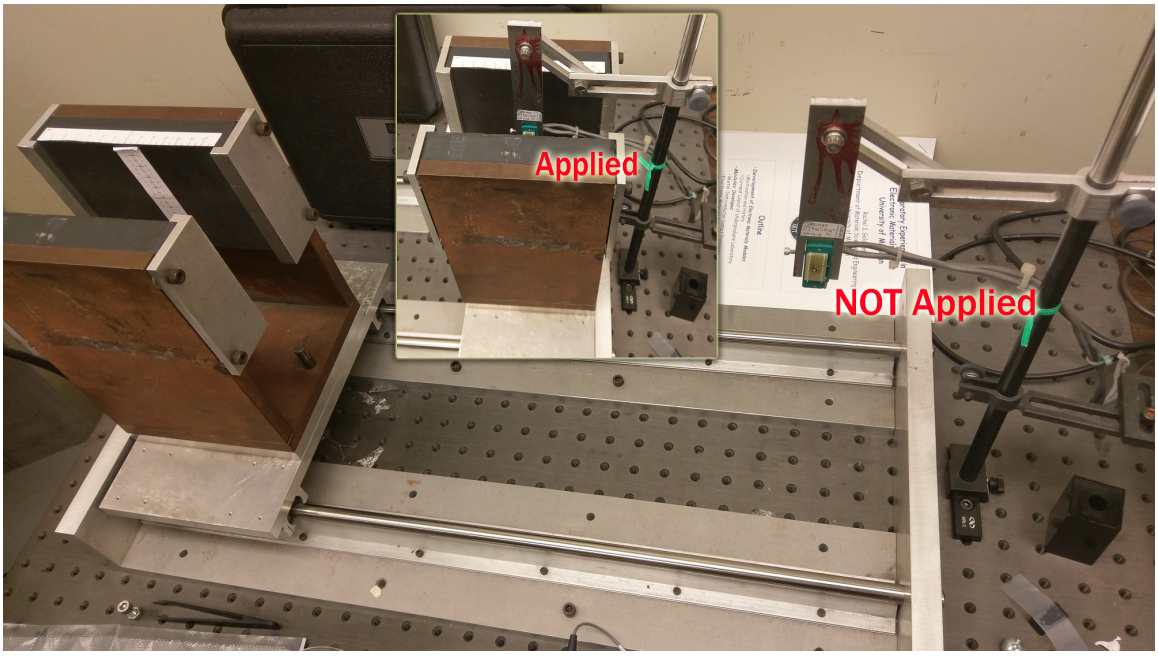

Figure 4.31: Resistivity measurements were carried out without the presence of a magnetic field (main), while Hall measurements were conducted with the magnetic field applied(inset).

4.3.2 Hall Effect Results & Discussion

Accurate placement of contacts on the corners of a square sample, in accordance with the preferred and accepted configurations(see Figure 4.29), was not always possible due to the inconsistency of the shapes of some of these samples. In some extreme cases the sample had less than four, well-separated corners, in which case contacts were placed closer to the middle of an edge so as to avoid placing two contacts too near to each other. In other cases, samples inherited scratches from the diamond scribe used to break the original die into multiple samples; thus, contacts were placed so that a current could still pass uninhibited by a break in the film. To compensate for these types of irregularities in the sample shapes, the magnetic field was reversed in orientation, in addition to the applied current. This provided parity in the measurement, so that the four slightly different observed voltages could be averaged to obtain the true Hall voltage. While other minor steps were taken to reduce variance

in the measurements (e.g. using the same solder tip, etc.), a significant amount of time was spent monitoring and reducing the amount of noise in the experiment.

Measurements were made by applying a current across one direction and measuring the voltage across the other. During low voltage measurements (in the μV range), thermal fluctuations may significantly impact the readings if the proper current is not chosen. A current of 1.5 mA was used for the majority of the samples, which was sufficient to avoid fluctuations in the voltage readings due to temperature-induced noise. For confirmation, a comparison test of voltage fluctuations was made between two applied currents of 1 mA and 1 μA, the results of which are shown in Figure 4.33.

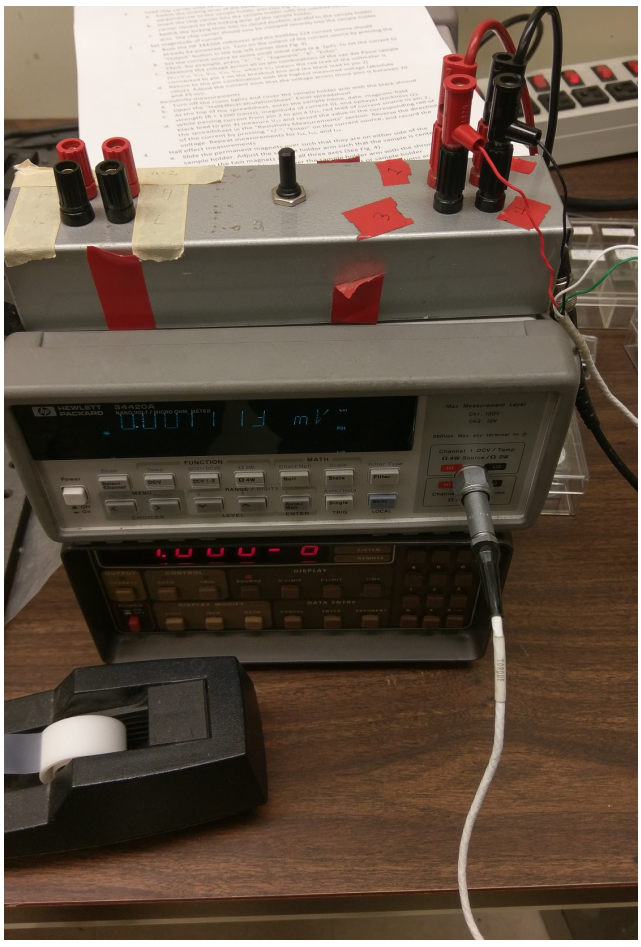

Figure 4.32: Shown are the Keithley current source (at bottom), the Hewlett-Packard voltmeter (middle) and the "control box," (at top) which was used to change the orientation of the current relative to the sample contacts.

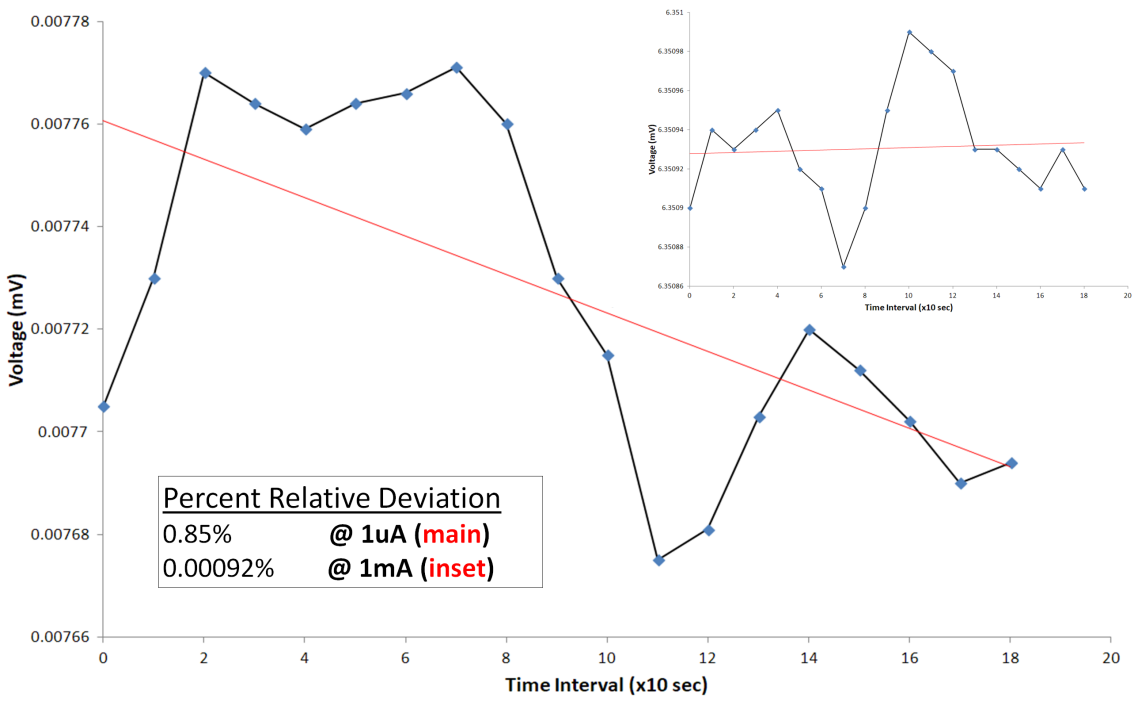

Figure 4.33: Voltages in the main plot were measured with an applied current of 1 μA, while the top-most inset shows voltages achieved with an applied current of 1 mA. The lower inset shows that the percent reduction in noise-level from using a 1 mA current is roughly three orders of magnitude (10^{-3}).

Voltages were measured in 10-second intervals up to 180 seconds. The results show that one can obtain three orders of magnitude in the signal-to-noise ratio by using mA-level currents, as opposed to μA, thus it can be deduced from this test that currents near and above 1 mA are sufficient for noise suppression in voltage readings. For confidence sake, most of the sample measurements were made above 1 mA. All samples were not well suited for electrical measurements. Many of the early samples were too small to reliably put down contacts by hand without risking significant coverage of the film by solder. To that end, choice samples were selected for measurement. Table 4.1 shows the carrier concentrations and mobilities of measured samples , many of which were 85nm in thickness. All measured samples were observed to have high carrier concentrations, with most having on the order of 10^{21} cm^{-3}, while mobilities were measured to be as high as 32.5 cm^2/Vs. It is likely that the high carrier con-

Sample (o/w)	Carrier Concentration (cm^{-3})	Mobility (cm^2/Vs)
WPI90C (w)	$1.12x10^{21}$	10.91
WPI91A (w)	$3.37x10^{20}$	12.70
WPI93B (w)	$8.65x10^{20}$	10.26
WPI94B (w)	$6.30x10^{20}$	11.51
WPI95B (o)	$1.01x10^{21}$	1.27
WPI98D (w)	$1.20x10^{21}$	12.46
WPI99D (w)	$1.36x10^{21}$	10.08
WPI144D (w)	$2.08x10^{21}$	13.45
WPI145D (w)	$2.02x10^{21}$	13.52
WPI146C (w)	$5.31x10^{20}$	32.50

Table 4.1: These are the measured values for the carrier concentration and mobility of several samples. Here "o/w" represents whether RHEED measurements revealed an orthorhombic or wurtzite structure. All measured films were 85 nm in thickness with the exception of 144, 145, & 146 (179 nm, 158 nm, & 200 nm, respectively).

centrations observed here significantly increase the scattering cross-section of carriers due to the Coulmbic forces between the electrons[1]. Though it was not a focus of this work, it can be presumed that mobility enhancements in semiconductors can be achieved by doping the film with impurity ions, as was explored theoretically in 1996 by Kikegawa and Furuya [46].

An important note to highlight in Table 4.1 are the values observed for sample WPI95B, which was the only measured orthorhombic sample. Significantly higher (10x) resistivity was observed for this sample even though measurements were made using a 1 mA current versus the 1.5 mA used for the other thin-film samples. Unfortunately, some physical degradation of this sample was observed through an optical microscope picture (see Figure 4.34). This could explain the order of magnitude increase in resistivity seen between this sample and all the others.

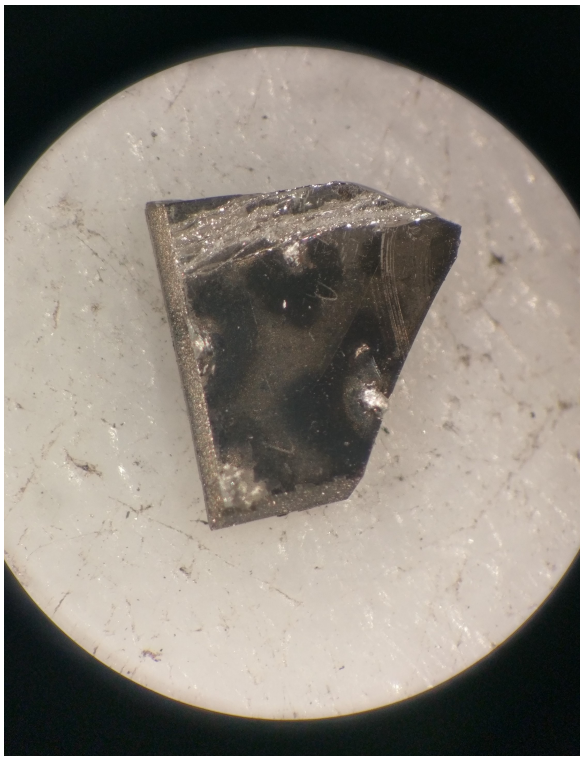

Figure 4.34: (WPI95B) The dark spots surrounding the contacts appeared just after the contacts were alloyed, implying that the temperature used to alloy the contacts was too high for the orthorhombic film, although no wurtzite samples showed any signs of degradation at that same temperature.

4.4 Cathodoluminescence Studies

4.4.1 CL Setup

A schematic of the instrument used for cathodoluminescence studies (located in the Michigan Center for Materials Characterization - $(MC)^2$) is shown in Figure 4.35. The CL spectrometer is integrated with a TESCAN RISE scanning electron microscope and therefore is capable of nanometer-scale resolution. This high spatial resolution capability is therefore very useful for studying the optical emission characteristics of nano-structures such as the thin films and quantum well (QW) structures that are the focus of this dissertation project.

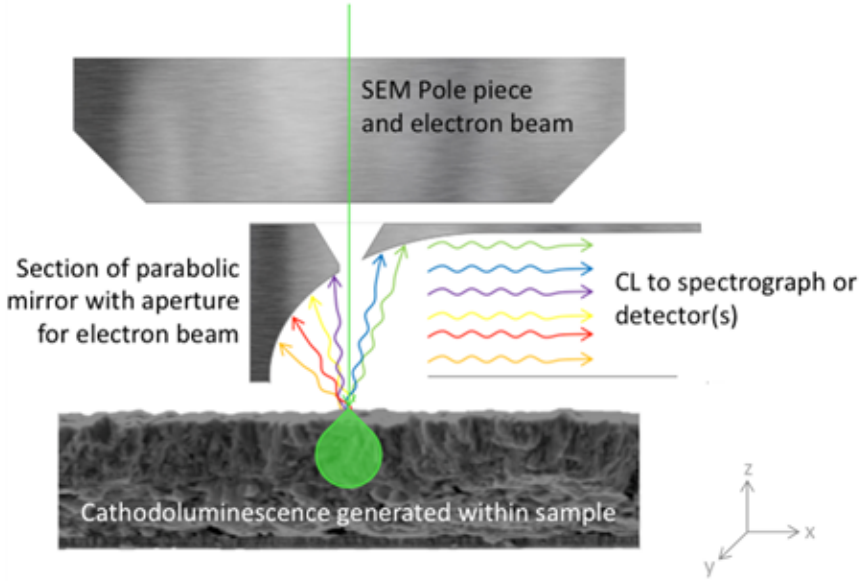

Figure 4.35: Schematic of cathodoluminescence instrument integrated into the TESCAN Scanning Electron Microscope. The green dot representing the focused SEM electron beam is approximately 2 nm in diameter. The light generated by the electron stimulation is collected and analyzed by a Gatan Mono CL4 spectrograph.

With the help of $(MC)^2$ instrument specialist, Dr. Nancy Senabulya Muyanja,

we obtained CL data on three ZSN samples: two single-layer thin films of the orthorhombic (cation ordered) phase (WPI 77 and WPI 79), and one quantum well sample (WPI 146), consisting of a wurtzite confining well (50 Å thickness) sandwiched between two 35 Å thick barrier layers of the orthorhombic phase. We first present the results for the single-layer samples. These spectra, together with the PL data we described in Section 4.2.4, are the first optical emission data ever obtained on the ordered orthorhombic phase of ZSN.

4.4.2 CL Results & Discussion

Figure 4.36 shows the CL optical emission spectrum from WPI 77, a 100 nm thick $ZnSnN_2$ film grown on a (111)-oriented substrate of YSZ. We observed two main features in the CL spectrum Figure 4.36. The most prominent is a broad peak at around 2.75 eV, which can be seen in the CL emission spectrum from the substrate in Figure 4.37. We ascribe this emission to mid-gap deep level states associated with the Yttria-doped zirconia substrate (YSZ), which is somewhat consistent with the known band gap of YSZ being ~5 eV[47, 48]. The other feature, indicated by an arrow, is of more interest for this study as it indicates significant optical emission at 1.96 eV close to the direct band gap of orthorhombic ZSN.

We repeated this measurement on a second sample (WPI 79) whose growth conditions were also targeted at the orthorhombic phase. Figure 4.38 shows the CL spectrum of this sample. Again, we observed the broad, deep-level substrate fluorescence at around 2.8 eV, and also a rather better defined interband emission peak at 2 eV +/- 0.1 eV.

It is clear from these measurements, the first of their kind on the orthorhombic thin films produced (also for the first time) as part of this study, that the optical band gap of fully ordered ZSN is close to 2 eV and this is consistent with the theoretical predictions[18, 20, 24, 26] summarized in Section 1.4 of this thesis as well as supporting

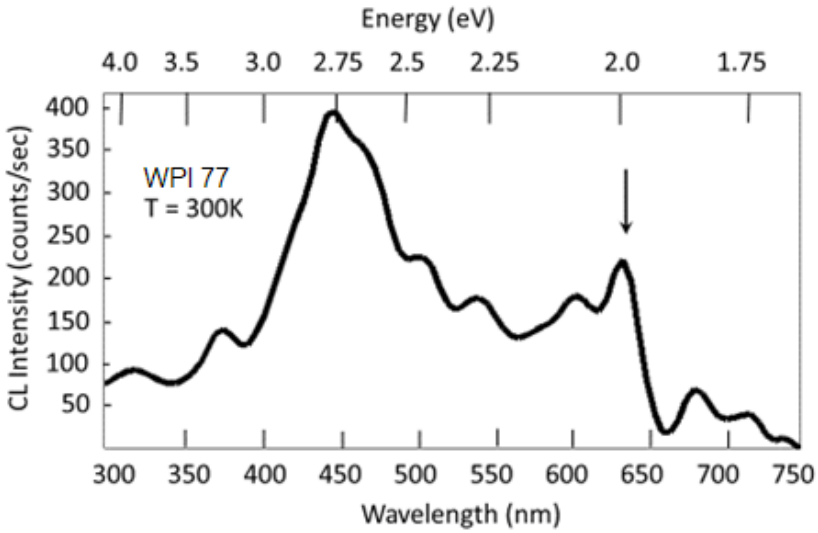

Figure 4.36: CL spectrum of 100 nm thick ZSN sample grown in the orthorhombic phase. We associate the arrowed feature with electron-hole recombination across the direct band gap. The large broad feature around 2.75 eV is most likely substrate-related, as discussed in the text. The small ripples are interference fringes originating in the optical components of the CL spectrograph.

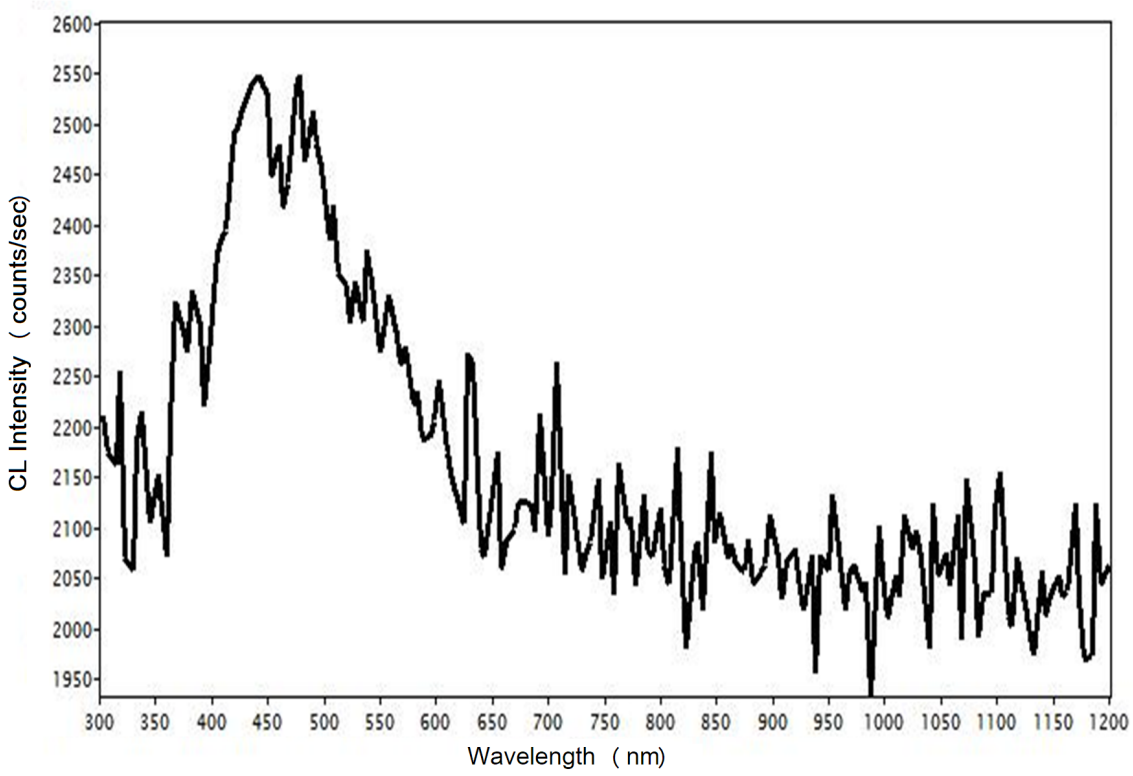

Figure 4.37: Ambient temperature CL spectrum of the (111) YSZ substrate. Despite the noise, a strong emission peak can be seen at 450 nm (2.75 eV).

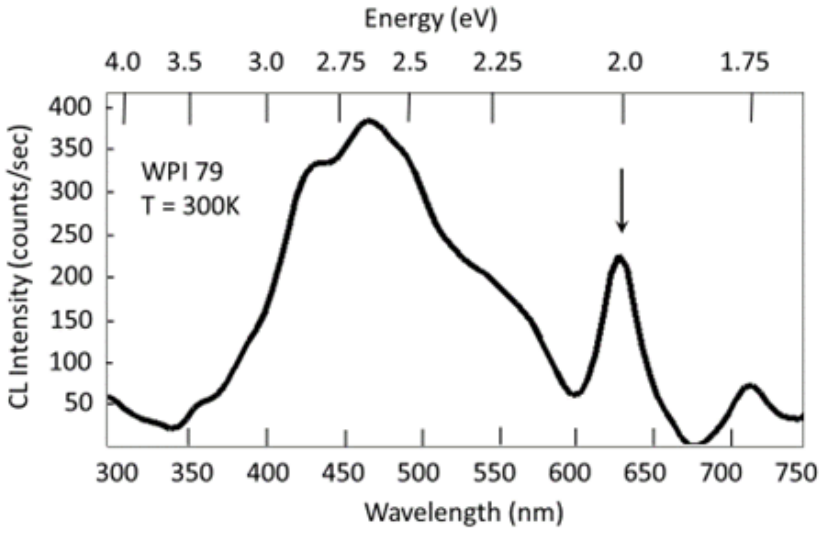

Figure 4.38: Ambient temperature CL spectrum of a second 100 nm thick film of MBE grown orthorhombic ZSN on a (111)-oriented YSZ substrate, again showing the optical emission peak at around 2 eV which we associate with conduction band to valence band recombination.

the PL and DRS measurements presented earlier in this Chapter. The measurements together provide a valuable measurement of the end point of the surprisingly large range of band-gap values between randomly disordered (wurtzite) and fully ordered (orthorhombic) forms of the ZSN structure.

Finally, we turn to the CL measurements on QW structures formed as a heterostructure of wurtzite and orthorhombic layers. This is an unusual example of a QW structure which has the same composition in each layer, except with the cations ordered to make the higher band gap barrier layers and disordered to make the lower band-gap well region. Figure 4.39 shows the CL spectrum of such a QW sample (QW 146). Interestingly, the mid-gap substrate fluorescence (the feature around 2.3 eV) appears to be significantly red-shifted compared to the mid-gap substrate fluorescence seen in Figures 4.36 and 4.38. It is not clear why this energy shift would occur, but may be related to band bending that is known to occur in epitaxial nanostructures with different band gaps[49]. There are no existing studies of band offsets in such an

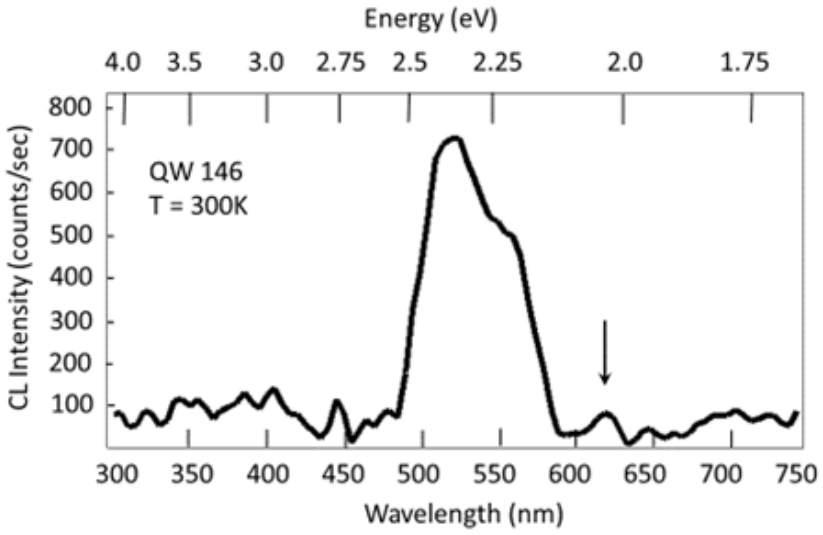

Figure 4.39: Ambient temperature CL spectrum of sample QW 146. The small peak at the arrowed position is possibly associated with the band gap of orthorhombic ZSN. Note that the CL spectral range of the Gatan Mono CL4 spectrograph does not provide access to the expected optical emission from quantum well states in the mid-IR.

order-disorder heterostructure, thus it would be interesting to study this phenomenon in future studies. In addition to the aforementioned feature, a weak peak around 2 eV is observed in the CL spectrum of QW146 (see Figure 4.39). This might originate from the orthorhombic barrier layer that is part of the QW heterostructure. It would be interesting to use the high-resolution capability of the TESCAN microscope to obtain spatially resolved CL signals from the different component layers of the QW heterostructure. This would be the next development for this particular study. It will also be important to extend the spectroscopic range of the measurement into the IR region to look for evidence of optical emission from states in the well region of the heterostructure. As of writing, the appropriate detector to achieve CL signals in the IR is available but not currently installed on the TESCAN instrument. When the IR detector is installed, these measurements will be performed in edge-on geometry to enable probing of the individual layers of the QW.

CHAPTER V

Conclusion & Future Directions

Here we provide a summary of the major findings of this dissertation work, including the novel ideas and their significance, along with suggestions on how the conducted experiments can be enhanced or iterated upon in the future. This will aid in providing a clearer understanding of how to move forward with the investigation of $ZnSnN_2$ as a potentially important addition to the family of technologically useful optoelectronic materials. This project, part of a wide-ranging collaboration with partners in several countries, including New Zealand, France, UK, as well as USA, aims to explore the earth abundant II-IV nitride family of materials from the perspective of sustainable optoelectronic applications, particularly solar harvesting and LEDs. The project overall has taken on many facets, with the lead on materials growth centered on Prof. Durbin's research group at Western Michigan University, in Kalamazoo, with whom the author has been working intensively over the course of this dissertation. The specific goal of this dissertation has been to perform what are essentially the first studies of the optoelectronic aspects of the thin films of one specific member of the II-IV nitride family, $ZnSnN_2$, of especial interest for its ability to cover the visible and near IR spectral range of interest for solar energy harvesting and LED lighting applications.

5.1 Major Findings

5.1.1 MBE

Thin films (<100 nm) of $ZnSnN_2$ were grown on (111)-oriented YSZ substrates via plasma-assisted molecular beam epitaxy. A great amount of attention was given to the establishment of those growth parameters which govern the growth rate and order paramter, S, of ZSN thin films[13, 15]. Although MBE growth method is exacting and unforgiving, and maybe a little tedious, it allows for highly reproducible results with a large degree of control over the stoichiometry. For this reason MBE is critical to the progression of establishing a basic understanding of this new material. Future experiments which utilize MBE growth of ZSN are likely to see significant progess due to the level of control one has over the growth parameters and also, due to the advantage of being able to grow high quality material with relatively few defects. However, as we have encountered, the stoichiometry of the films is a significant issue contributing to a relatively high background charge carrier concentration. This is currently one of the major impediments to the development of viable optoelectronic devices based on ZSN.

5.1.2 RHEED

RHEED is a powerful tool for *in situ* analysis of MBE growth. The immediate acquisition of strucutral data allowed for quick estimations of growth rates and crystallinity, which were useful for on-the-fly tuning of the growth parameters. RHEED images were acquired using the KSA 400 image acquisition and analysis package. Post-growth analysis included accurate determination of crystallinity and film thicknesses from the pixel brightness acquired via taking linescans across the RHEED images using the ImageJ software. In summary RHEED has played an important role in determining what growth conditions are required to span the range of cation ordering

and structures that the ternary heterovalent cation compounds such as $ZnSnN_2$ have to offer. The use of superlattice reflections in the RHEED pattern, especially (210), has been particularly useful as a quantitative measure of cation ordering. In turn, this has played a major role in being able to demonstrate that it is possible to tune the band gap across a large range of values equivalent to the all-important visible and IR regions of the spectrum.

5.1.3 XRD

While not a major part of this particular thesis project, X-ray diffraction has been of great use as a characterization tool in the sense that cation ordering has a profound influence on all the physical properties of ZSN and this ordering can be quantitatively determined through the dependence of the structure factor, and hence certain X-ray diffraction intensities, on the order parameter, S. Both RHEED and XRD have been critical in this respect and have demonstrated excellent agreement in the values of S determined by both techniques. S has also been determined by Raman scattering, although is not included in this dissertation, per se. Several films were measured with the high-brightness X-rays produced by the Advanced Photon Source at Argonne National Lab. These experiments show evidence of an expansion of the c-axis corresponding to the predicted orthorhombic structure as detailed by Feldberg et al. [28]. The basis for the growth of subsequent films builds on the results of these experiments, carried out by Senabulya et al. [12] and are critical to the future development of this material. Films were measured with xrays sourced from a 7 GeV synchrotron at the APS, and 3DRSMs were created by compiling a series of 2D scans created by the reflection of the source beam across the sample in rsMap3D, a program developed by Chris Schleputz and Argonne National Lab.

5.1.4 PL

The dissertation presents the first PL measurements on MBE grown films of ZSN. We found that the technique is difficult to use on very thin films (100 nm and less), and the presence of artifacts presents challenges for their analysis. In some cases the results were somewhat inconclusive. Nevertheless PL provided interesting data which are useful to compare with those from other optical techniques such as DRS and CL. Of particular interest are the results of PL measurements on a novel ZSN quantum well structure, which appear to show evidence of emission from confined states. The results are preliminary at this stage and need to be explored in more detail to ensure their credibility. We performed temperature dependent PL studies on the samples, between 10 K and 290 K. As expected there is a significant effect from thermal excitation at the higher temperatures, with the spectral features becoming weaker and broader, although perhaps not as much as would be expected in PL. The choice of excitation source was found to be very important for these measurements, and in particular the use of a He-Ne laser was problematic in that its photon energy was similar to the expected bandgap of ordered ZSN and it was uncertain whether this source had sufficient energy to excite the interband transitions of interest. He-Ne also exhibited many additional peaks which could have interfered with the PL data. For this reason we chose to use shorter wavelength lasers, such as 532 nm and 350 nm. Overall, the PL measurements proved to be difficult but potentially valuable for comparison with the results of other optical characterization techniques.

5.1.5 CL

The first cathodoluminescence studies on MBE-grown orthorhombic (ordered phase) ZSN thin films ($\sim$ 100 nm), as well as ZSN QWs (the first of their kind) formed as heterostructures of wurtzite and orthorhombic layers, were conducted at the Michigan Center for Materials Characterization $(MC)^2$ as a novel part of this dissertation.

Ambient temperature CL spectra from ZSN single-layer thin films demonstrated optical emission at around 2 eV, consistent with several theoretical predictions previously made for the ordered phase of ZSN[18, 20, 24, 26]. This same emission was observed in the CL spectrum of the QW, although with relatively diminished intensity. The significance of these results is that they assist in providing an empirical endpoint for the band-edge of orthorhombic ZSN with near-maximum order parameter, S = 1. These measurements represent the first evidence of optical emission by MBE-grown ZSN and are corroborated by novel spectroscopy measurements made in this work. In the immediate future, there are plans to extend the spectroscopic range of this measurement into the IR by probing optical emission from the wurtzite layers of this structure via the edge-on geometry.

5.1.6 Fine-Tuning the WDRS Method

Waveguided Diffuse Reflectance Spectroscopy (or WDRS), a novel approach we devised to the traditional DRS method, was demonstrated to be a viable method for thin-film band-edge probing, although a more controlled setup is needed to acquire data with a higher degree of consistency. Ordered ZSN thin films demonstrated a relative blueshift in the bang-edge as compared to the wurtzite (disordered) films. Significant improvements to the signal were obtained over that from using the traditional DRS method. Upon further investigation of optimizing photon incidence and the experimental setup, significant improvements are expected to be seen in probing the band edge of thin-films in the future. This work was significant not only from the technical perspective of how to improve band-edge measurements, but also as a demonstration that it enabled measurements of a critically important quantity, namely the optical band gap, which allowed to make an important correlation with the degree of cation ordering. This is one of the most significant aspects of the results obtained in this dissertation project. In particular, the determination of the band-gap

associated with the end point (S=1) of the fully-ordered, orthorhombic structure of ZSN is a significant step forward for this materials system.

5.1.7 Hall Effect

Hall measurements on ZSN single thin-films and thin-film QWs revealed a relatively high level of n-type carriers, with concentrations ranging between 10^{20}-10^{21} cm^{-3} and mobilities ranging (mostly) between 10-35 cm^2/Vs. Although a method for reducing the effects of thermal noise was studied, it is highly suggested that future experiments include low-temperature measurements to mitigate the electron-phonon interactions that we expect to be dominant at room temperature.

5.1.8 Future Work

The need for earth-abundant materials for energy harvesting and solid-state lighting is timely and would clearly be beneficial for society and the environment. The II-IV nitride family offers an interesting addition to the relatively few materials options available at the present time, none of which are particularly sustainable for large-scale deployment as a long-term solution to the problem. $ZnSnN_2$ is obviously at a very early stage of development for such applications and many challenges have to be overcome to bring it to the point of a viable optoelectronic device material. Clearly there is much to be done and in this outlook for the future we will touch upon just a few of the outstanding problems that need to be addressed in future research.

On of the most critical issues for any semiconductor system is the question of doping. All of the many successful semiconductors that have been implemented in devices over the last 7 decades have overcome this need, often after many years of very difficult research. Usually, it involves identifying appropriate dopants, of both polarities (p and n), and learning how to control their concentration over a wide range of

carrier densities. This is particularly hard for compound semiconductors, but spectacular success has been achieved with III-V's and II-IV compounds to the point where excellent device characteristics are now routinely demonstrated in commercial device deployment. For ternaries, control of doping is even more challenging, and this is certainly the case with $ZnSnN_2$. As was pointed out in Chapter II, maintaining stoichiometry of Zn and Sn is particularly difficult because of the large disparity in sticking coefficient between these two cation species. As Zn and Sn are heterovalent, even small imbalances can be a significant source of unwanted free carriers, the so-called self-doping effect. This was explored in some detail in the Hall Effect studies presented in Chapter IV where carrier densities approaching degenerate levels were seen in some cases. Nitrogen vacancies and interstitials can also contribute to the problem, although this was not specifically addressed in this dissertation. Therefore, much additional effort needs to be put into control of doping, by identifying ways to compensate for the high concentration of n-type carriers and, if possible to controllably introduce p-type doping so that heterojunctions can be routinely fabricated. Building on the theme of energy-critical materials, this would open up the possibility of making single junction and even multijunction solar cells from ZSN. The additional degrees of freedom offered by the ability to tune the band-gap by means of ordering/disorder of the cations is particularly interesting for both LED applications and for solar energy harvesting.

The iso-compositional QW geometry demonstrated in the previous Chapter is a potentially fruitful direction that would be interesting to further explore in this regard. The ability of MBE to make very clean, atomically abrupt interfaces between YSZ substrates and ZSN is promising for such future work.

The use of novel geometries for optical characterization, especially the waveguided diffuse reflectance approach devised in this project is also very promising for future studies of thin film samples. An instrument which incorporates delivery of the broad-

band optical probe beam (by means of optical fiber) and precise alignment of the sample to launch the probe beam into the film at the required angle of acceptance, would be a welcome addition to existing band-edge measurement capabilities.

Finally, we envision that the II-IV nitrides, of which ZSN is a particularly interesting and relevant example, may play an important role in the future of optoelectronics. It is relatively recent to raise concerns about the sustainability of technological applications, but clearly society's use of rare mineral resources impacts on this question in a fundamental way. We hope that the work presented here will stimulate more research to address this concern.

BIBLIOGRAPHY

BIBLIOGRAPHY

[1] NW Ashcroft and ND Mermin. *Solid State Physics*. Harcourt, Inc., 1976.

[2] TD Lee and AU Ebong. A review of thin film solar cell technologies and challenges. *Renewable and Sustainable Energy Reviews*, 70, 2017.

[3] Energy critical elements, 2011. URL https://www.aps.org/units/fps/newsletters/201107/jaffe.cfm.

[4] J Nelson. *The Physics of Solar Cells*. Imperial College Press, 2003.

[5] J Berzelius. Investigation of hydrofluoric acid and of its most noteworthy compounds. *Proceedings of the Royal Science Academy*, 12, 1824.

[6] E Becquerel. Memoire sur les effets electriques produits sous l'influence des rayons solaires. *Comptes Rendus*, 9, 1839.

[7] CE Fritts. On a new form of selenium photocell. *American Journal of Science*, 26, 1883.

[8] A Kumar. Predicting efficiency of solar cells based on transparent conducting electrodes. *Journal of Applied Physics*, 121, 2017.

[9] J Ramanujam and UP Singh. Copper indium gallium selenide based solar cells - a review. *Energy Environ. Sci.*, 10, 2017.

[10] W Shockley and HJ Queisser. Detailed Balance Limit of Efficiency of P-N Junction Solar Cells. *Journal of Applied Physics*, 32(3), 1961.

[11] Iupac, 2018. URL http://iupac.org/cms/wp-content/uploads/2015/07/IUPAC_Periodic_Table-28Nov16.jpg.

[12] N Senabulya, N Feldberg, RA Makin, Y Yang, G Shi, CM Jones, E Kioupakis, J Mathis, R Clarke, and SM Durbin. Stabilization of orthorhombic phase in single-crystal $ZnSnN_2$ films. *AIP Advances*, 6(7), 2016.

[13] RA Makin, N Senabulya, J Mathis, N Feldberg, P Miska, R Clarke, and SM Durbin. Growth of ordered and disordered $ZnSnN_2$. *Journal of Vacuum Science & Technology B*, 35(2), 2017.

[14] RA Makin, K York, N Senabulya, J Mathis, R Clarke, N Feldberg, P Miska, CM Jones, L Williams, E Kioupakis, R Reeves, and SM Durbin. Order Parameter and Band Gap of $ZnSnN_2$. In *2018 IEEE 7th World Conference On Photovoltaic Energy Conversion (WCPEC) (A Joint Conference of 45th IEEE PVSC, 28th PVSEC & 34th EU PVSEC)*, 2018.

[15] RA Makin, K York, SM Durbin, N Senabulya, J Mathis, R Clarke, N Feldberg, P Miska, CM Jones, Z Deng, L Williams, E Kioupakis, and RJ Reeves. Alloy-Free Band Gap Tuning across the Visible Spectrum. *Physical Review Letters*, 122(25), 2019.

[16] JE Jaffe and A Zunger. Theory of the Band-gap Anomaly in ABC_2 Chalcopyrite Semiconductors. *Physical Review B*, 29(4), 1984.

[17] DO Scanlon and A Walsh. Bandgap engineering of $ZnSnP_2$ for high-efficiency solar cells. *Applied Physics Letters*, 100(25), 2012.

[18] N Feldberg, JD Aldous, WM Linhart, LJ Phillips, K Durose, PA Stampe, RJ Kennedy, DO Scanlon, G Vardar, RL Field, III, TY Jen, RS Goldman, TD Veal, and SM Durbin. Growth, disorder, and physical properties of $ZnSnN_2$. *Applied Physics Letters*, 103(4), 2013.

[19] A Walsh, S Chen, SH Wei, and XG Gong. Kesterite Thin-Film Solar Cells: Advances in Materials Modelling of Cu_2ZnSnS_4. *Advanced Energy Materials*, 2, 2012.

[20] A Punya, WRL Lambrecht, and M van Schilfgaarde. Quasiparticle band structure of Zn-IV-N_2 compounds. *Phys. Rev. B*, 84, 2011.

[21] C Kittel. *Introduction to Solid State Physics*. John Wiley & Sons, Inc., 2005.

[22] Solar spectrum, 2013. URL https://en.wikipedia.org/wiki/Sunlight#/media/File:Solar_spectrum_en.svg.

[23] A Punya and WRL Lambrecht. Band offsets between $ZnGeN_2$, GaN, ZnO, and $ZnSnN_2$ and their potential impact for solar cells. *Physical Review B*, 88(7), 2013.

[24] L Lahourcade, NC Coronel, KT Delaney, SK Shukla, NA Spaldin, and HA Atwater. Structural and Optoelectronic Characterization of RF Sputtered $ZnSnN_2$. *Advanced Materials*, 25(18), 2013.

[25] PC Quayle, K He, J Shan, and K Kash. Synthesis, lattice structure, and band gap of $ZnSnN_2$. *MRS Communications*, 3(3), 2013.

[26] S Chen, P Narang, HA Atwater, and LW Wang. Phase Stability and Defect Physics of a Ternary $ZnSnN_2$ Semiconductor: First Principles Insights. *Advanced Materials*, 26(2), 2014.

[27] P Narang, S Chen, NC Coronel, S Gul, J Yano, LW Wang, NS. Lewis, and HA Atwater. Bandgap Tunability in Zn(Sn,Ge)N_2 Semiconductor Alloys. *Advanced Materials*, 26(8), 2014.

[28] N Feldberg, JD Aldous, PA Stampe, RJ Kennedy, TD Veal, and SM Durbin. Growth of $ZnSnN_2$ by Molecular Beam Epitaxy. *Journal of Electronic Materials*, 43(4), 2014.

[29] TM Razykov, CS Ferekides, D Morel, E Stefanakos, HS Ullal, and HM Upadhyaya. Solar photovoltaic electricity: Current status and future prospects. *Solar Energy*, 85(8), 2011.

[30] D Litvinov, CA Taylor, II, and R Clarke. Semiconducting cubic boron nitride. *Diamond and Related Materials*, 7(2), 1998.

[31] A Ichimiya and P Cohen. *Reflection High-Energy Electron Diffraction*. Cambridge University Press, 2004.

[32] Hyperphysics, 2017. URL http://hyperphysics.phy-astr.gsu.edu/hbase/index.html.

[33] BD Cullity. *Elements of X-ray Diffraction*. Addison-Wesley Publishing Company Inc., 1978.

[34] Y Wang, X Liu, K-S Im, W-K Lee, J Wang, K Fezzaa, DLS Hung, and JR Winkelman. Ultrafast X-ray study of dense-liquid-jet flow dynamics using structure-tracking velocimetry. *Nature Physics*, 4(4), 2008.

[35] X Zuo, J Wang, P Yu, D Eyler, H Xu, MR Starich, DM Tiede, AE Simon, W Kasprzak, CD Schwieters, BA Shapiro, and Y-X Wang. Solution structure of the cap-independent translational enhancer and ribosome-binding element in the 3 UTR of turnip crinkle virus. *Proceedings of the National Academy of Sciences of the United States of America*, 107(4), 2010.

[36] Advanced photon source grabngo, 2019. URL https://www.aps.anl.gov/Media-Center/APS-Slides.

[37] Advanced photon source grabngo, 2019. URL https://www.aps.anl.gov/Media-Center/APS-Slides.

[38] K Matsuo and K Nakano. Characterization of semiconductor oxides by IR diffuse reflectance spectroscopy. *Applied Surface Science*, 41-42, 1990.

[39] ZM Gibbs, A LaLonde, and GJ Snyder. Optical band gap and the Burstein-Moss effect in iodine doped PbTe using diffuse reflectance infrared Fourier transform spectroscopy. *New Journal of Physics*, 15, 2013.

[40] VA Christie, ST Liem, RJ Reeves, VJ Kennedy, A Markwitz, and SM Durbin. Characterisation of polycrystalline gallium nitride grown by plasma-assisted evaporation. *Current Applied Physics*, 4(2-4), 2004.

[41] Y Xiang, F-W Guo, T-M Lu, and G-C Wang. Reflection high-energy electron diffraction measurements of reciprocal space structure of 2D materials. *Nanotechnology*, 27(48), 2016.

[42] PC Quayle, EW Blanton, A Punya, GT Junno, K He, L Han, H Zhao, J Shan, WRL Lambrecht, and K Kash. Charge-neutral disorder and polytypes in heterovalent wurtzite-based ternary semiconductors: The importance of the octet rule. *Physical Review B*, 91(20), 2015.

[43] K Mukherjee, PB Deotare, and EA Fitzgerald. Improved photoluminescence characteristics of order-disorder AlGaInP quantum wells at room and elevated temperatures. *Applied Physics Letters*, 106(14), 2015.

[44] Vanderpauwcontactplacement, 2019. URL https://en.wikipedia.org/wiki/Van_der_Pauw_method#/media/File:VanderPauwContactPlacement.jpg.

[45] LJ van der Pauw. A Method of Measuring the Resistivity and Hall Coefficient on Lamellae of Arbitrary Shape. *Philips Technical Review*, 20, 1958.

[46] N Kikegawa and K Furuya. Scattering reduction due to electron wave interference by periodic doping of impurity ions in semiconductors. *Physica B*, 227(1-4), 1996.

[47] PDC King, T D Veal, SA Hatfield, PH Jefferson, CF McConville, CE Kendrick, CH Swartz, and SM Durbin. X-ray photoemission spectroscopy determination of the InN/yttria stabilized cubic-zirconia valence band offset. *Applied Physics Letters*, 91(11), 2007.

[48] VR PaiVerneker, AN Petelin, FJ Crowne, and DC Nagle. Color-center-induced band-gap shift in Yttria-Stabilized Zirconia. *Physical Review B*, 40(12), 1989.

[49] Z Zhang and JT Yates, Jr. Band Bending in Semiconductors: Chemical and Physical Consequences at Surfaces and Interfaces. *Chemical Reviews*, 112(10), 2012.